

## ABSTRACT

Title of dissertation:      MICROSCALE DIELECTRIC  
                                  ANTI-REFLECTION COATINGS  
                                  FOR PHOTOVOLTAICS

Dongheon Ha, Doctor of Philosophy, 2016

Dissertation directed by:  Professor Jeremy N. Munday  
                                  Department of Electrical and Computer Engineering

In order to power our planet for the next century, clean energy technologies need to be developed and deployed. Photovoltaic solar cells, which convert sunlight into electricity, are a clear option; however, they currently supply  $< 0.1\%$  of the US electricity due to the relatively high cost per Watt of generation. Thus, our goal is to create more power from a photovoltaic device, while simultaneously reducing its price. To accomplish this goal, we are creating new high efficiency anti-reflection coatings that allow more of the incident sunlight to be converted to electricity, using simple and inexpensive coating techniques that enable reduced manufacturing costs.

Traditional anti-reflection coatings (consisting of thin layers of non-absorbing materials) rely on the destructive interference of the reflected light, causing more light to enter the device and subsequently get absorbed. While these coatings are used on nearly all commercial cells, they are wavelength dependent and are deposited using expensive processes that require elevated temperatures, which increase production cost and can be detrimental to some temperature sensitive solar cell materials.

We are developing two new classes of anti-reflection coatings (ARCs) based on textured dielectric materials: (i) a transparent, flexible paper technology that relies on optical scattering and reduced refractive index contrast between the air and semiconductor and (ii) silicon dioxide ( $\text{SiO}_2$ ) nanosphere arrays that rely on collective optical resonances. Both techniques improve solar cell absorption and ultimately yield high efficiency, low cost devices. For the transparent paper-based ARCs, we have recently shown that they improve solar cell efficiencies for all angles of incident illumination reducing the need for costly tracking of the sun's position [1], [2]. For a GaAs solar cell, we achieved a 24% improvement in the power conversion efficiency using this simple coating. Because the transparent paper is made from an earth abundant material (wood pulp) using an easy, inexpensive and scalable process, this type of ARC is an excellent candidate for future solar technologies.

The coatings based on arrays of dielectric nanospheres also show excellent potential for inexpensive, high efficiency solar cells. The fabrication process is based on a Meyer rod rolling technique, which can be performed at room-temperature and applied to mass production, yielding a scalable and inexpensive manufacturing process. The deposited monolayer of  $\text{SiO}_2$  nanospheres, having a diameter of 500 nm on a bare Si wafer, leads to a significant increase in light absorption and a higher expected current density based on initial simulations, on the order of 15-20%. With application on a Si solar cell containing a traditional anti-reflection coating ( $\text{Si}_3\text{N}_4$  thin-film), an additional increase in the spectral current density is observed, 5% beyond what a typical commercial device would achieve [3]. Due to the coupling between the spheres originated from Whispering Gallery Modes (WGMs) inside each

nanosphere, the incident light is strongly coupled into the high-index absorbing material, leading to increased light absorption. Furthermore, the SiO<sub>2</sub> nanospheres scatter and diffract light in such a way that both the optical and electrical properties of the device have little dependence on incident angle, eliminating the need for solar tracking. Because the layer can be made with an easy, inexpensive, and scalable process, this anti-reflection coating is also an excellent candidate for replacing conventional technologies relying on complicated and expensive processes.

MICROSCALE DIELECTRIC ANTI-REFLECTION COATINGS  
FOR PHOTOVOLTAICS

by

Dongheon Ha

Dissertation submitted to the Faculty of the Graduate School of the  
University of Maryland, College Park in partial fulfillment  
of the requirements for the degree of  
Doctor of Philosophy  
2016

Advisory Committee:  
Professor Jeremy N. Munday/Advisor  
Professor Thomas E. Murphy  
Professor Julius Goldhar  
Professor John Melngailis  
Professor Kyu Yong Choi

© Copyright by  
Dongheon Ha  
2016

To the memory of my grandmother

*Jaeboon Song*

1928 - 2014

*For her unconditional love and endless prayer to me*

## Acknowledgments

First, I would like to express my sincere gratitude to my advisor Professor Jeremy N. Munday for his continuous support of my doctoral study, for his patience, motivation, and immense knowledge. His guidance helped me during the time I spent researching and writing my thesis. I could not have imagined having a better advisor and mentor for my doctoral study.

Besides my advisor, I would like to thank the rest of my thesis committee: Professor Thomas E. Murphy, Professor Julius Goldhar, Professor John Melngailis, and Professor Kyu Yong Choi for their insightful comments and encouragement, but also for the hard questions which incited me to widen the perspective of my research.

My sincere thanks also goes to Prof. Marina S. Leite, Prof. Liangbing Hu, Chen Gong and Zhiqiang Fang in the department of Materials Science and Engineering at UMD, who provided me an opportunity to join their team as a collaborator, and who gave access to the laboratory and research facilities. Without their precious support, it would have not been possible to conduct this research.

I thank Joe Murray Yunlu Xu, Joe Garrett, Tao Gong, Dakang Ma, David Somers, Lisa Krayner, and Dan Goldman, for the stimulating discussions, for the time we were working together, and for all the fun we have had in the last five years. I have been surrounded by great people in the lab.

Also I thank my previous advisors, Prof. Hee Chul Lee at Korea Advanced Institute of Science and Technology (KAIST) and Prof. Joon-Yong Lee at Handong

University for their endless encouragements to perform scientific research. Without their sincere support and motivation, I would not have been able to get to where I am.

I had many different sources of financial support during my doctoral study. Thanks to them, I have been able to solely focus on academics. I would like to thank the following people and organizations for their support: the Graduate School for a Graduate Dean's Dissertation Fellowship, the Future Faculty Program of the A. Clark School of Engineering at UMD, the Department of Electrical and Computer Engineering for teaching assistantships, and Professor Jeremy N. Munday for research assistantships.

To my friends, thank you for listening, offering advice, and supporting me throughout graduate school. I would like to express special thanks to my best friends: Sungjin Kim and Hyun Bok Kim for their everlasting friendship. I will never forget all the chats and beautiful moments I shared with some of my PhD comrades, Sung Jun Yoon, Kangmook Lim, Sungmin Eum, and Ginnah Lee. It was also my pleasure to share unforgettable time with some local friends, Jaemin Yi, Haarin Chun, Chiyong Oh, Brian Park and others in K-team, Acts 29, and GMC. Also, thanks to all friends from KAIST and Handong University for their cheering via texts, phone calls, and letters. The last year of my doctoral study was the most meaningful as I could persevere through difficulties with my sweetheart, Hyun Gee Kim. I appreciate for her true, compassionate, and long-lasting love.

Last, but certainly not least, I would like to thank my family. I feel the need to express my gratitude and love to my parents and to my brother for supporting me

spiritually throughout graduate school and all my life. I would also like to express my warmest love to my grandmother who passed away during my doctoral study. I feel a sense of gratitude beyond expression to my family.

And now I'm moving on to the next phase. I would like to thank God for making all things possible.

Dongheon Ha

April 2016

College Park, MD

## Table of Contents

List of Tables	viii
List of Figures	ix
List of Publications	xi
<b>1 Introduction</b>	<b>1</b>
1.1 Solar in demand . . . . .	1
1.2 Solar cell light management . . . . .	4
1.3 Traditional anti-reflection coatings . . . . .	5
1.4 Transparent paper-based anti-reflection coating . . . . .	9
1.5 Dielectric resonator-based anti-reflection coating . . . . .	10
1.6 Outline of this thesis . . . . .	11
<b>2 Characterization of cellulose-fiber paper</b>	<b>13</b>
2.1 Overview . . . . .	13
2.2 Transparent cellulose paper . . . . .	15
2.3 Attachment on solar cells . . . . .	25
<b>3 Paper-based anti-reflection coatings on solar cells</b>	<b>33</b>
3.1 Optoelectronic response of coated solar cells . . . . .	33
3.1.1 GaAs solar cell . . . . .	35
3.1.2 Si solar cell . . . . .	42
3.2 Paper-based anti-reflection coatings on a low index of refraction substrate . . . . .	48
3.3 Conclusion . . . . .	51
<b>4 Dielectric micro-resonators</b>	<b>52</b>
4.1 Fabrication steps . . . . .	53
4.2 Simulations of optical response . . . . .	56
4.3 Optical enhancement due to nanospheres . . . . .	58
4.4 Coupling of whispering gallery modes into the absorbing layer . . . . .	63
4.5 Resonance tuning . . . . .	67

4.6	Microscale optical measurement . . . . .	69
4.7	Microscale electrical measurement . . . . .	76
4.8	Conclusions . . . . .	82
5	<b>Conclusions and future outlook</b>	83
5.1	Improving transparent paper coatings . . . . .	84
5.2	Improving dielectric micro-resonator coatings . . . . .	85
A	<b>Additional information on experiments and calculations</b>	86
A.1	Polarization of optical setup . . . . .	86
A.2	Incoherent reflection model . . . . .	90
B	<b>Fabrication details</b>	93
B.1	Deposition of SiO <sub>2</sub> nanospheres using a Meyer rod . . . . .	93
B.2	A Si photodetector . . . . .	94
	Bibliography	105

## List of Tables

3.1	Electrical properties of GaAs solar cells . . . . .	41
3.2	Electrical properties of Si solar cells . . . . .	45
B.1	Si photodetector fabrication steps . . . . .	104

## List of Figures

1.1	Current density as a function of voltage for a typical solar cell . . . . .	3
1.2	Schematic of traditional anti-reflection coatings . . . . .	6
2.1	Transparent paper anti-reflection coating . . . . .	14
2.2	Optical properties of paper coating . . . . .	16
2.3	Picture of macroscale optical measurement setup . . . . .	18
2.4	Schematic of macroscale optical measurement setup . . . . .	20
2.5	Long-term effect of solar irradiation on the paper . . . . .	24
2.6	Transparent paper attachment and removal . . . . .	26
2.7	Reduced reflection over a wide range of incident angles and wave-lengths on GaAs solar cells . . . . .	28
2.8	Polarization dependence of the experimental setup . . . . .	29
2.9	Comparison between the measured and calculated reflectivity . . . . .	32
3.1	Schematic of the GaAs solar cell . . . . .	34
3.2	Quantum efficiency measurements for GaAs solar cells . . . . .	36
3.3	External quantum efficiency measurement setup . . . . .	38
3.4	Current density vs. voltage characteristic for GaAs solar cells . . . . .	40
3.5	Reduced reflection over a wide range of incident angles and wave-lengths on Si solar cells . . . . .	43
3.6	Quantum efficiency measurements and current density vs. voltage characteristic for Si solar cells . . . . .	47
3.7	Reflectivity of a polymer (P3HT) on glass upon the addition of a paper ARC . . . . .	50
4.1	Schematic showing the deposition process using a Meyer rod . . . . .	54
4.2	Fabrication steps for the SiO <sub>2</sub> dielectric nanosphere coating . . . . .	55
4.3	FDTD simulation structure with 500 nm nanospheres . . . . .	57
4.4	Experimental and simulated absorptivity . . . . .	60
4.5	Thin-film effect to explain a broadband enhancement . . . . .	62
4.6	Field intensity at resonance vs. off resonance . . . . .	64
4.7	Calculated spectral current density with SiO <sub>2</sub> nanosphere coating . . . . .	66
4.8	Reflectance variation due to spacing and sphere diameter . . . . .	68

4.9	Microscale vs. Macroscale optical measurement . . . . .	70
4.10	Measured spectrum of the tungsten halogen white light source . . . . .	71
4.11	Characterization of sphere size variation . . . . .	74
4.12	Optical simulations of non-uniform arrays of nanospheres . . . . .	75
4.13	A photograph showing the optical path for the supercontinuum laser coupled into the microscope . . . . .	78
4.14	Schematic showing the microscale photocurrent measurement set-up . . . . .	79
4.15	Optical and SEM images showing the Si solar cell used for photocur- rent measurements . . . . .	80
4.16	Photo-response measurement on a Si solar cell . . . . .	81
A.1	Schematic of the polarizers used in the optical set-up . . . . .	89
A.2	Schematic depicting multiple reflections . . . . .	90
B.1	Layout of the photomask . . . . .	96
B.2	Schematic of a Si photodetector . . . . .	97
B.3	Photolithograph . . . . .	98
B.4	Ag deposition with a thermal evaporator . . . . .	99
B.5	Ag removal . . . . .	100
B.6	Pt deposition with a electron beam evaporator . . . . .	101
B.7	Additional metal deposition . . . . .	102
B.8	Fabricated Si photodetector . . . . .	103

## List of Publications

Work from this thesis has resulted in the following publications:

**Dongheon Ha**, Joseph Murray, Zhiqiang Fang, Liangbing Hu, and Jeremy N. Munday, “Advanced broadband antireflection coatings based on cellulose microfiber paper,” *IEEE Journal of Photovoltaics*, **5**, 577-583 (2015).

**Dongheon Ha**, Zhiqiang Fang, Liangbing Hu, and Jeremy N. Munday, “Paper-based anti-reflection coatings for photovoltaics,” *Advanced Energy Materials*, **4**, 1301804 (2014). (**Inside Cover**)

Zhiqiang Fang\*, Hongli Zhu\*, Yongbo Yuan\*, **Dongheon Ha**, Shuze Zhu, Colin Preston, Qingxia Chen, Yuanyuan Li, Xiaogang Han, Seongwoo Lee, Gang Chen, Teng Li, Jeremy Munday, Jinsong Huang, and Liangbing Hu, “Novel Nanostructured Paper with Ultrahigh Transparency and Ultrahigh Haze for Solar Cells,” *Nano Letters*, **14**, 765-773 (2014). (\* indicates equal contribution)

**Dongheon Ha** and Jeremy N. Munday, “Transparent paper for optoelectronic applications,” (*invited Review Article in preparation*).

**Dongheon Ha**, Chen Gong, Marina S. Leite, and Jeremy N. Munday, “Demonstration of resonance coupling in scalable dielectric micro-resonator coatings for photovoltaics,” (*submitted and under review*).

## Chapter 1: Introduction

### 1.1 Solar in demand

The development of advanced photovoltaic technologies is critical to reducing the cost per watt of alternative energy. Currently  $\sim 10\%$  of the US energy production comes from renewables (including hydropower and biomass) and only  $< 0.1\%$  is from solar [4]. Recently the National Renewable Energy Laboratory (NREL) released a study suggesting that by 2050 nearly 80% of the power in the US could be generated by renewable sources, while keeping the grid stable [5]. However, to achieve this target, solar generation needs to increase to cover  $> 10\%$  of energy production.

In order to make solar photovoltaics cost competitive with fossil fuel based technologies, it is crucial to reduce inefficiencies that limit the solar power conversion. For a material with a given bandgap energy, the short-circuit current density,  $J_{sc}$ , is limited by the cell's ability to absorb above bandgap energy photons, and the open-circuit voltage,  $V_{oc}$ , is limited by the bandgap energy. The efficiency,  $\eta$ , of the solar cell is related to the product of these two quantities. Therefore, it is essential to maximize both of them simultaneously in order to achieve the optimal solar cell efficiency.

The efficiency of a solar cell is defined as the ratio of the energy output from the device to input energy from the sun. Thus, the efficiency depends not only on the device and its operating temperature, but also on the sun's spectrum and intensity. Therefore, to compare the performance of different terrestrial solar cells, we use the AM1.5G solar spectrum and a temperature of 25 °C.<sup>1</sup>

Figure 1.1 shows an example of a current-voltage curve for a typical solar cell under illumination. The maximum power per unit area is given by

$$\begin{aligned}\frac{P_{max}}{A} &= J_{max} \cdot V_{max} \\ &= J_{sc} \cdot V_{oc} \cdot FF\end{aligned}\tag{1.1}$$

where  $J_{max}$  and  $V_{max}$  are the current density and voltage at maximum power,  $A$  is the area of the device,  $J_{sc}$  is the short-circuit current density,  $V_{oc}$  is the open-circuit voltage, and  $FF$  is the fill factor, which describes the squareness of the current-voltage characteristic. The efficiency is then calculated as

$$\eta = \frac{P_{max}}{P_{in}} = \frac{J_{sc} \cdot V_{oc} \cdot FF}{P_{in}}\tag{1.2}$$

where  $P_{in}$  is the input power from the sun. The input power per unit area is 1 kW/m<sup>2</sup> (or 100 mW/cm<sup>2</sup>).

---

<sup>1</sup>AM1.5G refers to 1.5 air masses, which is the agreed upon standard illumination condition for testing purposes based on average solar conditions. Note AM1.0G, would correspond to 1 air mass, *i.e.* the sun directly overhead.

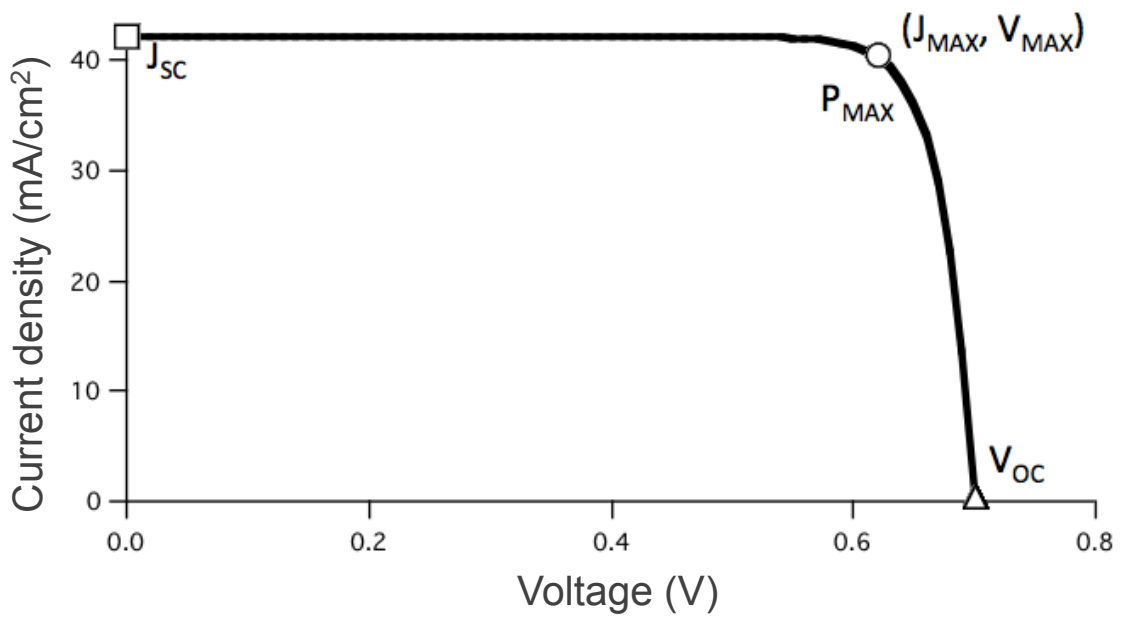


Figure 1.1: Current density as a function of voltage for a typical solar cell showing important parameters and the maximum power point.

## 1.2 Solar cell light management

For a typical air-semiconductor interface,  $> 30\%$  of the incident light is lost to reflection, and reducing this reflection is a key design principle for making high-quality solar cells. To accomplish this goal, coatings are typically applied that rely on optical resonances. Recently, nanostructured materials based on metal [6] - [16], dielectric [17] - [22], or semiconducting [23], [24] scatterers have been employed. These structures typically rely on plasmonic resonances [6] - [16], whispering gallery modes [17] - [19], [25] - [27], or Mie scattering [23]. While many advantages exist for these subwavelength structures, their size often requires micro- and nanoscale lithography or processing.

Light management layers are important for all solar cells to ensure that light enters the device and that the absorption occurs in a region of the device that leads to carrier generation and collection. It is also advantageous to make solar cells thin, typically on the order of the minority carrier diffusion length to ensure carrier collection. Thus, reflective back layers are often used to increase the optical path length of light, which can be achieved through the use of highly reflective metal, dielectric, or Bragg stack layers [28]. Additionally, light management layers can be used to direct the light into regions where the absorption will lead to current generation rather than non-radiative recombination, which is likely to occur in passivating window layers or near metal structures. These optimized light management layers will thus depend on the type of device (*e.g.*, absorption coefficient, carrier diffusion length, etc.), and are very important for thin-films; however, a good anti-reflection

coating (ARC) is necessary for all solar cells to ensure that light enters the device and enables absorption.

### 1.3 Traditional anti-reflection coatings

Anti-reflection coatings are widely used in a variety of applications ranging from eyeglasses and cameras to telescopes and solar cells. The basic principle is to reduce reflection, which can be achieved using a number of effects based on either coherent or incoherent reflection of light from surfaces. One of the first observations of an anti-reflection coating effect was by Lord Rayleigh in the late 1800s. The glass that was commonly used during that time period would tend to tarnish over time, developing a thin layer on its surface. Rayleigh observed that tarnished glass would transmit more light than a new, clean glass surface. The tarnished coating acted as an anti-reflection layer with an index of refraction intermediate between that of air and glass.

Today, most common anti-reflection coatings rely on thin-film interference effects to reduce reflection at the top interface of a solar cell. Traditional methods for anti-reflection coatings generally involve the deposition of single- or double-layer films in order to improve transmission by interference of the reflected light [29]. Figure 1.2 shows a schematic of a single-layer traditional anti-reflection coating.

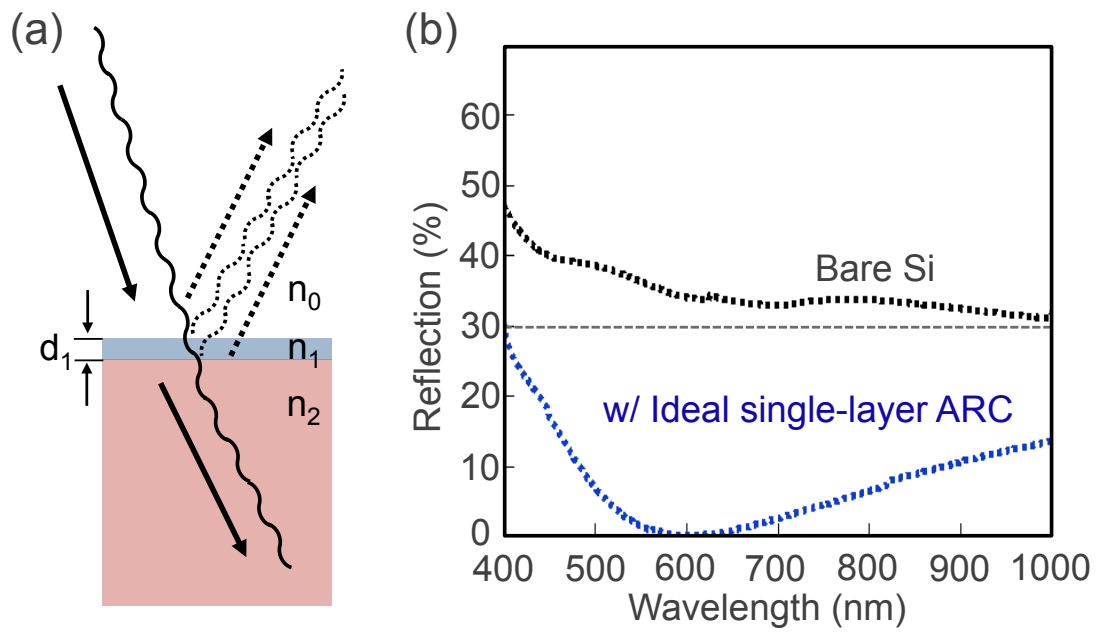


Figure 1.2: (a) Schematic showing a single-layer traditional anti-reflection coating. (b) The anti-reflection coating minimizes the light reflection effectively at a wavelength of  $\sim 600$  nm.

To minimize light reflection to air, the thickness of the traditional anti-reflection coating should be chosen to be one quarter of the wavelength of the incident light. For the best operation, the refractive index of that layer should be the geometric mean of that of the materials surrounding it (*e.g.*, air and substrate of the solar cell). With meeting those conditions, the reflected light after traversing the film is 180° out of phase with the light reflected off the first surface. This way, the reflected fields cancel, and the light is transmitted into the solar cell. The optimal conditions are

$$n_1 = \sqrt{n_0 n_2} \quad (1.3)$$

and

$$d_1 = \frac{\lambda_0}{4n_1} \quad (1.4)$$

where  $n_0$ ,  $n_1$ , and  $n_2$  are refractive index for air, the traditional anti-reflection coating, and substrate of the solar cell, respectively,  $d_1$  is the thickness of the traditional anti-reflection coating, and  $\lambda_0$  is a free space wavelength of the incident light.

Because these techniques rely on interference, they are typically optimized for a wavelength in the middle of the solar spectrum and perform poorly at wavelengths far from the optimum or for grazing angles of incidence. Further, these anti-reflection coatings are manufactured by film deposition techniques such as chemical vapor deposition (CVD), sputtering, or evaporation, which have many disadvantages in terms

of cost and the possibility of high temperature environments that are unsuitable for certain solar cell architectures. Thus, how cheaply and easily these layers can be made and how effective they are is of significant importance to future PV technologies.

One alternative to thin-film anti-reflection coatings is the use of metal or dielectric nanostructures [6] - [9], [12], [13], [15], [17] - [19], [23], [30] - [37]. The scattering properties of metal nanoparticles can be tuned by modifying their size, shape, or the surrounding environment and can lead to preferential forward scattering when placed on top of a high index substrate, such as a solar cell [38]. High index dielectric or semiconductor scattering objects can also yield improved forward scattering via coupling to Mie resonances [23], [39]. These structures have shown improved anti-reflection characteristics; however, they are generally more complicated to fabricate, as they rely on subwavelength structures that require microscale and nanoscale lithography.

## 1.4 Transparent paper-based anti-reflection coating

To circumvent the aforementioned difficulties, we present the use of an inexpensive and easy to process transparent paper for anti-reflection coatings (Chapter 3). The transparent paper, consisting of cellulose fibers, is used to reduce the index contrast between air and the semiconducting absorber layer, which ultimately increases light absorption within the solar cell. Furthermore, surface texturing of the cellulose leads to angle insensitive behavior over all wavelengths under consideration. Because of the ease of this process, the approach described here is a potential candidate for next generation ARCs that replace the conventional coatings, which rely on high-cost, vacuum deposition methods. Additionally, these cellulose materials are lightweight, flexible, and recyclable. These properties have allowed for the recent use of cellulose papers as substrates for polymer solar cells and batteries [40] - [45]. These renewable and sustainable materials have good mechanical properties, low densities, low thermal expansion, tunable optical properties, and low toxicity [40], [46] - [54].

The transparent paper, which is fabricated by a papermaking technique using TEMPO-treated micro-sized wood fibers, has excellent optical properties (Chapter 2). The paper used in this study not only has high optical transparency, but it also exhibits increased optical scattering. High transmittance allows most incident light to propagate through the paper and reach the active layer, while the optical scattering enables the possibility of increased path length. The scattering may be important for very thin solar cells; however, this feature is of less importance for

optically thick devices, typically made of Si, GaAs, etc.

## 1.5 Dielectric resonator-based anti-reflection coating

Silicon dioxide ( $\text{SiO}_2$ ) nanospheres offer a promising nanophotonic ARC option route due to its light trapping and scattering properties (Chapter 4). Further,  $\text{SiO}_2$  nanoscale structures are stable with respect to extreme temperatures and illumination and are commonly used in micro fabrication. Moreover,  $\text{SiO}_2$  is earth abundant. Different techniques have been used to achieve layers of  $\text{SiO}_2$  nanospheres on top of photo-active layers on flexible and rigid substrates, including the Langmuir-Blodgett method [19], [55], sedimentation [56], and controlled evaporation [57]. Despite the success in obtaining large areas covered with spheres, these approaches are not generally compatible with roll-to-roll processes, which are required for most continuous, mass production approaches.

The Meyer rod rolling technique has been used to deposit solution-based nanomaterials (i.e. graphene [58], silver nanowires [59], and carbon nanotubes [60]) on a variety of mechanical supports, including plastics, wafers, and glasses, enabling coatings for flexible electronics and energy storage devices. In this study, we use the Meyer rod rolling technique with an aqueous solution of  $\text{SiO}_2$  nanospheres and demonstrate that optical modes can be excited from incident illumination and lead to increased photocurrent in an underlying solar cell (Chapter 4).

## 1.6 Outline of this thesis

This thesis focuses on the use of non-resonant and resonant dielectric coatings for photovoltaics using (1) transparent cellulose fiber-based paper and (2) spherical dielectric micro-resonators. The following chapters are outlined as follows:

- Chapter 2 shows the characterization of the optical properties of the cellulose fiber paper used as an anti-reflection coating. Additionally, we describe the attachment process of paper to a typical solar cell.
- Chapter 3 describes the application of the cellulose-fiber paper coatings to various optoelectronic devices, specifically three solar cell materials: GaAs, Si, and P3HT, a common polymer solar cell material. Optical measurements are performed to determine the reduced reflection achieved with these coatings, and external quantum efficiency and current-voltage characteristics are used to determine the improvement in the power output and, hence, the efficiency increase.
- Chapter 4 focused on the use of nanoscale  $\text{SiO}_2$  spherical resonators to improve the performance of a Si solar cell. A detailed comparison is made between measurements of the optical and electrical response on the microscale and macroscale.

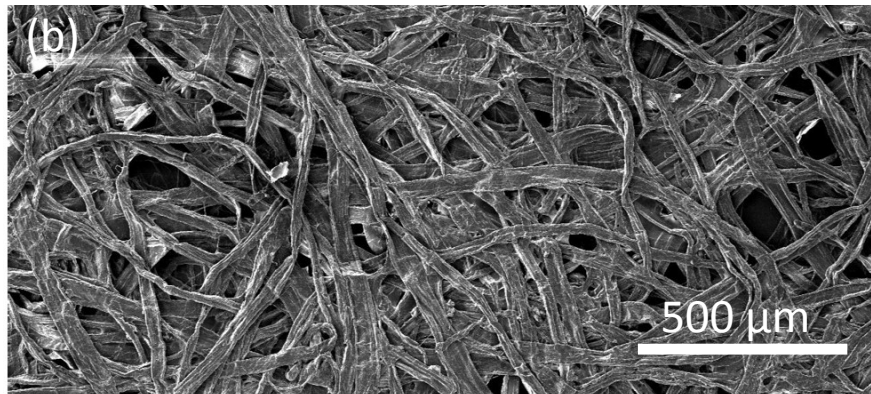
- Finally, Chapter 5 summarizes our findings and provides an outlook for future work.

Chapters 2 and 3 are based on material published in D. Ha *et al.*, “Paper-based anti-reflection coatings for photovoltaics,” *Advanced Energy Materials*, 4, 1301804 (2014) and D. Ha *et al.*, “Advanced broadband antireflection coatings based on cellulose microfiber paper,” *IEEE Journal of Photovoltaics*, 5, 577-583 (2015). Chapter 4 is based on a manuscript currently in review, D. Ha, *et al.*, “Demonstration of resonance coupling in scalable dielectric micro-resonator coatings for photovoltaics,” (*submitted and under review*).

## Chapter 2: Characterization of cellulose-fiber paper

### 2.1 Overview

In this chapter, we present the optical properties of a new ARC that is based on microscale cellulose fibers (Fig. 2.1). These fibers are constructed into a transparent paper that is able to scatter light at large angles, enabling increased optical path lengths and absorption within thin-film low-index solar cells (*e.g.*, polymer cells). For high-index solar cells, the path length enhancement is modest but can be improved if there is sufficient scattering at the paper-semiconductor interface. These transparent cellulose papers act as broadband ARCs that work over a wide range of incidence angles and are made in a simple inexpensive process using materials that are lightweight, flexible, and recyclable.



(c) Si solar cell with transparent paper ARC

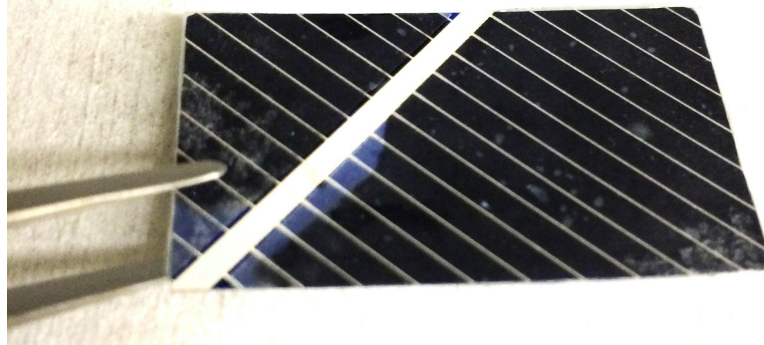


Figure 2.1: Transparent paper ARC. (a) Photograph of the transparent paper showing high transmission, yet large angular scattering. (b) SEM of the cellulose fibers that make up the transparent paper. (c) Textured monocrystalline Si solar cell with transparent paper ARC attached.

## 2.2 Transparent cellulose paper

Figure 2.1 shows an example of the cellulose paper used in these studies. The transparent paper is fabricated using TEMPO-treated micro-sized wood fibers through a papermaking technique [1], [61]. A 0.45 g TEMPO-oxidized bleached sulfate softwood pulp is dispersed into deionized water with a concentration of 0.1% by weight using a magnetic stirrer. The solution is stirred for 5 minutes to get a homogeneous suspension. The prepared pulp is then poured into a Buchner funnel with a filter membrane (Durapore Membrane, PVDF,  $0.65 \mu\text{m}$ ) to fabricate transparent paper by vacuum filtration. The film and filter membrane are placed between a stack of regular filter papers and dried under mechanical pressure. The paper has high optical transparency and also exhibits increased optical scattering (Figs. 2.1(a) and 2.2(b)).

The randomly oriented cellulose fibers have an average width of 20-30  $\mu\text{m}$  and a length of 0.8 mm, yielding a total average film thickness of 40-50  $\mu\text{m}$ . To create adhesion between the transparent paper and solar cells, a droplet of polyvinyl alcohol (PVA) is used. The capillary interaction creates a conformal coating even when a textured surface is used.

The high transmittance allows most of the incident light to propagate through the paper to reach the active layer. For very thin cells, the optical scattering enables the possibility of increased path length. The normalized scattering profile of the transparent paper ARC is shown in Fig. 2.2(b). The paper was illuminated from normal incidence with a tunable laser with wavelengths varying from  $\lambda = 500 \text{ nm}$

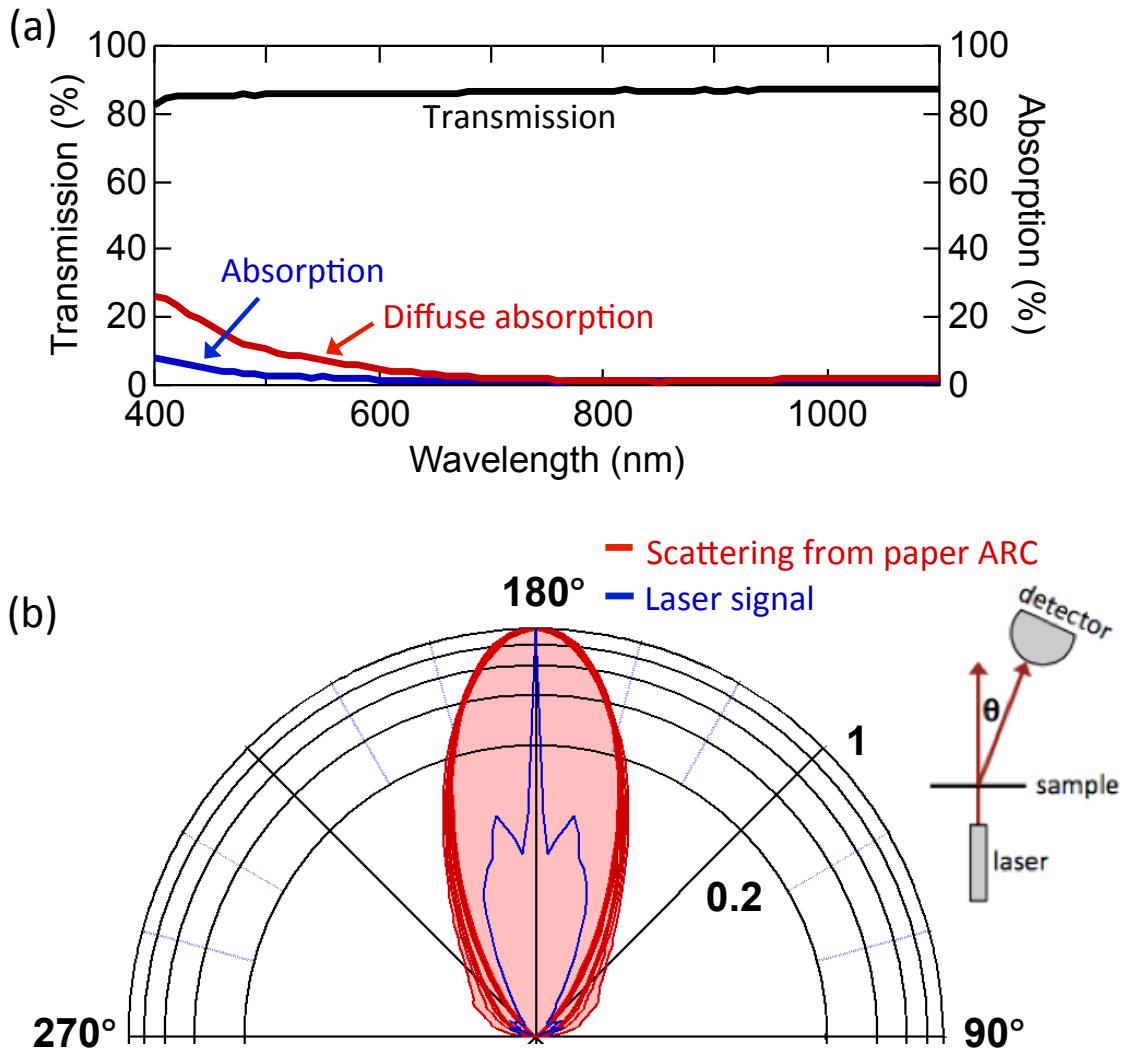


Figure 2.2: Optical properties of paper coating. (a) Wavelength-dependent transmission, absorption, and diffuse absorption data show that the paper has small absorption for normally incident light; however, the absorption is increased for diffuse illumination (*i.e.*, light incident from all angles). (b) Scattering profile under normal illumination from a tunable laser (blue) shows similar forward scattering performance (red) for all wavelengths measured (from 500 nm to 1000 nm).

to  $\lambda = 1100$  nm in 50-nm steps. The angular dependence of the transmitted signal was recorded after scattering from the paper. For comparison, the angular spread of the incident laser is shown (blue) in Fig. 2.2(b). There is significant scattering from the normal for all wavelengths considered, which illustrates that the paper ARC has broadband scattering properties from the visible to near-infrared range.

The transmission, absorption, and diffuse absorption of the paper were measured using an integrating sphere (Fig. 2.2(a)). High transmission and low absorption are found for normal incidence illumination. However, diffuse illumination results in increased absorption, especially for shorter wavelengths. As discussed in Chapter 3, this increased diffuse absorption leads to decreased performance for a textured device.

For the macroscale optical measurements (transmission, absorption, and diffuse absorption), a 150 W Xenon Arc lamp (6255, Newport Corp.) was coupled into a monochromator (500M, SPEX Industries, Inc.), and a 6-inch integrating sphere (Labsphere) was used. An integrating sphere is necessary to guarantee that all scattered light is detected. Figure 2.3 shows a picture of a measurement setup and Figure 2.4 shows a schematic illustrating the measurement configuration. The incident wavelength is selected using a computer controlled (Labview) monochromator. With an iris placed beside the output port of the monochromator, we can adjust the incoming light intensity and beam size. For lock-in measurements, the signal is chopped at a fixed frequency. The chopping frequency is fed to a DSP lock-in amplifier (SR830, Stanford Research Systems) for the reference signal. A beam splitter is used to split the light into two directions: one path goes to a reference photodetector

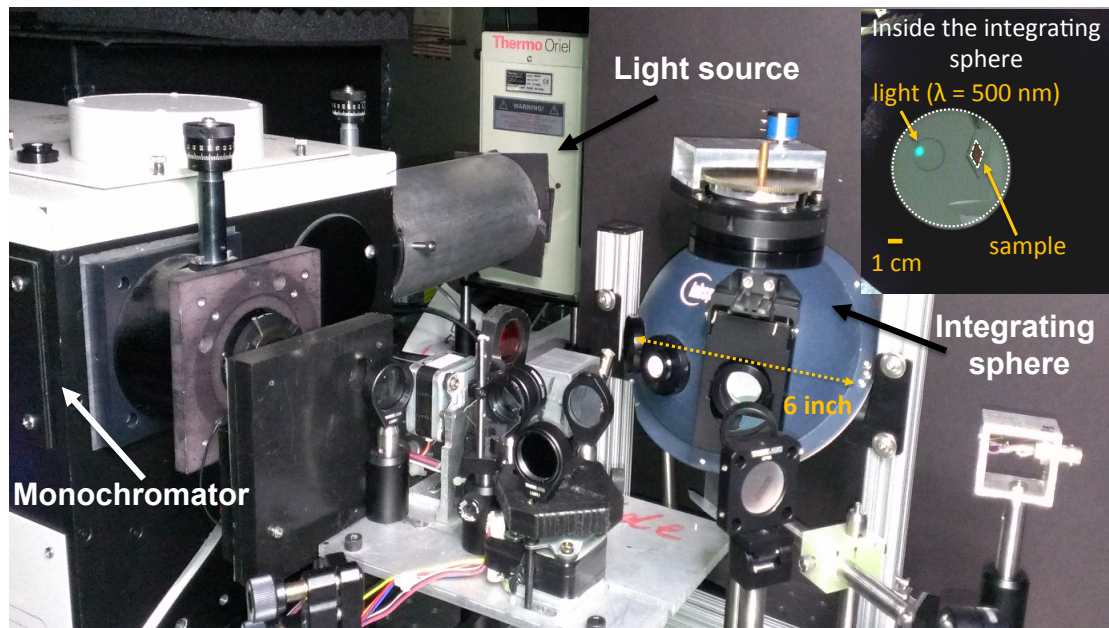


Figure 2.3: A measurement setup to determine optical properties. Inset shows the light at the wall of the integrating sphere, which is reflected from a GaAs solar cell at the wavelength of 500 nm.

and other goes toward the integrating sphere. The reference photodetector (in our case a Si photodetector) monitors the incident power ( $I_{ref}$ ), and it sends the signal to the relay. Light from the other path enters the integrating sphere after passing through various optical components, which enable the beam to be steered toward different ports on the integrating sphere or to a separate setup for quantum efficiency measurements. For the reflection data, the sample is positioned in the center of the integrating sphere and can be rotated for angle dependent measurements.

When the light enters the main port of the integrating sphere, the reflected light from the sample hits the wall of the integrating sphere, which is coated with a Lambertian paint, and then is scattered within the sphere. This light is finally captured by the photodetector placed at the bottom of the integrating sphere ( $I_{sig,port1}$ ). However, as this signal incorporates all secondarily reflected light components (*i.e.* components that reflect off the wall of the integrating sphere and return to the sample), we need to subtract these components from the measured signal ( $I_{sig,port1}$ ). For this work, we change the beam path so that the incident light, instead, enters the second port of the integrating sphere. In this configuration, we can make the incident light first hit the wall of the integrating sphere, and we can collect all secondarily reflected light from the sample with the photodetector placed at the bottom of the integrating sphere ( $I_{sig,port2}$ ). To calibrate the intensity difference between the light beams entering the two ports, we do a similar baseline measurement without the sample and record both intensities ( $I_{base,port1}$ ,  $I_{base,port2}$ ). All signals from two photodetectors are measured using a DSP lock-in amplifier (SR830, Stanford Research Systems).

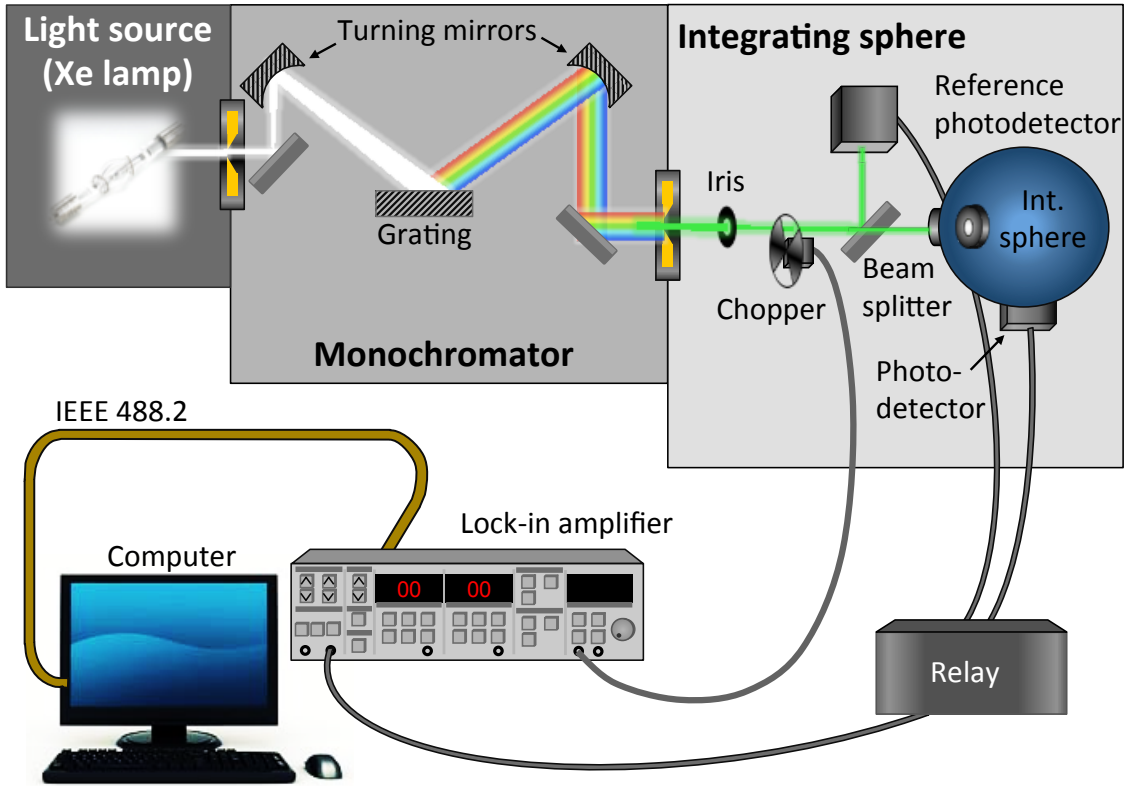


Figure 2.4: Schematic showing the optical measurement setup to determine transmission, absorption, and reflection.

The measured absorptivity in a sample within the integrating sphere is given by

$$A_{sample} = 1 - \frac{I_{sig,port1}}{I_{sig,port2} \times \frac{I_{base,port1}}{I_{base,port2}}} \quad (2.1)$$

and depends on the incident illumination angle and wavelength. In general, the absorptivity is related to the reflectivity ( $R_{sample}$ ) and the transmissivity ( $T_{sample}$ ) by

$$A_{sample} = 1 - (R_{sample} + T_{sample}). \quad (2.2)$$

When there is no transmission (*e.g.* when a back reflector is used),  $T_{sample} = 0$ , and the expression becomes:

$$A_{sample} = 1 - R_{sample}. \quad (2.3)$$

To measure the diffuse absorption (*i.e.* absorption that would occur due to a diffuse light source), we shine light inside the integrating sphere to obtain diffused light and measure the absorption of the sample. Because the sample is diffusely

illuminated in this case, the signal from the photodetector attached to the integrating sphere depends both on the intrinsic absorptivity and the sample size, which needs to be calibrated. There are three steps to determine the diffuse absorption of the sample. First, for calibration, the light intensity within the integrating sphere without the sample is measured. Second, optical intensities inside the integrating sphere with samples having different sizes but with known absorptivity (*e.g.* Si) are then measured. The diffuse absorption of materials with well-known absorptivity can be determined as follows

$$A_{diff,ref} = 2 \int_0^{\pi/2} T(\theta) \sin(\theta) \cos(\theta) d\theta \quad (2.4)$$

where  $T(\theta)$  is the transmission into the sample,  $\theta$  is the angle from the normal, and trigonometric terms represent the complete randomization. Third, we determine the diffuse absorption of the sample with unknown absorptivity by measuring the optical intensities inside the integrating sphere with samples having different sizes. The diffuse absorption of the sample then can be determined by comparing the measured calibration signals with the reference sample (*e.g.* Si) to the measured calibration signals with the sample having unknown absorptivity. Finally, these measurements result in the transmission, absorption, and diffuse absorption data presented in Fig. 2.2a.

To determine the durability of the transparent paper ARC under extended

solar illumination, the paper was exposed to the AM 1.5G solar spectrum for 168 h, which is equivalent to 21 days of illumination at 8 h per day (Fig. 2.5). No significant degradation in the optical transmissivity (averaged across the solar spectrum) was observed (*i.e.*, the change in transmission was found to be within the noise of the experiment  $< 1\%$ ). While future durability studies are needed, the transparent paper appears to be a versatile and robust material. Additionally, glass encapsulation should be considered for long-term applications, yielding further UV protection.

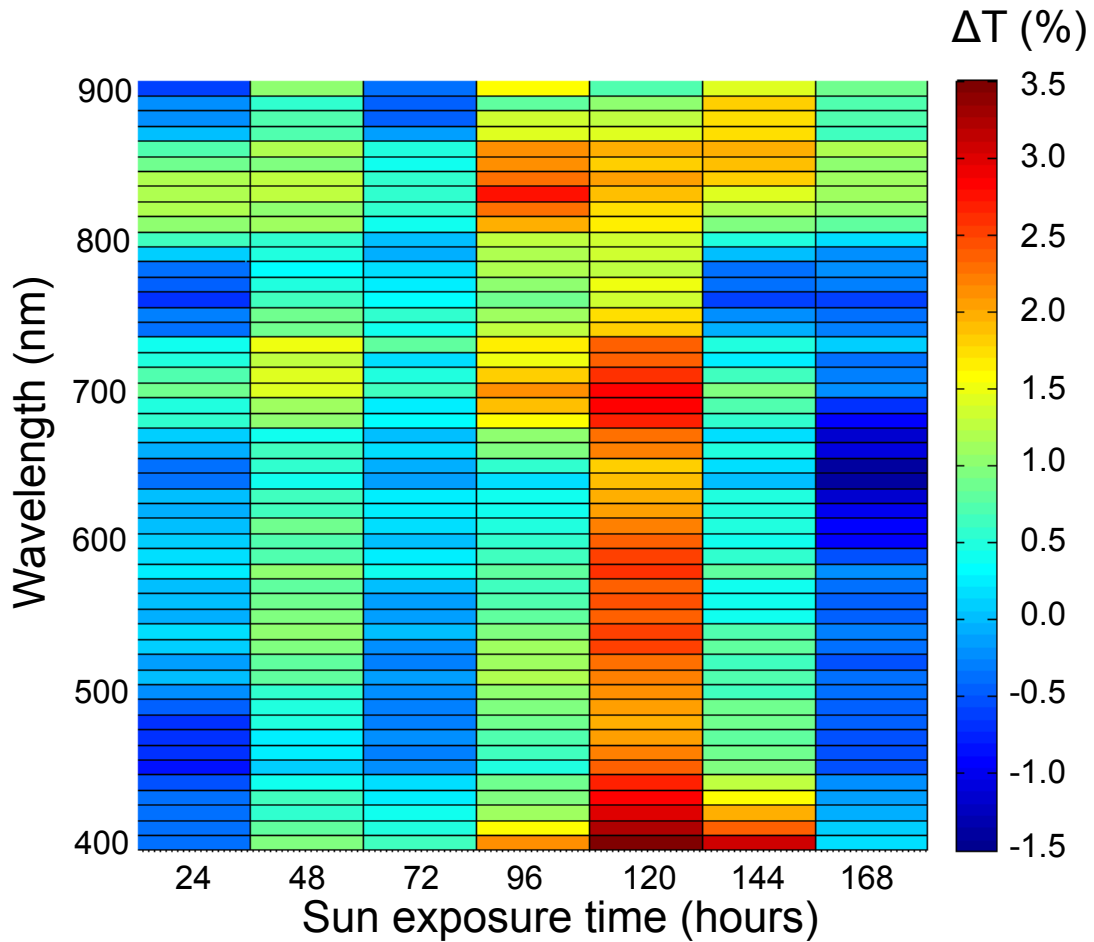


Figure 2.5: Change in transmission ( $\Delta T = T_{initial} - T_{hours\ of\ exposure}$ ) upon illumination in a solar simulator for 160 hours (equivalent of 21 days of AM 1.5 illumination at 8 hours per day) shows no significant degradation of the transmission over this timeframe.

### 2.3 Attachment on solar cells

In addition to the simplicity of fabrication, the paper can be easily attached (or removed) from the solar cell (Fig. 2.6). During the attachment process, polyvinyl alcohol (PVA) is used to ensure adhesion, and the paper can be detached by mechanical peeling from the cell. The transparent paper is cut into a rectangle with an area of  $1\text{ cm} \times 1\text{ cm}$  for attachment to the cell. To improve cohesive strength between the transparent paper and the GaAs cell,  $300\ \mu\text{L}$  of polyvinyl alcohol (PVA) solution (5% by weight) is used as a binder, and the trimmed transparent paper is carefully placed on the PVA-covered cell to assure that the transparent paper covers the entire active area. The laminated sample is then dried at room temperature.

Addition of the transparent paper ARC to a GaAs solar cell (M-Comm, the structure of the cell is shown in Fig. 3.1) results in reduced reflection over all angles and wavelengths throughout the visible spectrum (Fig. 2.7). The reflectivity is measured as a function of incident angle using an integrating sphere and monochromatic light. Figure 2.7 shows contour plots of the reflectivity as a function of incident angle (from  $10^\circ$  to  $55^\circ$ ) and wavelength (from 400 nm to 900 nm). Without the transparent paper, the GaAs solar cell generally reflects approximately 35-45% of the incident light (Fig. 2.7(a)); however, the addition of the transparent paper ARC reduces the reflection to approximately 15-25%. While a commercially available GaAs cell was used as a proof-of-principle demonstration, we show in Chapter 3 that this coating technique can be applied to virtually any solar cell architecture ranging from Si, which dominates the PV market, to new thin film and/or flexible technologies.

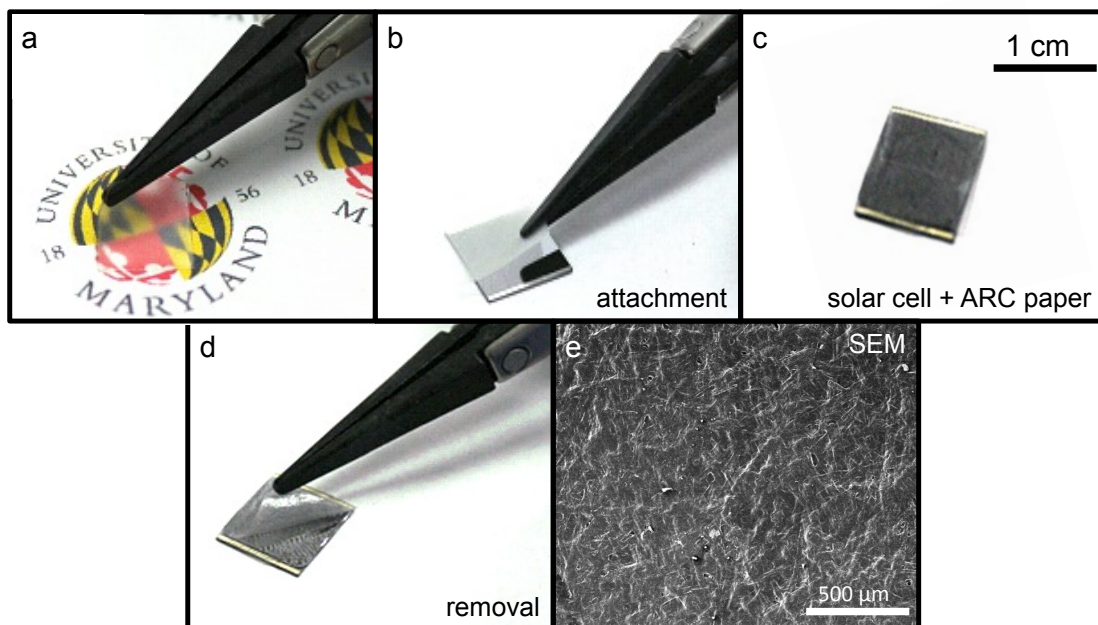


Figure 2.6: (a) The transparent cellulose paper. (b) Attachment of the transparent paper onto a GaAs solar cell using PVA. (c) The final cell with transparent paper on top. (d) Detachment can be performed as needed. (e) SEM image of the transparent paper showing cellulose fibers.

The angular dependence of the reflectivity is also interesting to consider if one wishes to avoid the need for mechanical tracking elements to align the surface normal of the solar cell with the incident light from the sun. The angular dependence of the reflectivity is also reduced when the transparent paper ARC is used (Fig. 2.7(a),(c)). We believe that this reduced angular dependence is due to the surface texturing of the paper, which increases the likelihood of light entering the ARC, even at steep angles.

The incident light was initially unpolarized; however, a slight polarization was created as a result of the optical path of the beam prior to it entering the integrating sphere. In order to account for this effect, the polarization was measured and the calculated reflectivity was corrected by weighting the two polarizations as shown in Fig. 2.7. This polarization calibration was also used in Fig. 3.5 in Chapter 3 to compare simulated and experimental results on Si devices. Figure 2.8 shows the polarization measurement for the experimental setup. Additional details about the polarization measurement can be found in Appendix A.1.

The reduction of the reflectivity can be explained using an incoherent reflection model and agrees well with the experimental data (Fig. 2.7). The transparent paper consists of cellulose fibers (with refractive index  $n = 1.47$ ) [62], which is very similar to that of PVA [63]. Because PVA is soaked into the transparent paper when processed, the refractive index of the mixture (transparent paper and PVA) is very similar to that of either the cellulose fibers or PVA alone. To better understand the enhancement in absorptivity, we consider an incoherent light propagation model based on the Fresnel equations with two different layers: the mixture of the trans-

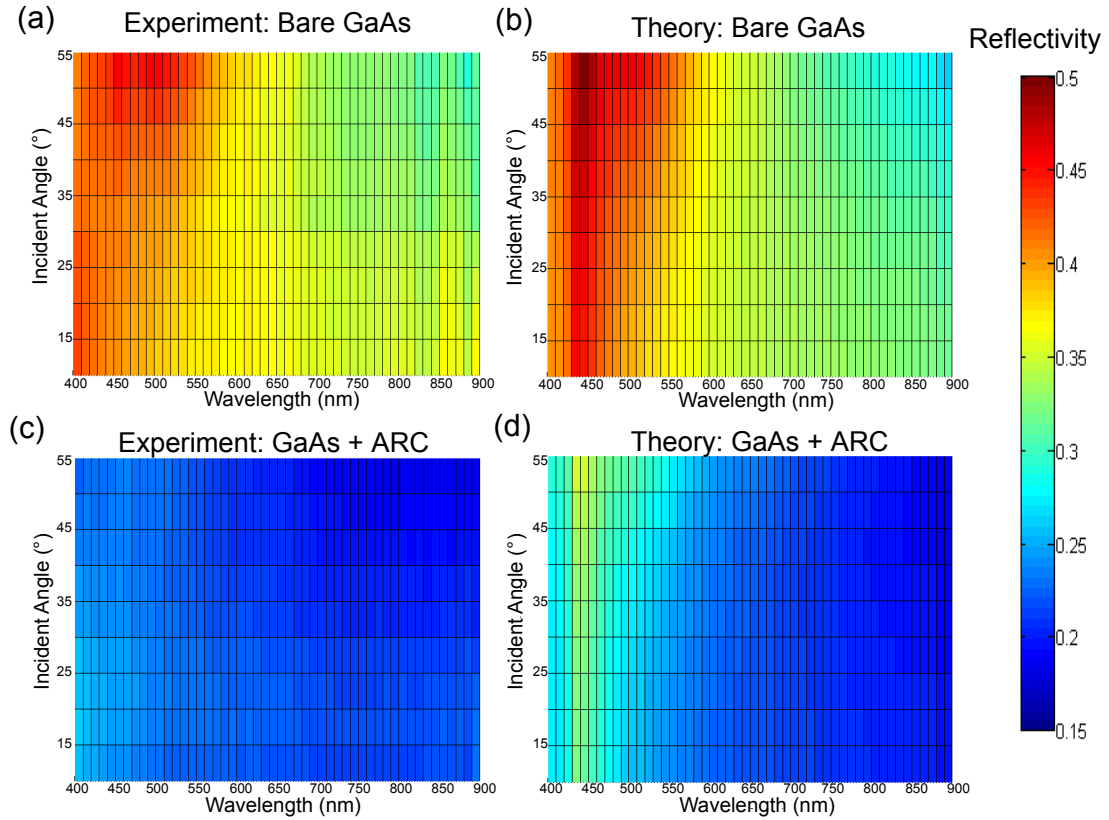


Figure 2.7: Transparent paper ARC reduces reflection over a wide range of incident angles and wavelengths. For the bare GaAs cell, contour plots of (a) measured and (b) calculated reflectivity as a function of incident angle (from  $10^\circ$  to  $55^\circ$ ) and wavelength (from 400 nm to 900 nm) are in close agreement. The addition of a transparent paper ARC greatly reduces the measured reflection (c) over all angles and wavelengths. Calculations using an incoherent reflection model accurately predict the expected reduction of the reflectivity (d). Differences between the experiment and the calculations near  $\lambda = 430$  nm are predominately due to differences in the optical properties of the GaAs used and are independent of the paper ARC.

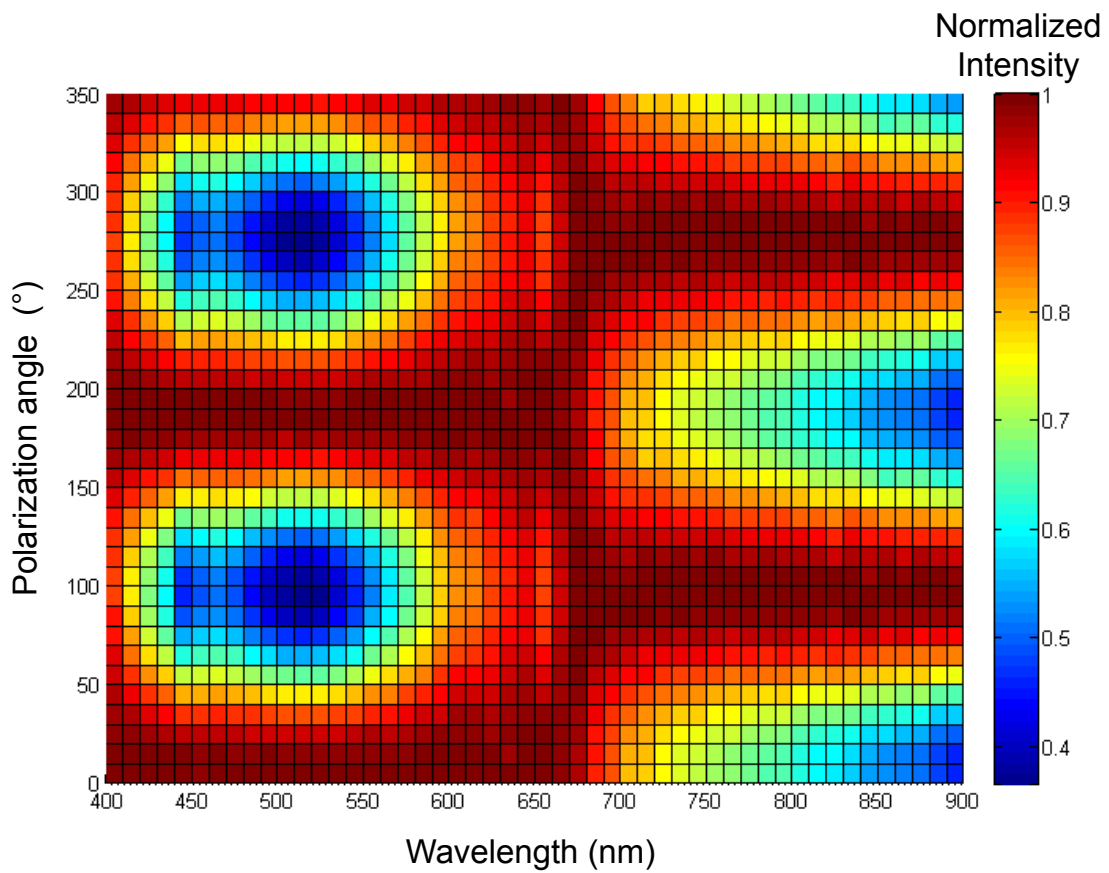


Figure 2.8: Calibration of polarization of incident beam. Contour plot of normalized intensity as a function of incident wavelength and polarization angle.

parent paper and PVA with a refractive index of  $\approx 1.47$  and the GaAs absorbing layer [64]. An incoherent model is used because of the texturing and the thickness of the layer rather than a coherent model, which would be appropriate for thin, flat films. At each incident angle, the reflectivity is calculated for each polarization and is given by

$$R_S = \left| \frac{n_1 \cos \theta_i - n_2 \cos \theta_t}{n_1 \cos \theta_i + n_2 \cos \theta_t} \right|^2 \quad (2.5)$$

and

$$R_P = \left| \frac{n_1 \cos \theta_t - n_2 \cos \theta_i}{n_1 \cos \theta_t + n_2 \cos \theta_i} \right|^2 \quad (2.6)$$

for  $S$ - and  $P$ - polarized incident illumination, respectively, where  $n_1$  and  $n_2$  are the refractive indices of the two media at the interface and  $\theta_i$  and  $\theta_t$  are the incident and transmitted angles from the surface normal. As discussed above, the slight polarization of our illumination source was determined and used to weight the calculated value of the reflectivity (Fig. 2.9). Because there are multiple reflections as the rays travel through the film, a geometric series is calculated to determine the total reflection (see Appendix A.2 for more detailed information about this model). Figure 2.9 shows that this incoherent model explains our data well. The calculation

shows a slight increase in the reflectivity around 430 nm for samples both with and without the transparent paper ARC, which is not observed in the experiment. This feature is independent of the ARC and is likely due to a difference in the GaAs index of refraction between that of Ref. [64] and of our actual sample.

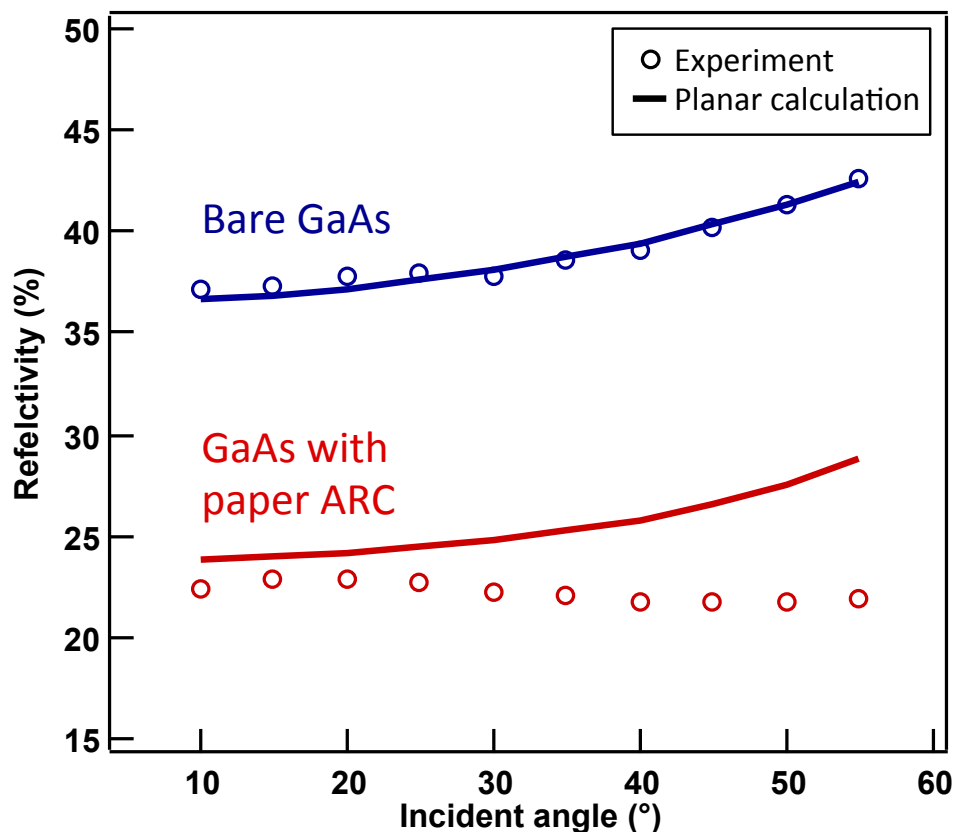


Figure 2.9: Measured (circles) and calculated (lines) reflectivity for both the bare GaAs cell (blue) and the GaAs cell with the transparent paper ARC (red) for  $\lambda = 550$  nm. For the cell with the paper ARC, the reflectivity is both reduced and angle independent.

## Chapter 3: Paper-based anti-reflection coatings on solar cells

### 3.1 Optoelectronic response of coated solar cells

In order to determine the effect of the transparent paper on a fully processed solar cell, the paper is transferred to two different types of devices: an untextured GaAs solar cell (M-Comm) and a textured monocrystalline Si solar cell (SensLite). Both devices show a significant decrease in the optical reflectivity. The flat untextured GaAs cell also shows a significant increase in the photocurrent as a result of the coating; however, the textured monocrystalline Si device shows a decrease in the photocurrent. This decrease is suspected to arise as a result of small amounts of absorption in the paper-based ARC, which are increased by the enhanced path length within the paper due to scattering from the textured pyramidal surface of the monocrystalline Si solar cell as described at the end of this chapter.

The schematic showing the structure of the GaAs solar cell is shown in Fig. 3.1. The GaAs solar cells were obtained from M-Comm, and the layer thickness and dopings are shown in Fig. 3.1. The cells were grown on an n-type GaAs wafer (300  $\mu\text{m}$  thick), and the active regions were cladded by AlGaAs passivation and back surface field layers. No traditional anti-reflection layer was used, because the added paper layer acts as the anti-reflection coating.

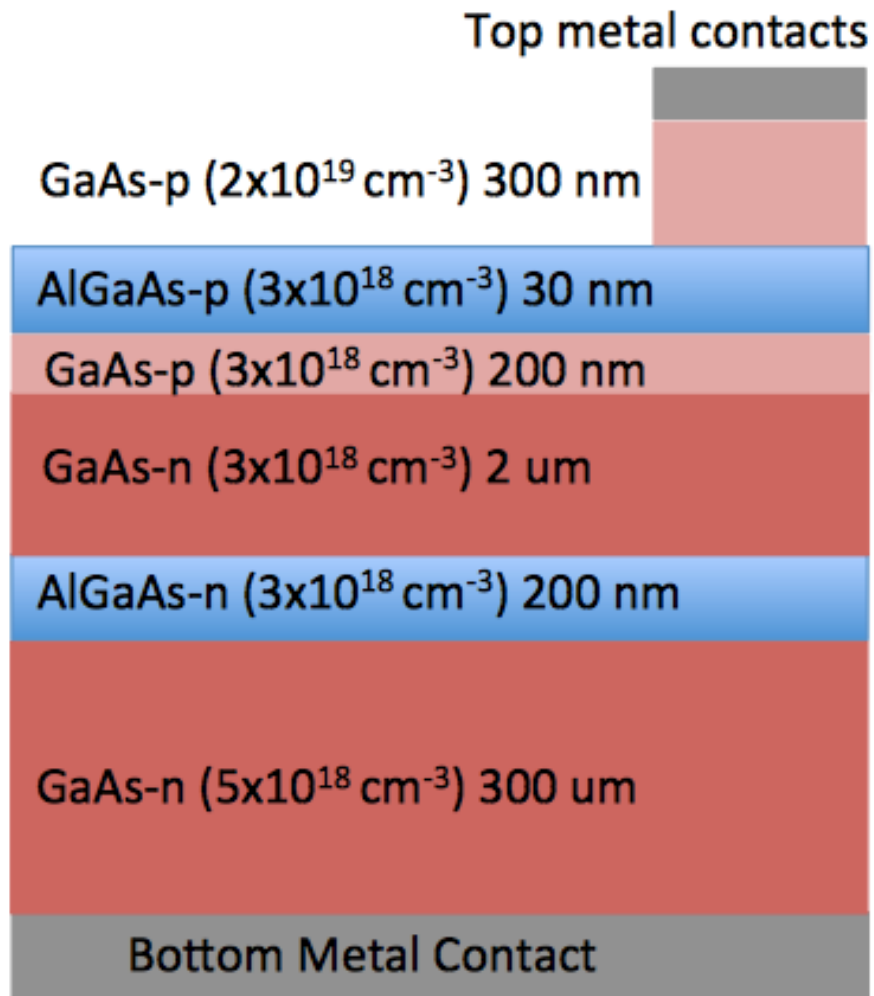


Figure 3.1: Schematic of the GaAs solar cell.

### 3.1.1 GaAs solar cell

In addition to the reduced reflectivity shown in Chapter 2, the addition of the transparent paper ARC also improves the external quantum efficiency (EQE) of the solar cell measured at zero bias (see Fig. 3.2). EQE is the ratio of collected electron-hole pairs to the number of incident photons:

$$EQE = \frac{\text{number of generated electrons/time}}{\text{number of incident photons/time}}. \quad (3.1)$$

Thus, we need two measurements to determine EQE of a solar cell. First, we measure the incident power arriving at the stage. Once we determine the current ( $I_{baseline}(\lambda)$ ) under light illumination with a calibrated photodetector having a responsivity of  $R(\lambda)$ , the incident power is determined as  $I_{baseline}(\lambda)/R(\lambda)$ . Simultaneously, we measure the photo-generated current from the solar cell ( $I_{sample}(\lambda)$ ) under the same illumination to determine the EQE for each wavelength:

$$EQE(\lambda) = \frac{\frac{I_{sample}(\lambda)}{q}}{\frac{I_{baseline}(\lambda)}{R(\lambda)} / \frac{hc}{\lambda}} \quad (3.2)$$

where  $\lambda$  is the wavelength,  $h$  is the Planck constant,  $c$  is the speed of light in a vacuum, and  $q$  is the charge of an electron. Figure 3.3 shows the EQE measurement

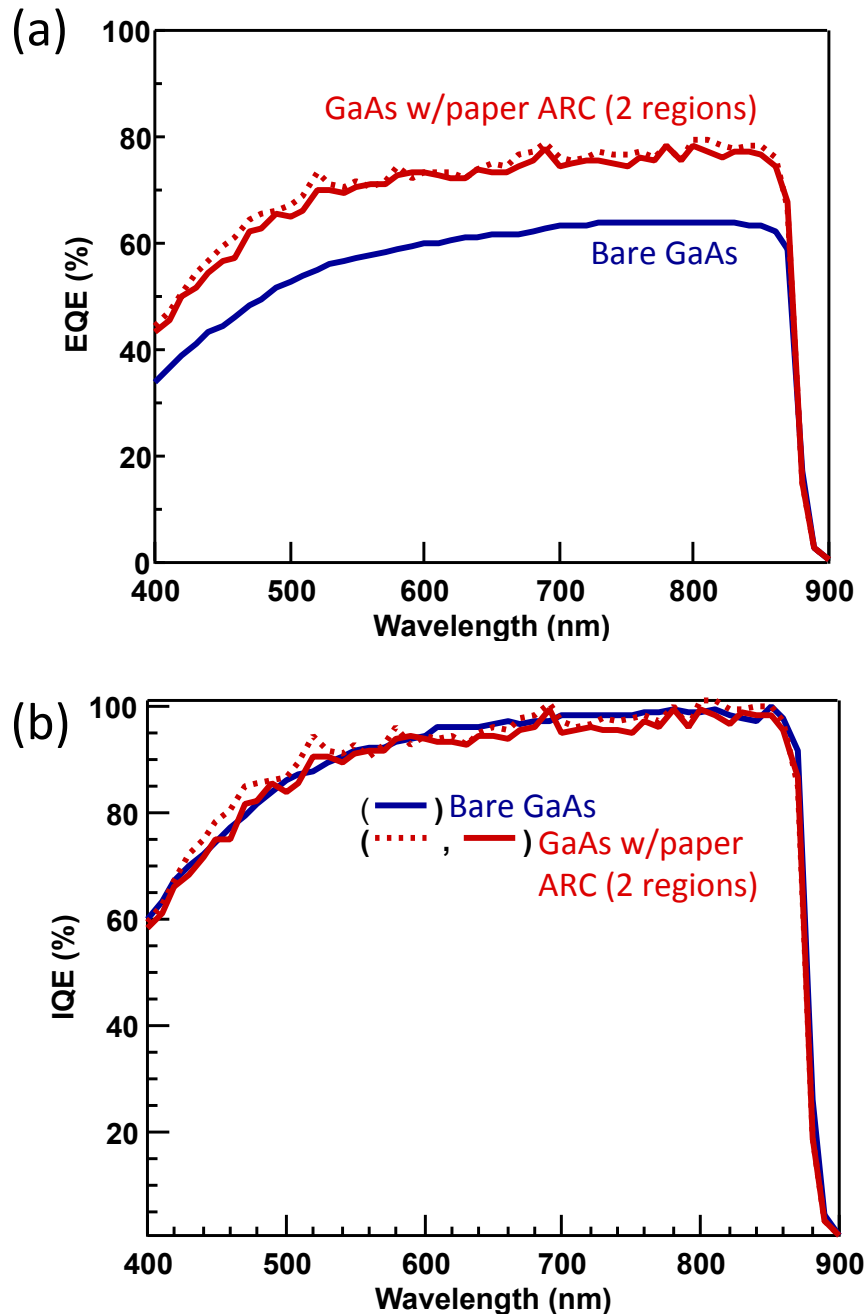


Figure 3.2: Quantum efficiency measurements for a GaAs solar cell with and without the ARC. (a) External quantum efficiency for the cell with the paper ARC (red) is improved over the entire wavelength range when compared to the bare GaAs cell (blue). (b) Internal quantum efficiency is unchanged upon the addition of the ARC, showing no detrimental effect on carrier collection. Both EQE and IQE are measured on multiple regions (dotted and solid lines) of the cell and show no significant deviations.

setup. Improved EQE is observed over the entire wavelength range from 400 nm to 900 nm. The enhancement in EQE throughout the entire wavelength range without any specific resonances is another indicator that the enhancement is not based on a simple anti-reflection effect but on the reduced index contrast and surface texturing.

The internal quantum efficiency (IQE) can be calculated by dividing the EQE by the absorptivity of the cell:

$$IQE = \frac{EQE}{Absorption}. \quad (3.3)$$

As the expression illustrates, IQE is an intrinsic electrical characteristic of the device. Thus, ideally the IQE should be the same for the solar cell with or without the transparent paper ARC. As shown in Fig. 3.2(b), the IQE of the two different solar cells are almost identical over the entire wavelength range, showing that the process had no detrimental effects on the device's carrier collection.

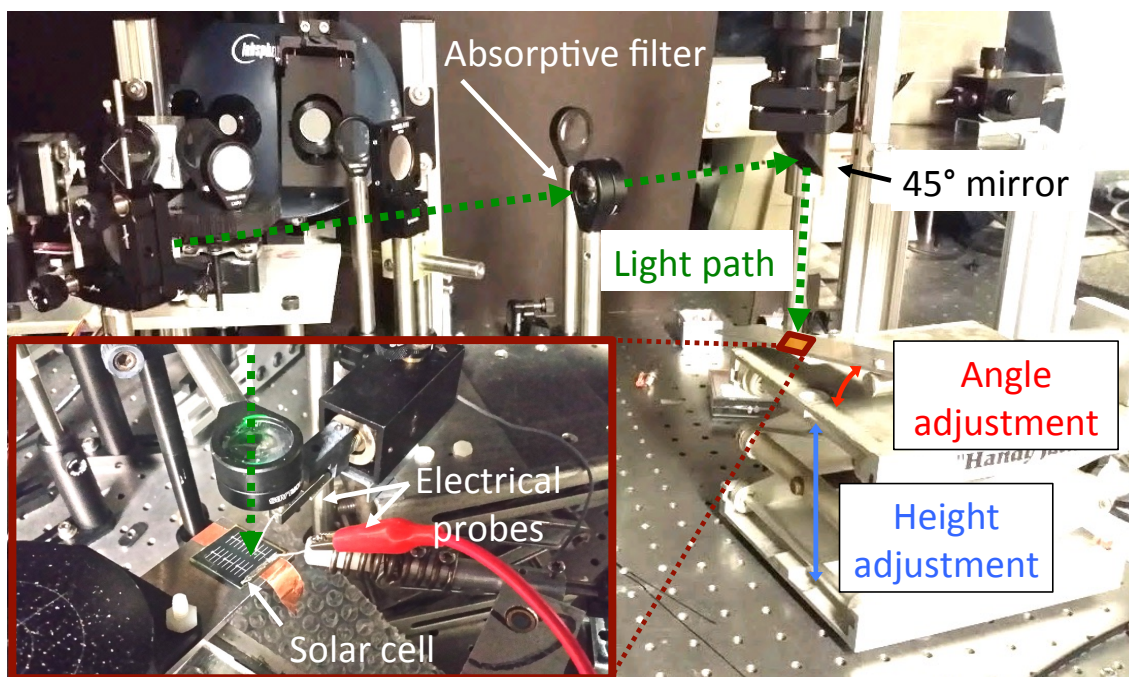


Figure 3.3: External quantum efficiency measurement setup. Green dotted line shows the beam path. Inset shows a solar cell under measurement at a wavelength of 500 nm.

The solar cell's efficiency is determined under AM 1.5G illumination using a solar simulator. A full spectrum solar simulator (Newport Model 91159) providing power equivalent of 1 sun is used for measurements. This 150 W Solar Simulator has a  $2 \times 2$  inch ( $50.8 \times 50.8$  mm) collimated output, and one Air Mass 1.5 filter. Using a LabView coded interface, we measure the solar cell performance and determine relevant figures of merit, such as short-circuit current density, open-circuit voltage, fill factor, etc. Figure 3.4 shows the measured current density-voltage ( $J$ - $V$ ) characteristics of the cell. The cell's electronic properties, which are extracted from the  $J$ - $V$  curve, are given in Table 3.1. With the transparent paper ARC on top of the GaAs cell, the total power conversion efficiency is improved by 23.8%, from  $\eta = 13.56\%$  to  $\eta = 16.79\%$ . The improvement is predominantly due to an increase in the short-circuit current density,  $J_{sc}$  (20.5%). A modest improvement in the fill factor,  $FF$  (2.6%) is also obtained; however, there is almost no change in the open-circuit voltage,  $V_{oc}$ . Because PVA has been used for attachment of the transparent paper to the GaAs cell, the electrical characteristics of the cell with PVA alone are also measured to see if the PVA affects the properties of the solar cell. There is almost no change in  $V_{oc}$  and a slight increase in the efficiency (5.6%), mostly arising from the enhancement in the photocurrent due to the thin PVA layer acting as a poor quality ARC. We thus conclude that the PVA has minimal effect on the solar cell and can be used as a suitable attachment material. The results are summarized in Table 3.1.

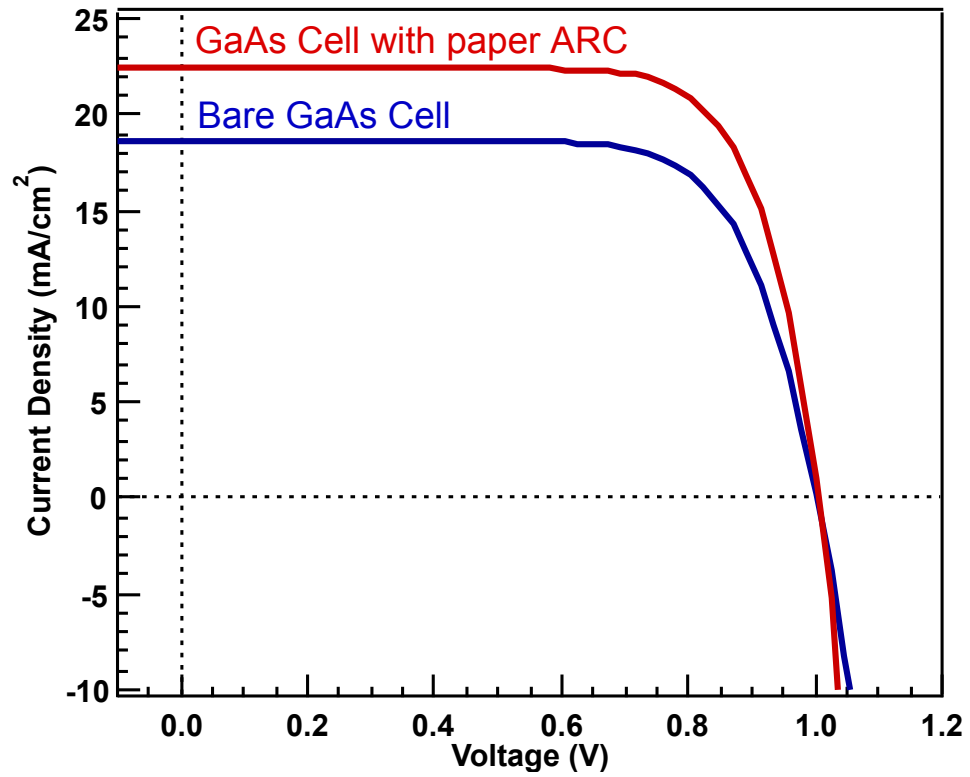


Figure 3.4: Current density vs. voltage characteristic for both the bare GaAs cell (blue) and the GaAs cell with the paper ARC (red). The addition of the paper ARC results in a 20.5% improvement in the short current density and a 23.9% improvement in the power conversion efficiency.

Table 3.1: Comparison of electrical properties between the bare GaAs cell and the GaAs cell with transparent paper ARC. Data represent the average of 7 measurements, and the uncertainties correspond to the standard deviation of the mean.

	$V_{oc}$ [mV]	$J_{sc}$ [mA/cm <sup>2</sup> ]	$FF$ [%]	$\eta$ [%]
Bare GaAs cell	$1001.9 \pm 0.3$	$18.67 \pm 0.01$	$72.5 \pm 0.5$	$13.55 \pm 0.10$
GaAs cell with paper ARC	$1004.0 \pm 0.5$	$22.49 \pm 0.01$	$74.4 \pm 0.2$	$16.79 \pm 0.03$
Enhancement from the bare GaAs cell [%]	0.21	20.46	2.62	23.91

### 3.1.2 Si solar cell

To determine the effect of the transparent paper ARC on the most common photovoltaic device architecture, we attach the transparent paper to both a flat Si wafer and to a monocrystalline textured Si solar cell, which results in reduced reflection over all angles and wavelengths throughout the visible spectrum (Fig. 3.5). The reflectivity is measured as a function of incident angle using an integrating sphere and monochromatic illumination. Figure 3.5 shows contour plots of the reflectivity, which are a function of incident angle (from  $10^\circ$  to  $55^\circ$ ) and wavelength (from 400 nm to 1000 nm). Without the transparent paper on top, the flat Si wafer generally reflects approximately 35-45% of the incident light (Fig. 3.5(a), top); however, the addition of the transparent paper ARC reduces the reflection to approximately 15-25% (Fig. 3.5(a), bottom).

Because most monocrystalline Si solar cells are processed to achieve pyramidal texturing for increased light incoupling, we also consider the effect of our transparent paper on these devices. Before application of the transparent paper ARC, the device's reflectivity is reduced (Fig. 3.5(b), top) in comparison with an untextured Si wafer (Fig. 3.5(a), top). The addition of the paper ARC to the textured Si solar cell further reduces the reflection (Fig. 3.5(b), bottom). Thus, the transparent paper ARC is able to reduce the reflection for both textured and untextured Si devices. This coating technique can be applied to virtually any kind of solar cell ranging from Si, which dominates the PV market, to next-generation thin-film and/or flexible solar cells.

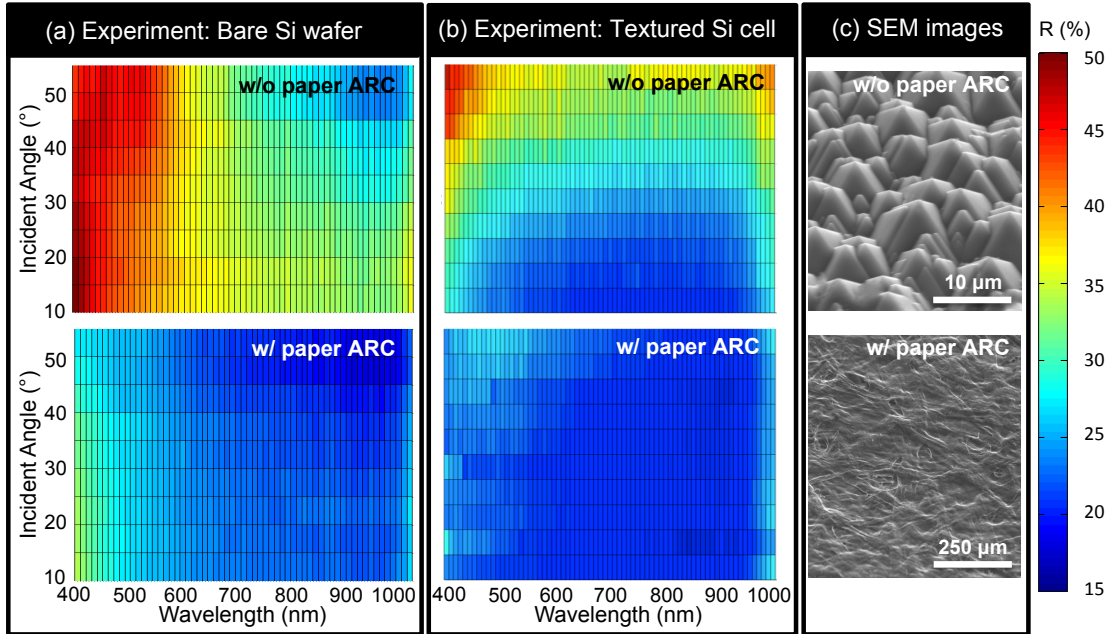


Figure 3.5: Transparent paper ARC reduces reflection over a wide range of incident angles and wavelengths when applied to a Si wafer or solar cell. (a) Measurements of the reflectivity of a bare Si wafer (top) and the same wafer after the application of the transparent paper ARC (bottom) as a function of incident angle (from  $10^\circ$  to  $55^\circ$ ) and wavelength (from 400 nm to 1000 nm). Contour plots show that the reflectivity is reduced for all wavelengths and incident angles. (b) Measurements of the reflectivity for a textured monocrystalline Si solar cell without (top) and with (bottom) the transparent paper ARC. Similarly, the reflection is reduced for all wavelengths and incident angles. (c) SEM of the top surface of the textured monocrystalline Si solar cell with pyramidal structuring on the surface (top). After attachment of the transparent paper ARC, the pyramidal structures are no longer visible and only the larger scale cellulose fibers can be seen (bottom).

The transparent paper ARC also shows little dependence on the incident angle of illumination, which reduces the need for a mechanical tracking system to align the surface normal of the solar cell with the incident light from the sun (Fig. 3.5). We attribute the reduced angular dependence to the surface texturing of the transparent paper ARC, which helps light enter this ARC even at steep angles.

The monocrystalline Si solar cell's efficiency was also determined under AM 1.5G illumination; however, despite the decreased reflectivity, the photocurrent was not enhanced (Fig. 3.6). To understand this surprising result, the optical properties of the paper and the scattering at the Si interface must be carefully considered. While the paper has high transmission, we found that it also absorbs approximately 2.1% of the incident light (averaged across the solar spectrum) when placed on a glass slide and measured using an integrating sphere. When the paper is placed on a flat surface, the path length is only enhanced slightly due to the texturing of the paper itself. However, when placed on top of the textured Si, the paper leads to increased wide angle backing scattering of the light as it is reflected off the Si surface. The increased path length within the paper can result in non-negligible absorption within the layer. This effect is clearly observable in the diffuse absorption measurement (Fig. 2.2), which shows increased absorption within the paper for light entering at non-normal incidence angles. The reflectivity is still reduced upon the addition of the paper ARC; however, a larger fraction of the absorption occurs in the paper when the Si layer is textured, leading to a decrease in the measured photocurrent. The electronic properties for both the bare monocrystalline Si solar cell and the cell with the paper ARC are shown in Table 3.2.

Table 3.2: Comparison of electrical properties between the bare Si cell and the cell with a transparent paper ARC.

	$V_{oc}$ [mV]	$J_{sc}$ [mA/cm <sup>2</sup> ]	$FF$ [%]	$\eta$ [%]
Bare Si cell	$563.9 \pm 0.3$	$28.02 \pm 0.02$	$57.3 \pm 1.0$	$9.05 \pm 0.20$
With ARC	$559.8 \pm 0.1$	$26.25 \pm 0.01$	$60.5 \pm 0.1$	$8.90 \pm 0.01$
Lossless ARC (Predicted)	$568.1 \pm 0.3$	$28.91 \pm 0.02$	$57.2 \pm 1.0$	$9.39 \pm 0.20$

In order to recover the advantageous anti-reflection properties of the paper when applied to a textured device, the absorption within the paper needs to be decreased. This can be achieved either by development of papers with less absorption or with papers that are thinner, which would decrease the optical path length. In order to calculate the expected performance improvement with such a paper ARC, we calculate the expected short-circuit current density increase upon application of the paper ARC based on the experimentally determined decrease in the reflectivity (Fig. 3.5(b)). Under AM 1.5G illumination,  $J_{sc}$  would be increased by  $0.89 \text{ mA/cm}^2$ , corresponding to a 3.2% increase in the  $J_{sc}$  over the bare cell. Figure 3.6(b) shows the  $J$ - $V$  characteristic for the textured Si solar cell without paper ARC, with paper ARC, and the expected  $J$ - $V$  characteristic if there were no loss in the paper. The expected  $J$ - $V$  curve is obtained by adding  $0.89 \text{ mA/cm}^2$  to the photogenerated current measured from the device without the paper ARC. In the same way, we can estimate the expected EQE of the device with the addition of a lossless transparent paper ARC on the textured Si solar cell. As shown in Fig. 3.6(a), the lossless transparent paper ARC applied to the textured Si solar cell would also improve EQE throughout the entire wavelength range for the solar cell (from 400 nm to 1100 nm). However, the enhancement is not remarkable compared with the GaAs solar cell because the textured bare Si solar cell already has good optical absorptivity at near normal incidence as shown in Fig. 3.5(b). Thus, adding this transparent paper ARC is not able to bring as large of an enhancement in EQE, when compared with the untextured cell at normal incidence.

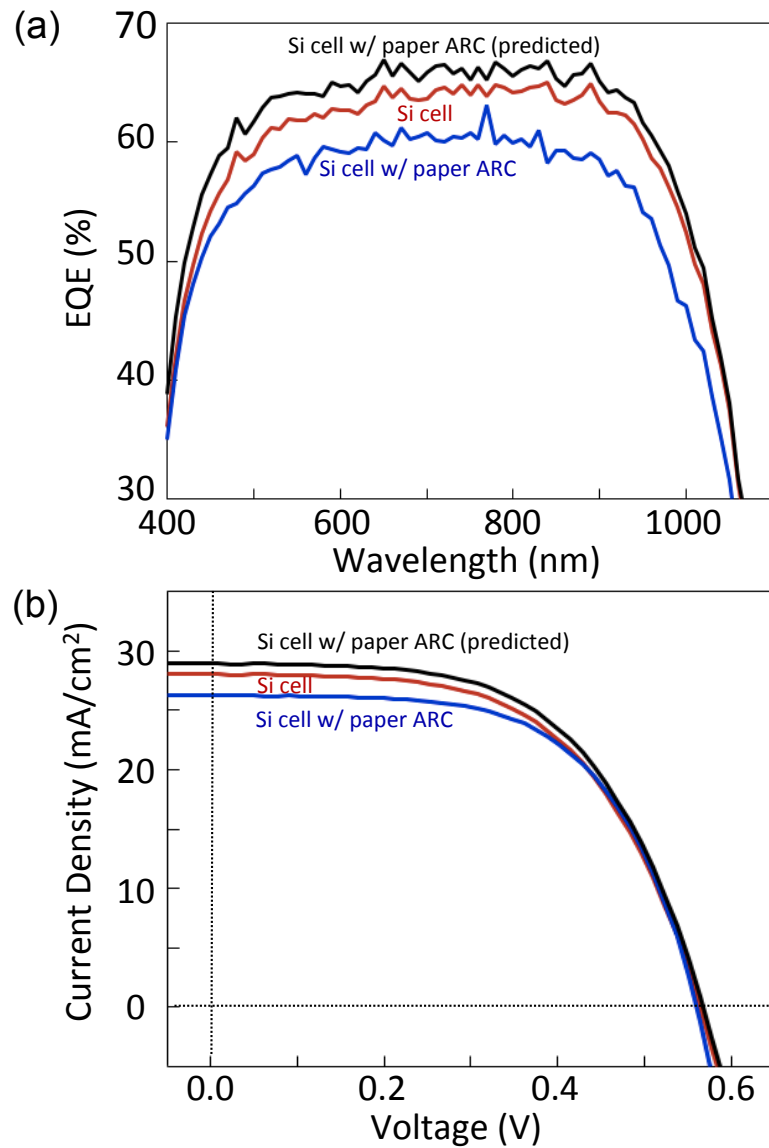


Figure 3.6: (a) EQE measurement on textured Si solar cell without the ARC (red) and with the ARC (blue). EQE without light loss within the paper ARC is also predicted (black). (b) For the textured monocrystalline Si solar cell, adding the transparent paper ARC reduced the cell's  $J_{sc}$  and the power conversion efficiency as a result of increased light absorption within the transparent paper ARC layer. For a thinner or less absorbing paper, the  $J_{sc}$  could be increased to  $28.9 \text{ mA/cm}^2$  (compared with  $28.0 \text{ mA/cm}^2$  for the device without ARC) as determined from the decrease in the measured reflectivity. We predict that the efficiency would reach 9.4%, an improvement of 3.8%.

## 3.2 Paper-based anti-reflection coatings on a low index of refraction substrate

Due to the difference in the refractive index between the paper ARC and the GaAs or Si substrate, it is difficult to reduce reflection below  $\sim 15\%$  without grading the index or increasing the scattering at the interface. For a lower index substrate (*e.g.*, P3HT, a common polymer solar cell material), the paper ARC can have improved performance due to a more optimal index contrast. To further investigate this idea, we performed reflection measurements on P3HT with and without the paper ARC (Fig. 3.7). To prepare the sample, a droplet of the P3HT solution was spun onto glass, and a thickness of  $\sim 60$  nm was achieved, as determined by ellipsometry. This paper ARC effectively reduces light reflection throughout the entire wavelength range of interest for this polymer (from 400 nm to 700 nm). In this range, the solar spectrum-weighted light reflection was reduced from 17.0% to 13.7% with the addition of the paper ARC, corresponding to an  $\sim 20\%$  overall reduction. To determine how much the reduced reflection depends on the index contrast alone, the reflection was calculated under the simplifying assumption of no scattering using the well-known matrix transfer method [65] where the P3HT was treated as a coherent layer and the paper and glass were treated as incoherent layers. The glass was assumed to have an index of 1.5, the paper, an index of 1.47, and the P3HT, a wavelength dependent index derived from [66]. Despite the small discrepancy in the magnitude between the experiment and calculation, it is clear that the paper ARC

can perform well even on a lower index substrate. The difference between the experiment and calculation is likely due to the difference between the refractive indices of the P3HT layer in the calculations and the experiments and due to scattering by the paper, which is not included in the calculation. For shorter wavelengths (from 400 nm to 450 nm), the effect of the paper ARC is not significant in the calculation. In this wavelength range, the refractive index of P3HT is slightly lower than the paper ARC, and thus, the reduced index contrast from air to the polymer is not obtained. For this reason, light reflection becomes slightly larger. By contrast, the decreased reflection measured experimentally in this range is likely due to light scattering within the paper ARC.

While additional improvement is needed for these paper-based coatings to surpass the normal incidence performance of interference-based coatings, there are many advantages to the cellulose paper ARCs. From a manufacturing point of view, this room temperature fabrication process has the potential to reduce manufacturing costs. From an optical point of view, the angular independence of the paper-based ARC gives additional competitiveness to this technique, as it reduces the need for solar tracking.

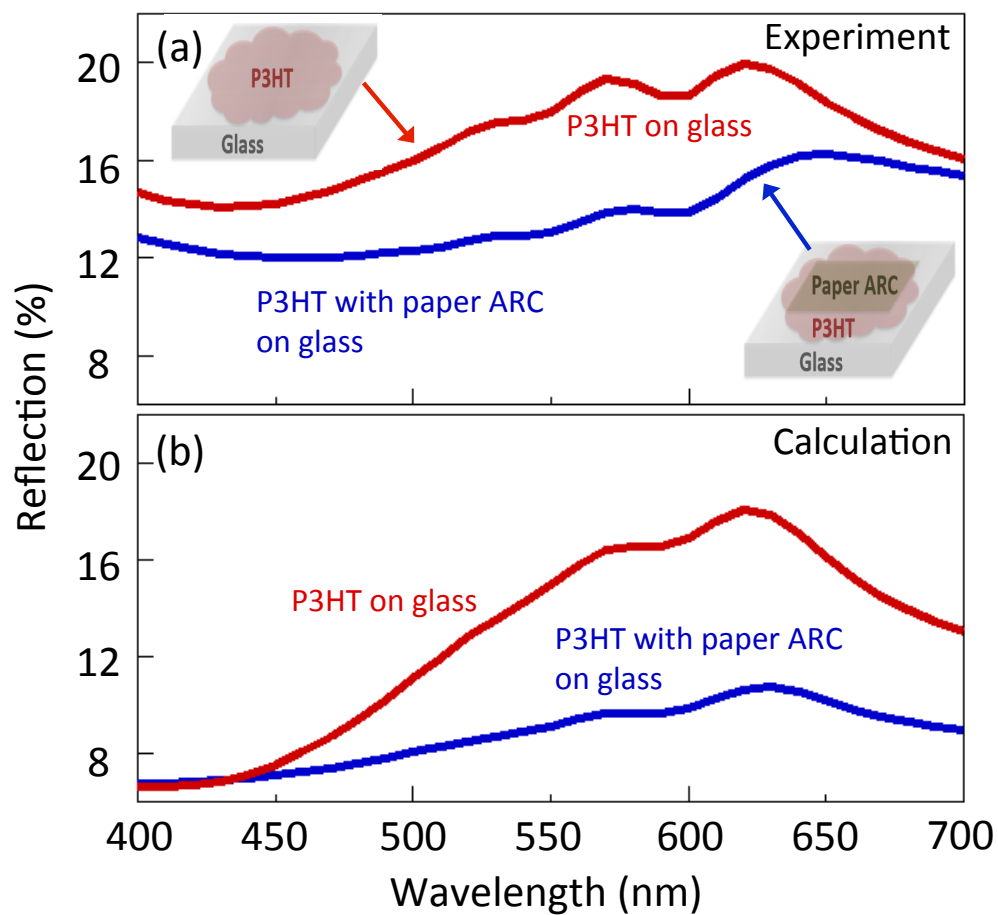


Figure 3.7: Reflectivity of a polymer (P3HT) on glass is reduced upon the addition of a paper ARC, showing potential application for thin-film organic photovoltaic devices. Experimental results (a) are in general agreement with predictions (b) based on a transfer matrix method (neglecting scattering).

### 3.3 Conclusion

In conclusion, we have observed improved optical response from solar cells using a novel transparent paper-based anti-reflection coating. The paper leads to a significant decrease in the reflectivity independent of incident illumination angle for both textured and untextured cells. An increase in the power conversion efficiency for the untextured cells is also observed; however, cells with surface texturing have reduced power conversion efficiencies due to an increase in the absorption within the paper ARC resulting from an increased path length within the coating. This study also shows the need for testing beyond simple reflection measurements to determine the effects of potential ARCs. Despite drawbacks on devices with textured surfaces, this new type of ARC offers a simple, earth abundant material option and a room-temperature deposition process, making this technique an excellent candidate for planar solar cell technologies. Additionally, thinner transparent papers could provide superior performance for textured devices by further reducing the loss within the paper.

## Chapter 4: Dielectric micro-resonators

We present an effective and potentially scalable ARC for PV based on SiO<sub>2</sub> dielectric nanospheres deposited by the Meyer rod rolling technique, which produces broadband absorptivity enhancement of > 15% when applied to Si solar cells. The highly periodic configuration of the SiO<sub>2</sub> nanospheres leads to the excitation of particular optical modes within the structure, which produces distinct electric field distributions that strongly indicate the presence of whispering gallery modes within the nanospheres.

## 4.1 Fabrication steps

Here we employ a water-based process to assemble a monolayer of silicon dioxide nanospheres on a substrate by the Meyer rod rolling technique, which produces close-packed arrays with high density coverage. To generate a close-packed monolayer of SiO<sub>2</sub> nanospheres, a surfactant (*e.g.* Zonyl) is added to the nanosphere suspension to prevent their aggregation. The suspension containing nanoparticles is then spread on the top of a semiconducting substrate and a dense monolayer of SiO<sub>2</sub> nanospheres assembles during the drying process (see Appendix B.1 for more detailed information about the Meyer rod rolling technique). Figure 4.1 shows a schematic illustrating the concept of the Meyer rod rolling deposition. Figure 4.2(a)-(c) shows the steps required to obtain a close-packed monolayer of spheres with diameter of 500 nm and coverage area of  $\sim 67\%$ , as shown in Fig. 4.2(d). This coverage can be improved through further optimization of the coating technique; however, the achieved coverage is sufficient to demonstrate the optical resonances, as presented in this chapter.

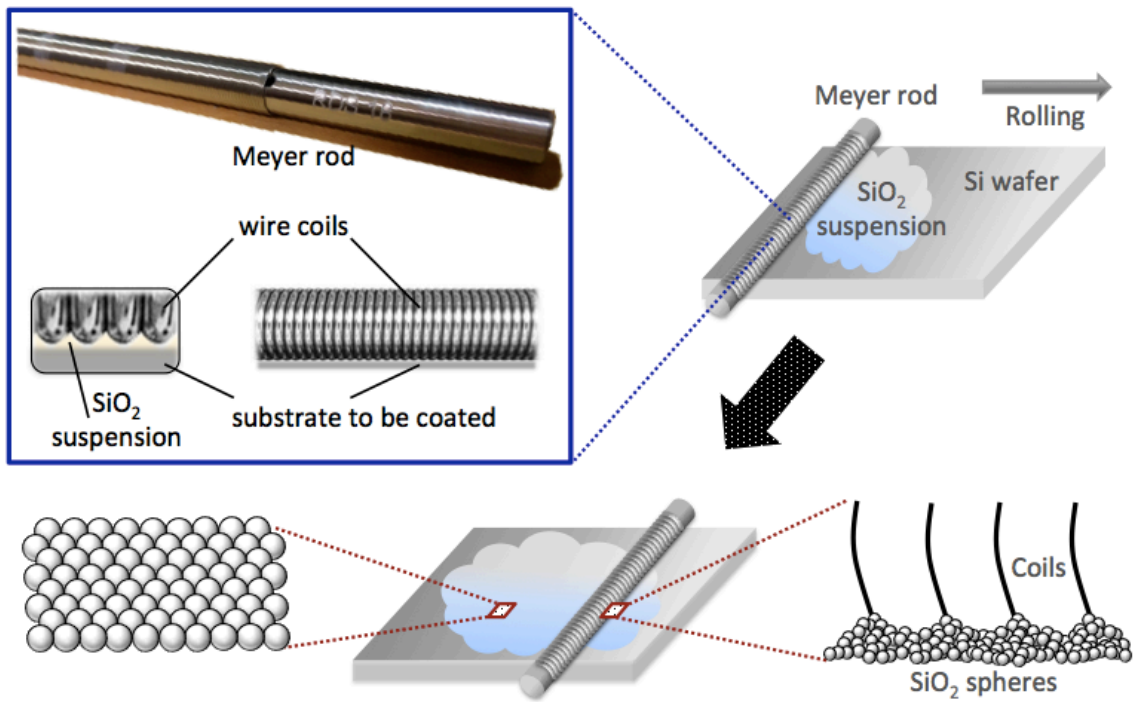


Figure 4.1: Schematic showing the deposition process using a Meyer rod rolling technique

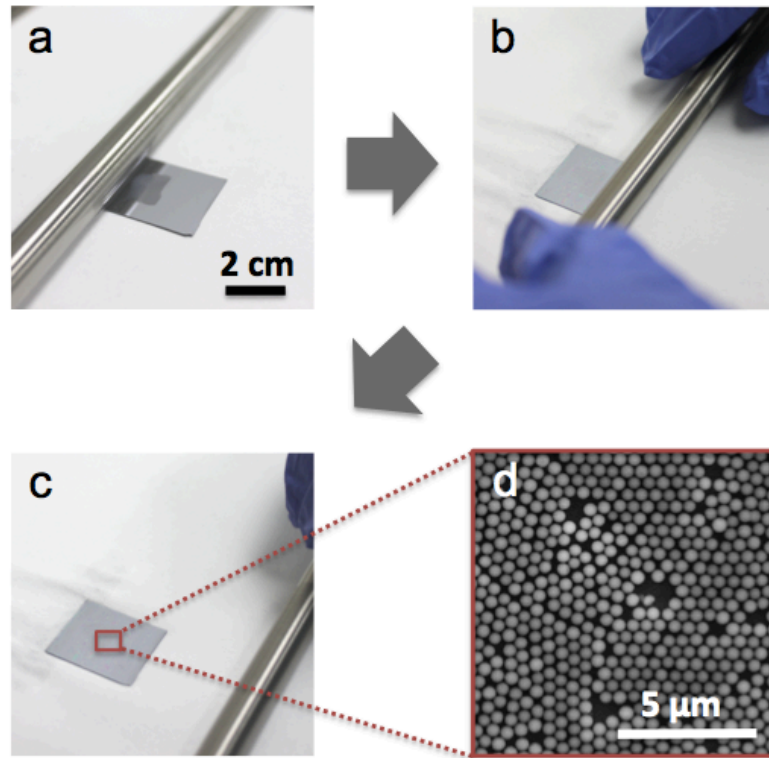


Figure 4.2: (a)-(c) Photographs depicting the fabrication steps for the  $\text{SiO}_2$  dielectric nanosphere coating. A Meyer rod is pulled along the surface of a Si wafer with a droplet of suspension containing  $\text{SiO}_2$  nanospheres. The sample is then submitted to a mild annealing treatment, at  $50^\circ\text{C}$  for 1 min for water evaporation. (d) SEM image showing one monolayer of  $\text{SiO}_2$  nanospheres on a Si substrate.

## 4.2 Simulations of optical response

The Finite-Difference Time-Domain (FDTD) method was used to simulate the optical response of the dielectric spheres. We assumed close-packed SiO<sub>2</sub> nanospheres on a Si substrate, where the absorptivity of the Si substrate was calculated from its reflection. We applied periodic boundary conditions horizontally within the simulated volume (or a Bloch boundary condition when a plane wave source was propagating at an angle) to simulate a periodic structure and a perfectly matched layer boundary condition was used at the bottom of a Si substrate (see Fig. 4.3). Optical constants required for simulations were obtained from [64].

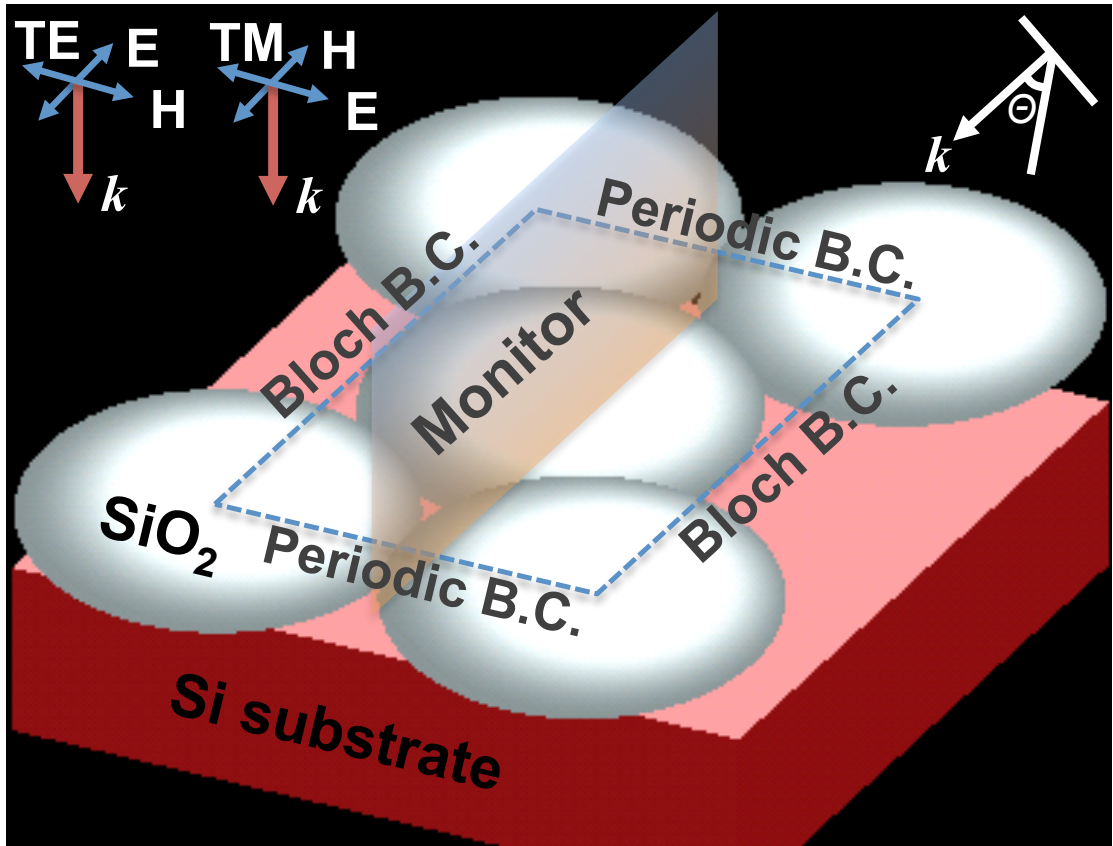


Figure 4.3: The boundary conditions as well as the simulation structures. The definition of polarization in the structure and angle of incidence are also shown.

### 4.3 Optical enhancement due to nanospheres

The SiO<sub>2</sub> nanosphere ARC results in increased absorption throughout the solar spectrum as determined from experiments (Fig. 4.4). An integrating sphere and monochromatic light are used to measure the absorptivity as a function of angle of incidence and wavelength for both a bare Si reference wafer (Fig. 4.4(a)) and a Si wafer with the nanosphere ARC (Fig. 4.4(c)). The addition of the SiO<sub>2</sub> nanosphere layer leads to both broadband and narrowband absorption enhancements throughout the visible spectrum that vary with incident wavelength and illumination angle from the surface normal.

One simple explanation for the increased absorption is that the spheres constitute a new thin-film layer that acts as an anti-reflection coating whose index of refraction varies with thickness based on the weighted-average of the index at each height above the Si slab's surface (Fig. 4.5). The calculated absorption of a Si wafer without any coating (Fig. 4.5(a)) is compared to the absorption resulting from a close-packed layer of SiO<sub>2</sub> nanospheres (500 nm diameter) atop a Si wafer (Fig. 4.5(b)) and to the absorption occurring in a Si wafer coated with the modeled effective index thin-film (Fig. 4.5(c)). Broadband enhancements occur for both the sphere array and the thin-film coating; however, only the sphere array leads to narrowband absorption features (Fig. 4.5(b)). All calculations were performed using the Finite-Difference Time-Domain (FDTD) method. This explanation accounts for the two broadband absorption enhancement regions that occur at  $\sim 500$  nm and  $\sim 750$  nm at normal incident and shift to slightly shorter wavelengths for larger in-

cident angles (Fig. 4.5).

However, additional narrowband peaks (*e.g.*, the absorption peak that occurs at  $\sim 600$  nm in the experimental data for an incident angle of  $10^\circ$ , which shifts to longer wavelengths at higher angles) cannot be explained by this simple model. In order to better understand the origins of the narrowband resonances, simulations are performed, and contour plots of absorption are obtained (as a function of incident illumination wavelength and angle) for a thick Si slab with and without the nanosphere coating (Fig. 4.4(b),(d)). Simulations are performed for both polarizations to match the unpolarized light from the experiment. The simulations accurately describe the experimental data, including the absence of any sharp resonances for the bare Si. Fig. 4.4(d) shows the calculated absorption in a Si slab with a close-packed layer of  $\text{SiO}_2$  spheres, which is in good agreement with the experimental data shown in Fig. 4.4(c). In addition to the broadband absorption regions discussed above, the nanosphere coating also leads to regions with narrowband absorption, highlighted by white ellipses in Fig. 4.4(c),(d).

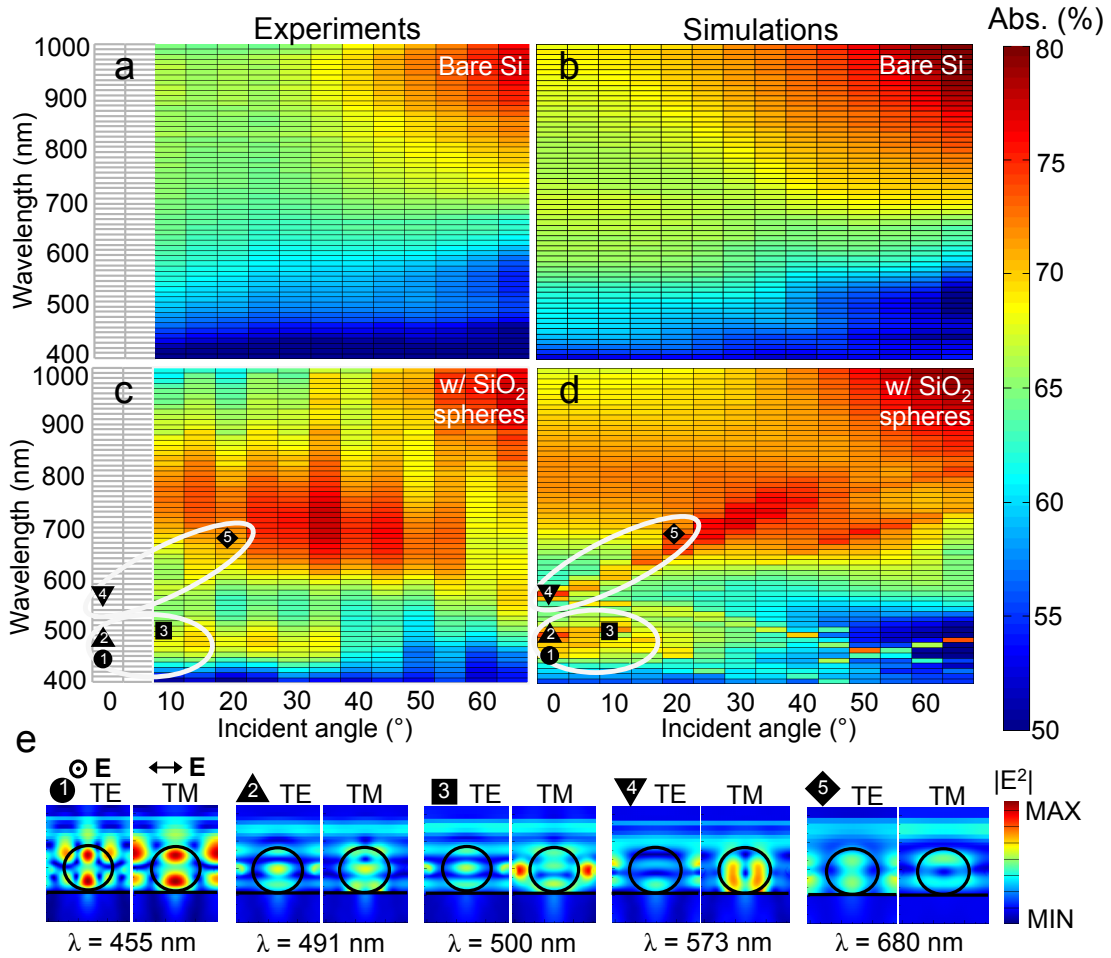


Figure 4.4: Contour plots showing (a),(c) experimental and (b),(d) simulated absorptivity as a function of both wavelength (from  $\lambda = 400$  nm to 1000 nm) and angle of incidence (from  $\theta = 0^\circ$  to  $65^\circ$ ) of incoming light for (a),(b) a bare Si wafer and (c),(d) a Si wafer with a close-packed monolayer of SiO<sub>2</sub> nanospheres. All calculations are based on the FDTD method. There is no experimental data for incident angles  $< 10^\circ$  due to geometric constraints that are typical of integrating sphere systems. (e) Electric field profiles for data points numbered (1)-(5) in (c),(d) are shown for each polarization.

The electric field intensities for each polarization (transverse magnetic (TM) and transverse electric (TE)) are displayed in Fig. 4.4(e) for each numbered point in Fig. 4.4(c),(d). The electric field profile of the TM mode from point 4 ( $\lambda = 573$  nm at normal incidence) strongly suggests the excitation of whispering gallery modes inside the sphere [17] - [19], as confirmed by the field intensity profile (Fig. 4.4(e)). These modes couple with each other, most likely due to the close proximity of the spheres, which allows for light scattering from one to another, ultimately leading to a significant increase in the electric field strength within the periodic array of nanospheres [25] - [27], [67] - [69]. These enhanced fields then couple into the high-index absorbing material (Si wafer), leading to waveguiding in thin films [70].

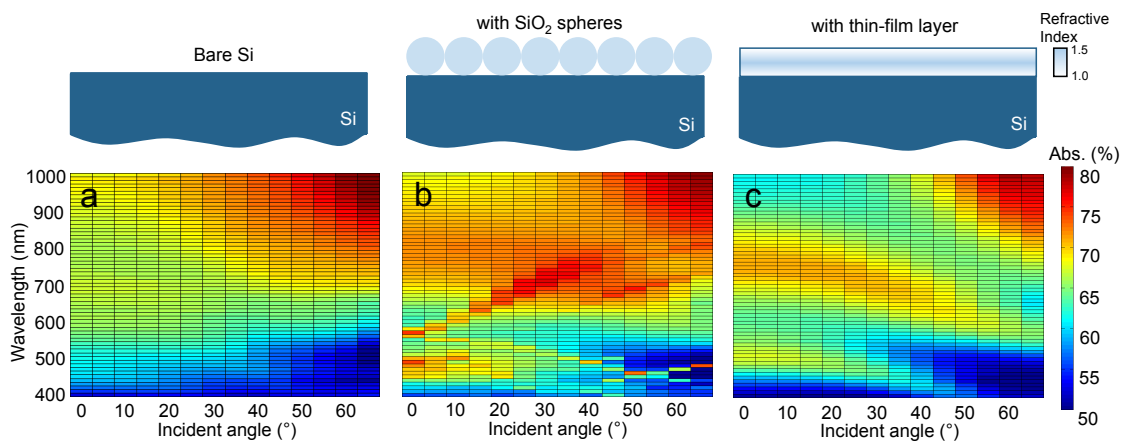


Figure 4.5: Calculated absorption within a Si wafer with (a) no coating, (b) a coating consisting of a close-packed layer of SiO<sub>2</sub> nanospheres, and (c) a thin-film coating layer with an effective index of refraction corresponding to the average index at a given height above the Si wafer.

#### 4.4 Coupling of whispering gallery modes into the absorbing layer

To determine whether whispering gallery modes in each SiO<sub>2</sub> nanosphere actually coupled into the Si absorbing layer, we probe the electric field intensity just inside the Si absorber. Figure 4.6(a),(b) show the field intensity from normal incidence illumination at resonances 1 ( $\lambda = 455$  nm) and 4 ( $\lambda = 573$  nm), and Fig. 4.6(c) shows the field intensity off resonance ( $\lambda = 600$  nm). Resonances 1 and 4 (shown in Fig. 4.4(e)) are not accessible with the experiment because they occur at normal incidence, but these resonances show a focusing effect (Fig. 4.6(a),(b),left) that leads to increased semiconductor absorption. Figure 4.6(b) shows two high intensity lobes on each side of the sphere, similar to the profile of the whispering gallery mode of an isolated sphere [18]. The electric field intensity both at the interface (red solid line) and 50 nm below (red dotted line) is much stronger than that of off resonance excitation (Fig. 4.6(c),  $\lambda = 600$  nm). Because significant energy is captured inside the spheres, light eventually leaks into the high-index absorbing substrate (*i.e.*, Si wafer) beneath it, where it is absorbed.

To test the effect of the SiO<sub>2</sub> monolayer ARC on an optoelectronic device, we simulate the expected spectral current density of a solar cell with this coating (Fig. 4.7). To determine how much the current density is increased, the AM1.5G solar spectrum-weighted current density,  $J$ , is calculated for the cases with and without SiO<sub>2</sub> nanospheres atop a substrate. The total current density is calculated based on

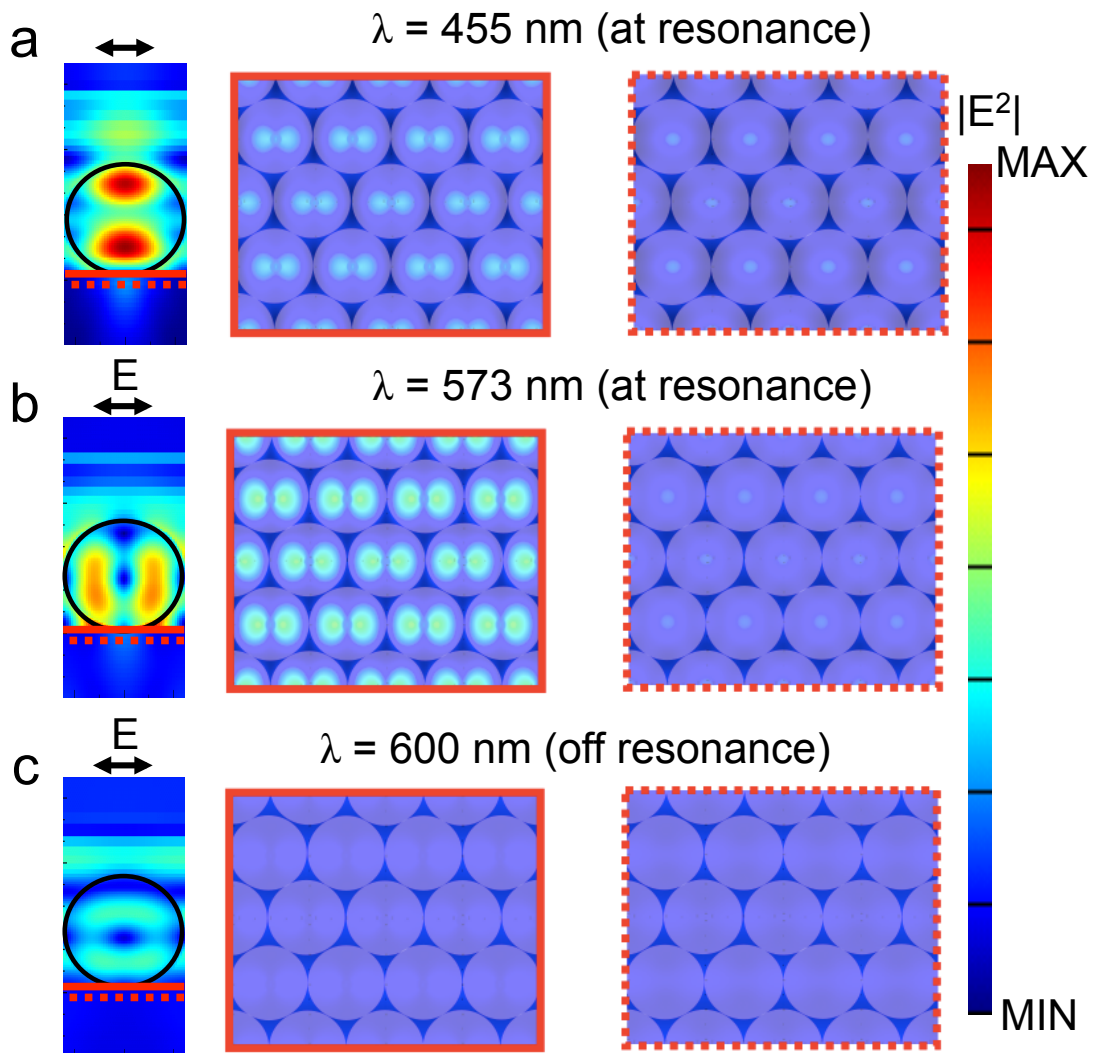


Figure 4.6: Electric field profiles at resonances resulting from illumination at (a)  $\lambda = 455$  nm and (b)  $\lambda = 573$  nm. High fields are observed inside the  $\text{SiO}_2$  nanosphere, which couple into the Si substrate. Lateral field profiles at the top of the Si substrate (red solid line) and 50 nm below the interface (red dotted line) show increased intensities within the Si for the resonant wavelengths (455 nm and 573 nm). (c) Electric field profiles for off resonance illumination ( $\lambda = 600$  nm), where no specific, strong field enhancements are observed.

the following expression:

$$J = q \int S(\lambda)\eta_{EQE}(\lambda)d\lambda \quad (4.1)$$

where  $q$  is the electron charge,  $S(\lambda)$  is the AM1.5 solar intensity per unit wavelength, and  $\eta_{EQE}(\lambda)$  is the external quantum efficiency (EQE) of the device. For this calculation,  $\eta_{EQE}(\lambda)$  is obtained from the absorptivity within the Si substrate, assuming perfect internal quantum efficiency (IQE) for the wavelengths of interests in our calculation for simplicity. Figure 4.7 shows the calculated absorptivity, the AM1.5G solar intensity, and the calculated spectrally resolved current density. The absorptivity enhancement due to the previously described resonances ( $\lambda = 455$  nm and 573 nm, see Fig. 4.6(a),(b)) results in higher spectral current density. For a bare Si cell (black line), the total integrated current density (from  $\lambda = 400$  nm to the bandgap of Si,  $\lambda = 1100$  nm) is  $27.71 \text{ mA/cm}^2$ . With the addition of the close-packed SiO<sub>2</sub> nanospheres coating, the spectral current density (blue line) increases to  $29.75 \text{ mA/cm}^2$ , a  $\sim 7.4\%$  improvement over that of a bare cell. As expected, the spectral current density at  $\lambda = 600$  nm (off resonance, see Fig. 4.6(c)) is much lower than the current density at either of the resonant peaks. Thus, we expect that this new ARC yielding high absorptivity enhancement can significantly increase photo-generated current for optoelectronic devices.

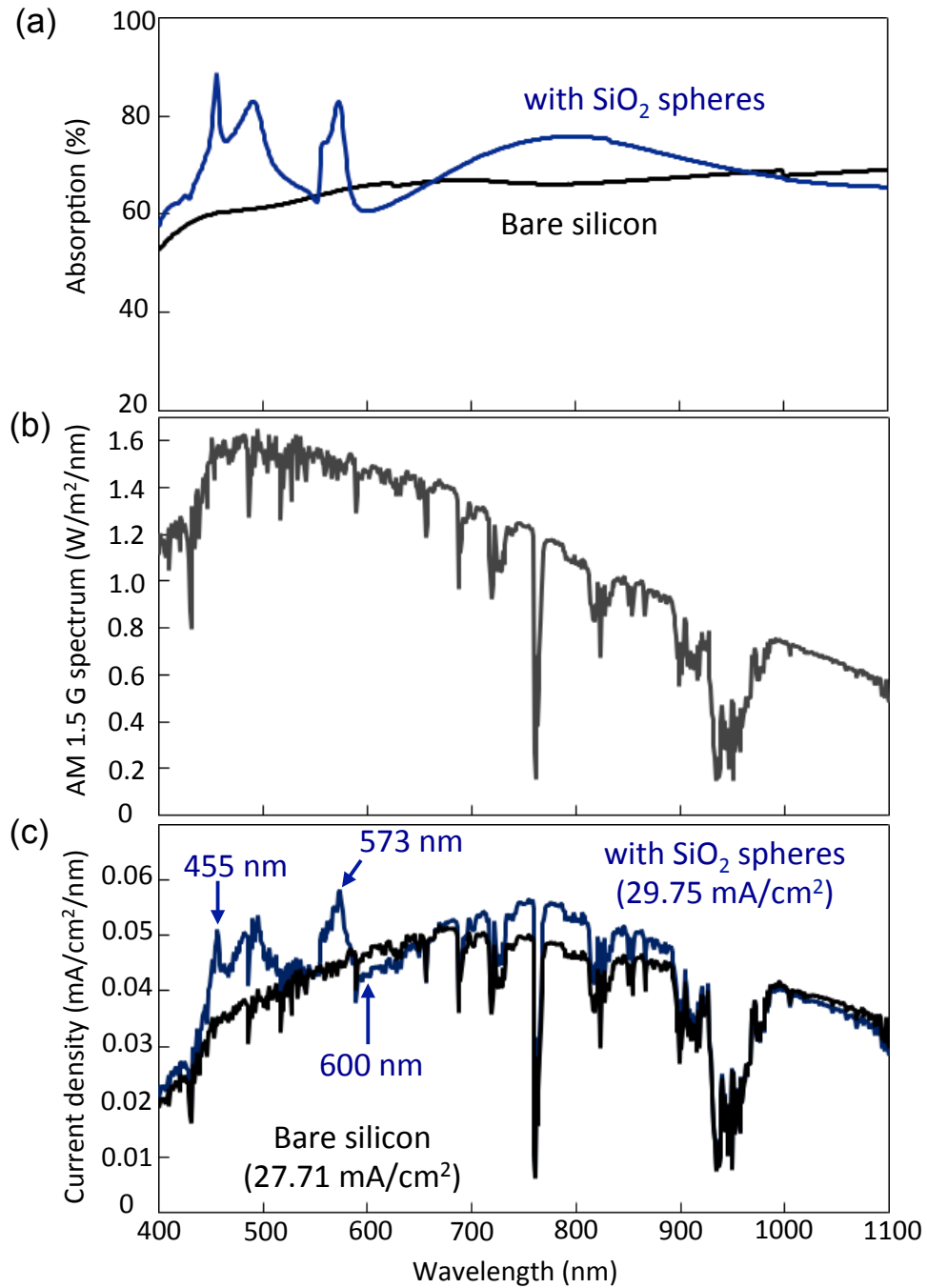


Figure 4.7: (a) Calculated absorption from two different structures: a bare Si cell (black) and a cell with close-packed SiO<sub>2</sub> nanospheres on top (blue). (b) AM 1.5 G solar spectrum for wavelengths of interest. (c) Calculated spectral current density obtained by weighting the solar spectrum by the calculated absorption. Enhancements in the spectral current density are observed at the wavelengths of 455 nm and 573 nm, and no enhancement is found at a wavelength of 600 nm.

## 4.5 Resonance tuning

Various applications require minimized reflection at particular wavelengths, which necessitate tuning the resonance of the nanostructures decorating the surface of the optoelectronic device in question. This tuning can be achieved by varying the spacing between the spheres (Fig. 4.8(a)) or by varying the diameter of the spheres (Fig. 4.8(b)). As expected, increasing either the diameter or spacing between the spheres leads to a red-shift of the resonances. Three particular resonances are emphasized in Fig. 4.8, corresponding to resonances 1, 2, and 4 from Fig. 4.4. The red-shift is more pronounced as the diameter of the sphere is increased compared to when an air-gap spacing layer is added to the lattice, because the electric field experiences a higher effective index of refraction, resulting in a larger effective periodicity for electromagnetic waves within the layer.

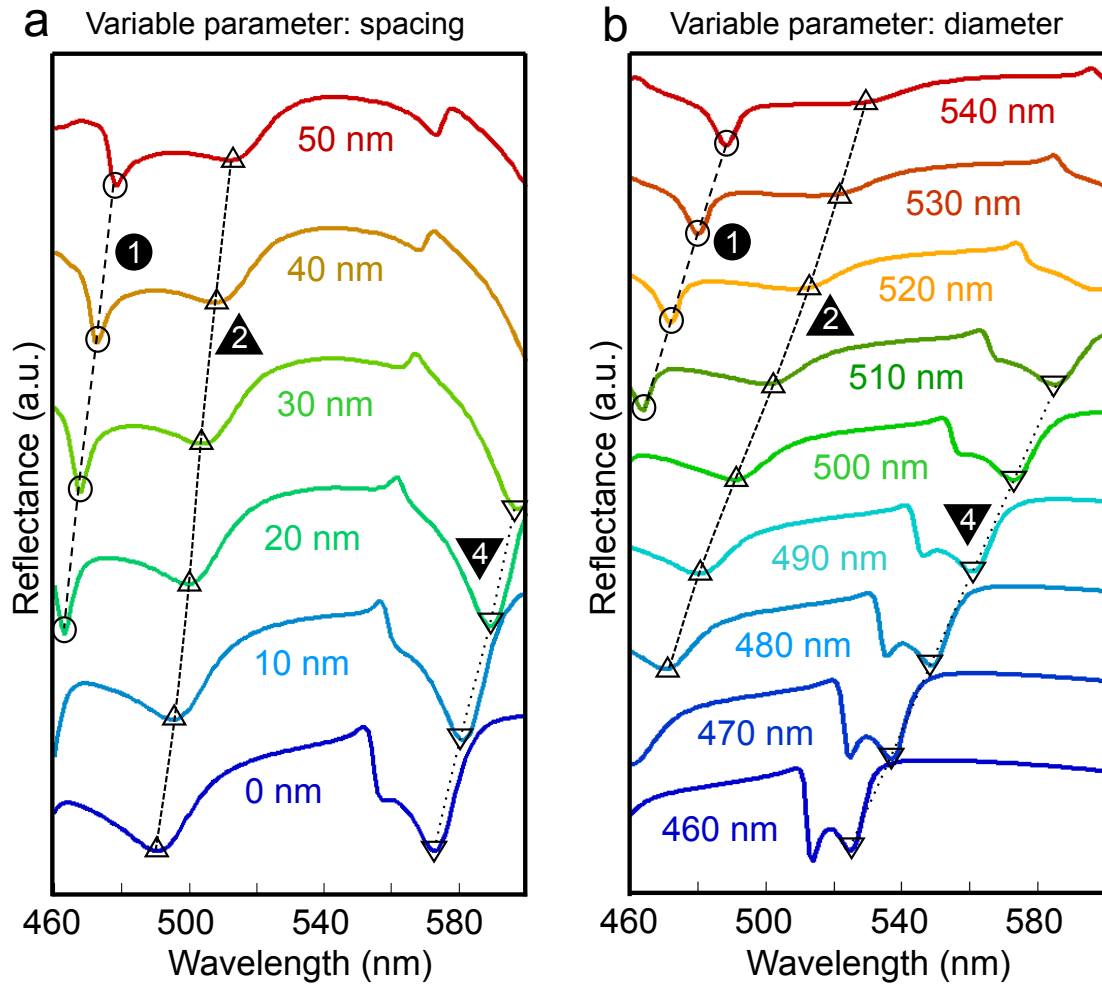


Figure 4.8: Reflectance as a function of wavelength for a monolayer of SiO<sub>2</sub> spheres on a Si substrate showing the reflectance variation due to (a) spacing between the 500 nm diameter spheres and (b) sphere diameter in a close-packed configuration. The three resonances (assigned as 1, 2, 4) correspond to the resonances that occur at normal incidence shown in Fig. 4.4. The dashed lines are guides to the eyes. All calculations are based on the FDTD method.

## 4.6 Microscale optical measurement

In order to investigate the optical resonances in more detail experimentally, we measure the reflectance on the microscale regime using an upright optical microscope (Fig. 4.9(a)). For this microscopic reflection measurement, a tungsten halogen white light source (BPS101, BWTEK Inc., Fig. 4.10) was connected to a confocal optical microscope via a multimode optical fiber. The reflection signal was recorded by a CCD camera (DV401-BV, WiTec). The reflection spectrum shown in Fig. 4.9 was the average of nine measurements for different regions of the sample with close-packed SiO<sub>2</sub> nanospheres, recorded with an integration time of 0.2 s per frame and an average over 100 frames. Regions containing only close-packed SiO<sub>2</sub> nanospheres are selected for this measurement. Three representative areas are shown in Fig. 4.9(a), where each hexagonal pattern shows illumination of seven close-packed SiO<sub>2</sub> nanospheres. For normally incident light at  $\lambda = 573$  nm, one would expect excitation of a whispering gallery mode and reduced reflection; however, Figure 4.9(a) instead shows a peak in the reflectance near this wavelength. This peak is caused by an angle averaging effect of the numerical aperture of the objective lens ( $NA = 0.75$ , corresponding to an acceptance angle of  $\sim 30^\circ$ ).

As shown in Fig. 4.4(d), as the incident angle of illumination is increased from  $0^\circ$  to  $30^\circ$ , the resonance that occurs at  $\lambda = 573$  nm is split (there is a red-shifted and a blue shifted branch). FDTD simulations show that the weighted average of the reflectance over this angular region agrees well with the experimental results obtained via microscopic reflectance measurements (Fig. 4.9(a)). For comparison,

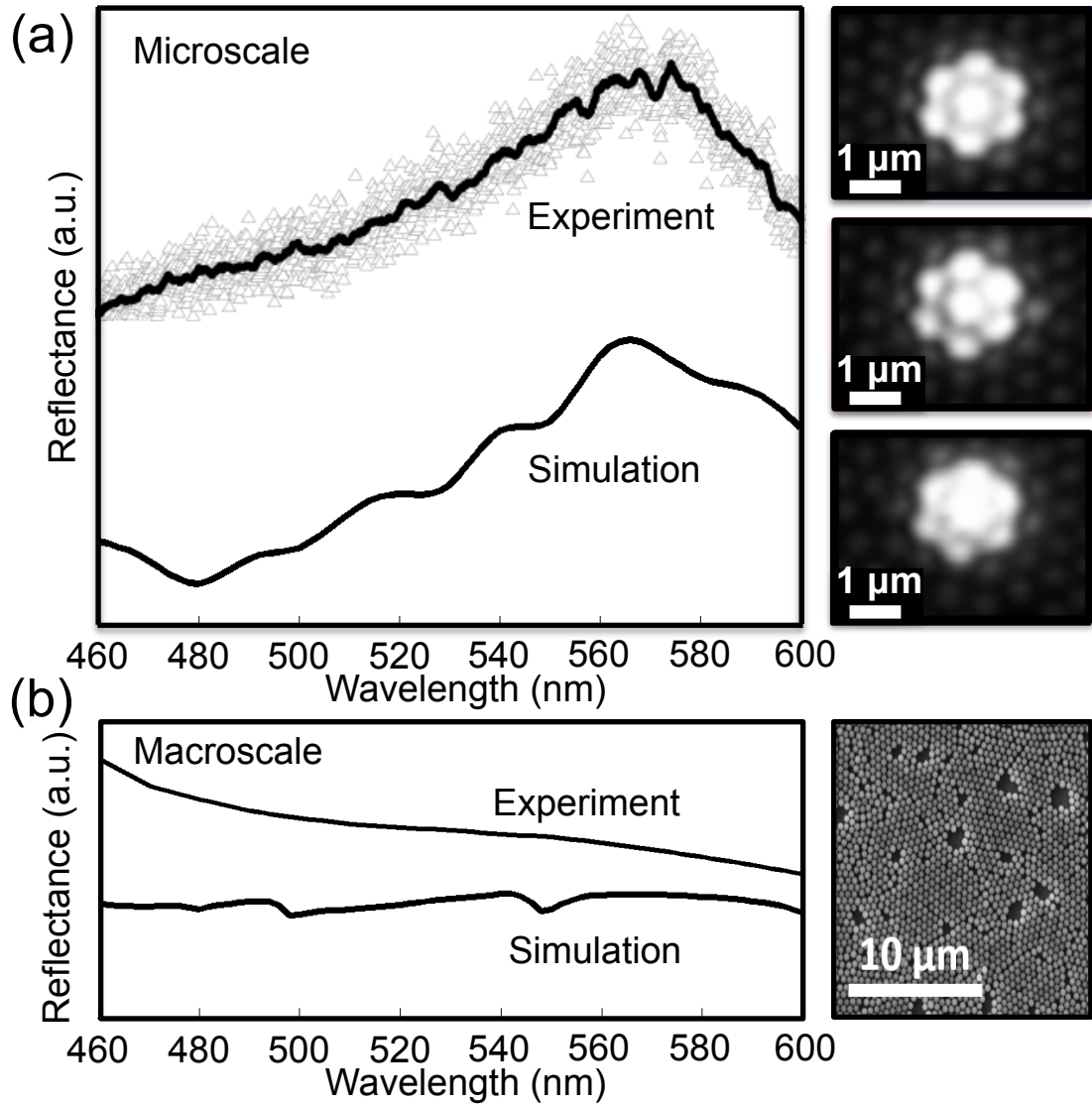


Figure 4.9: (a) Left: Microscopic reflectance measurements and simulations for a set of close-packed SiO<sub>2</sub> nanospheres. Right: representative optical images of three close-packed clusters under illumination. (b) Left: Macroscopic reflectance measurements and simulations corresponding to an angle of incidence of 10° with respect to the normal. Measurements were performed using an integrating sphere and calculations using the FDTD method. Right: SEM image showing SiO<sub>2</sub> nanospheres atop a Si wafer where the measurements were performed.

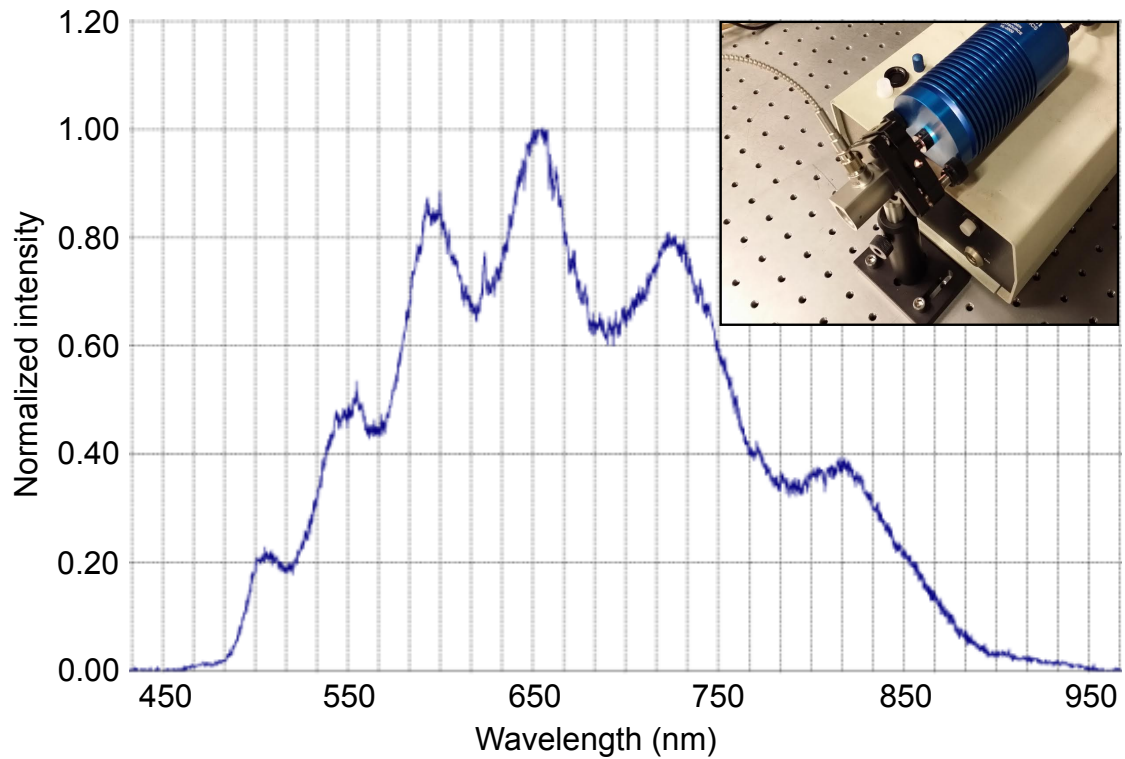


Figure 4.10: Measured spectrum of the tungsten halogen white light source (BPS101, BWTEK Inc.). Inset shows the light source coupled into the multimode optical fiber.

Figure 4.9(b) shows a macroscopic measurement of the reflectance obtained using an integrating sphere with a spot size of  $\sim 0.5 \text{ cm}^2$  at an incident angle of  $10^\circ$ . The relatively flat response is an effect of averaging over the resonances as a result of variation in sphere diameter, spacing, and periodicity/randomization, as seen in the SEM image (Fig. 4.9(b), right). Despite this averaging effect, simulations of the reflectance for a close-packed array of 500 nm diameter spheres illuminated at an incident angle of  $10^\circ$  describe the measurements well (Fig. 4.9(b), left).

A weighted-average of the reflectivity resulting from different sphere sizes based on SEM images results in a further flattening of the optical response (Fig. 4.11). The size variation of the deposited  $\text{SiO}_2$  nanospheres was determined via image analysis of a representative scanning electron microscope image (Fig. 4.11(a)). The mean diameter was 502 nm with a standard deviation of 75 nm (Fig. 4.11(b)). The distribution of sphere sizes was used to determine the total reflectance by taking an average of the reflectance values from simulations of each sphere diameter and weighting the result by the distribution function (Figs. 4.4(d) and 4.5(b)).

Variation in sphere size, spacing, and Si surface coverage results in an averaging effect for macroscopic measurements of the reflectance. While the experiments are performed over an area of  $\sim 0.5 \text{ cm}^2$ , optical simulations are limited to areas of  $\sim 1 \mu\text{m}^2$  and employ periodic (or Bloch) boundary conditions to enable largescale arrays. To simulate the effects of nanosphere size variation, we have performed simulations of the reflectance under normal incident illumination for spheres with diameters between 460 nm and 540 nm (Fig. 4.12, grey lines), corresponding to the size distribution obtained from SEM images of the samples (Fig. 4.11). Fig-

ure 4.12 also shows the weighted-average of simulations with different sphere sizes. Similarly, the nanosphere arrays do not always cover the complete surface of the Si wafer. To determine the effect of surface coverage, a second weighted-average of the reflectance data was taken with the simulated reflectance data obtained for a bare Si wafer. Two coverage percentages (67% and 100%) are shown in Fig. 4.12.

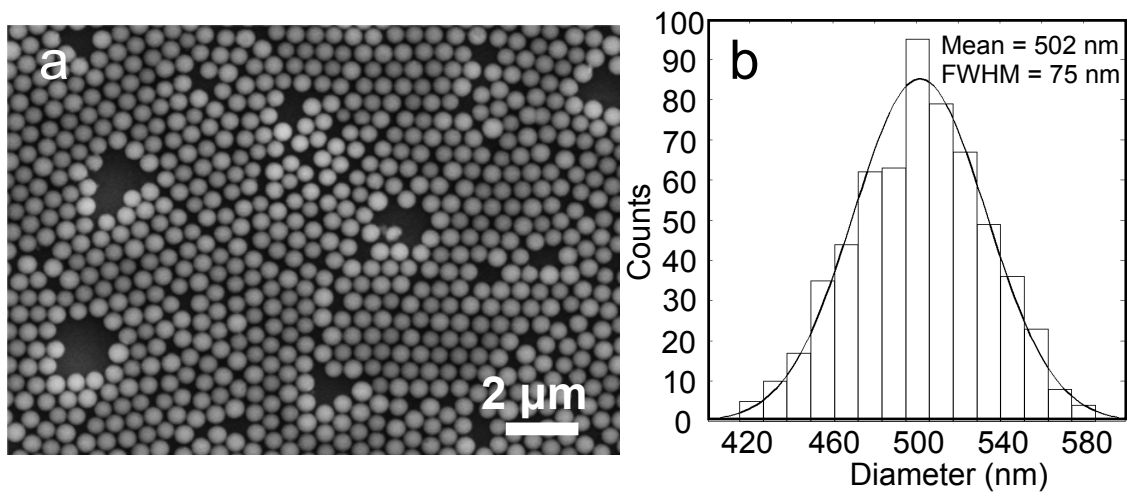


Figure 4.11: (a) SEM image used to determine (b) the diameter variation of SiO<sub>2</sub> nanospheres deposited atop the Si wafer used in the experiments.

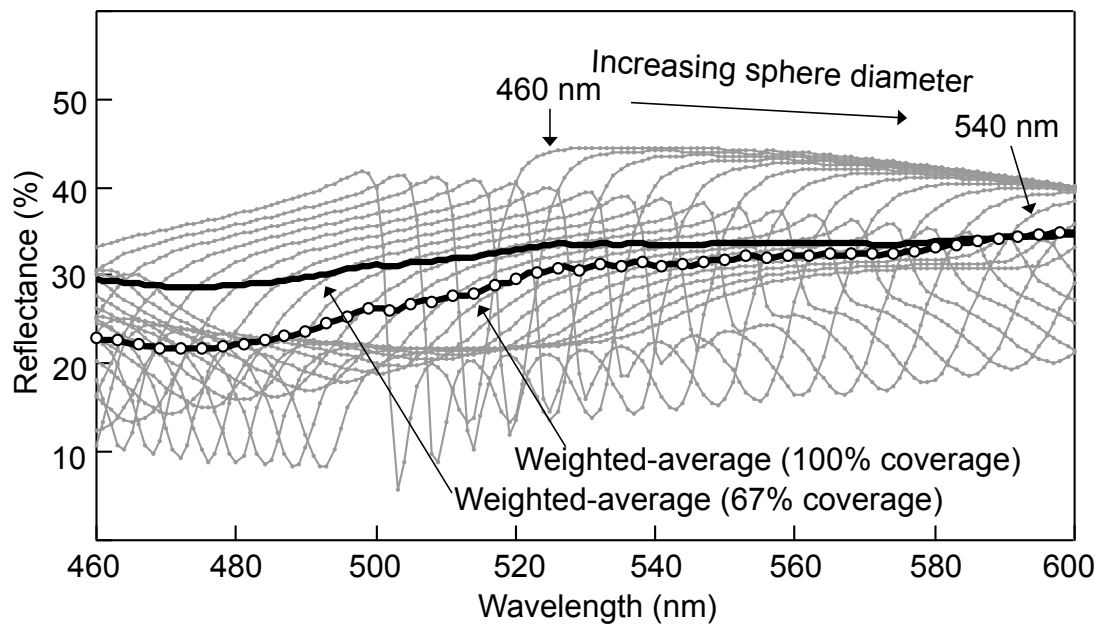


Figure 4.12: Simulated reflectance for each sphere diameter (grey solid lines) and the diameter weighted-average considering 67% and 100% area coverages (black solid line and circles, respectively).

## 4.7 Microscale electrical measurement

We perform local photocurrent measurements using a standard multi-crystalline Si solar cell with a thin-film silicon nitride ( $\text{Si}_3\text{N}_4$ ) antireflection layer with and without the addition of the nanosphere coating. A confocal optical microscope was used for the photo-response measurements, where a  $100\times$  objective lens was used as a local source of excitation (with  $\text{NA} = 0.75$ ). The illumination source originated from a supercontinuum laser that was fiber-coupled to the microscope to measure photo-generated current from the solar cell. To monitor the incident laser power, a Si photodetector is used. A small fraction of light directed to a photodetector for lock-in detection. Two lock-in amplifiers fed with one chopper are used simultaneously for this measurement to monitor both incident laser power and measured photo-current at the same time. This addresses the time dependent power variations of the light source. A piezo stage is used to scan different parts of the sample. A photograph and detailed schematic showing the measurement set-up are in Fig. 4.13 and Fig. 4.14, respectively. Because the tunable laser has a non-uniform power spectrum, all the measurements were normalized to the incident power for each wavelength. Thus, the measured wavelength-dependent photocurrent of the device containing the nanosphere coating is normalized to the photocurrent obtained for the device without the coating. Measurements are made on three different regions of the sample, as shown in Fig. 4.15. The average photocurrent enhancement obtained for three different regions with close-packed spheres is shown in Fig. 4.16(b). The measurement is compared with the calculated absorptivity enhancement based

on FDTD simulations (Fig. 4.16(a)). A peak in the calculated absorption and the measured photocurrent is found at  $\lambda = 455$  nm. This peak corresponds to a resonance similar to resonance 1 (Fig. 4.4(d)) for a  $\text{SiO}_2$  array directly atop Si, whereas for the device in Fig. 4.16 there is an additional  $\text{Si}_3\text{N}_4$  coating. This resonance persists even though the incident illumination contains a range of angles ( $0^\circ$  to  $30^\circ$ ). The measured and calculated enhancements are found to be in good agreement. Fig. 4.16(c) shows an SEM of the close-packed nanosphere coating, indicating areas where the measurements were performed.

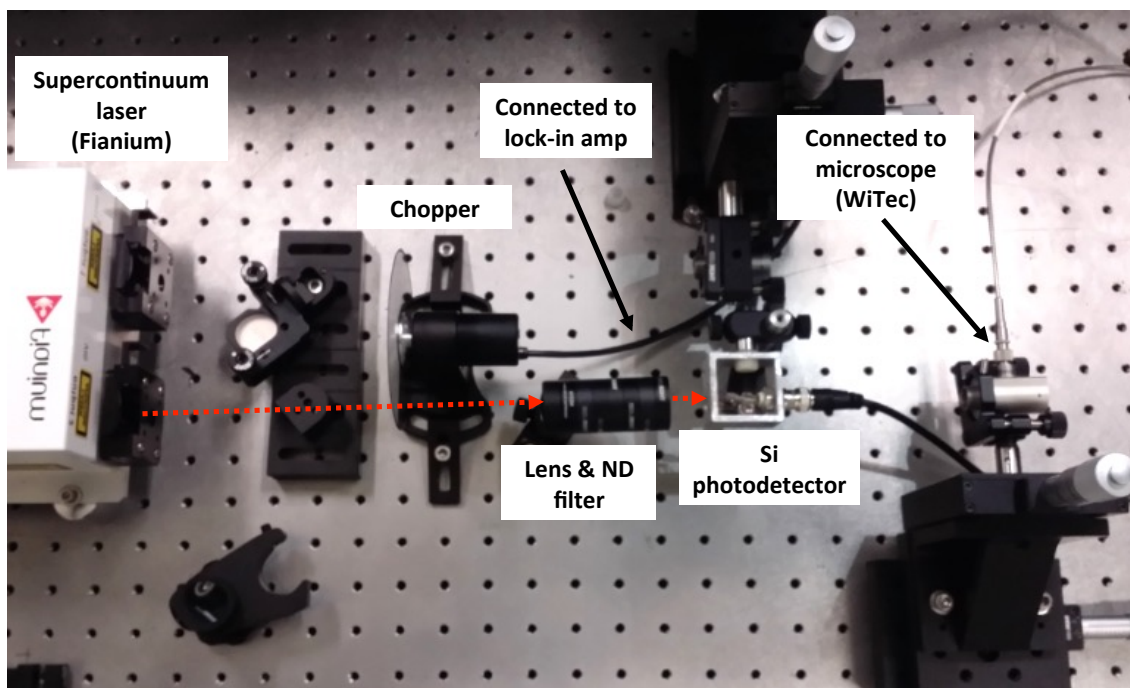


Figure 4.13: A photograph showing the optical path for the supercontinuum laser coupled into the microscope. Red dotted line shows the beam path.

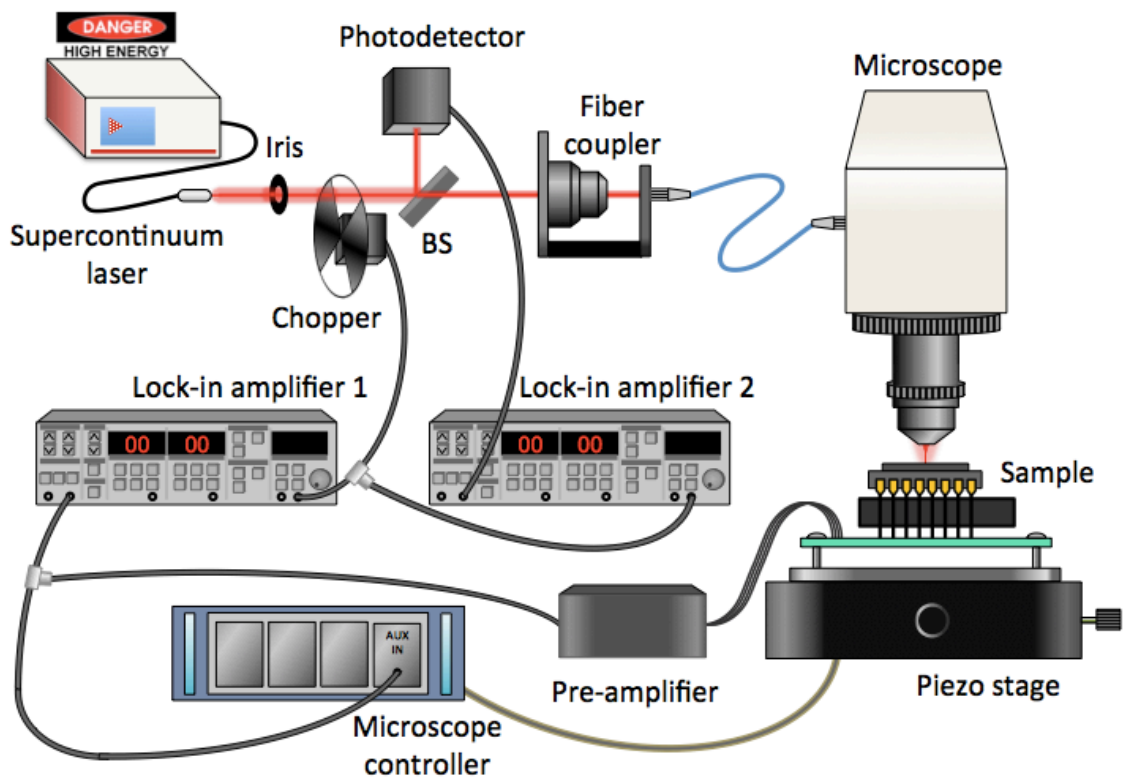


Figure 4.14: Schematic showing the microscale photocurrent measurement set-up.

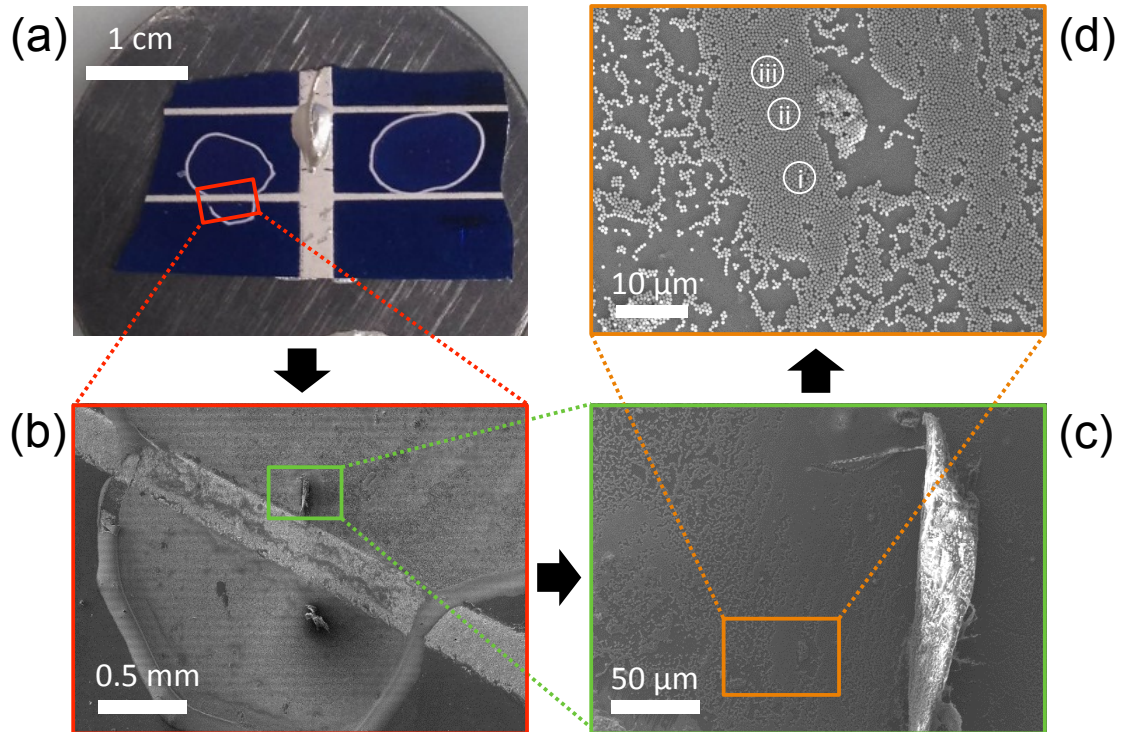


Figure 4.15: (a) Optical and (b)-(d) SEM images showing the Si solar cell used for photocurrent measurements. (d) Numbers on the image represent same spots as in Fig. 4.16 (c) where three measurements are conducted.

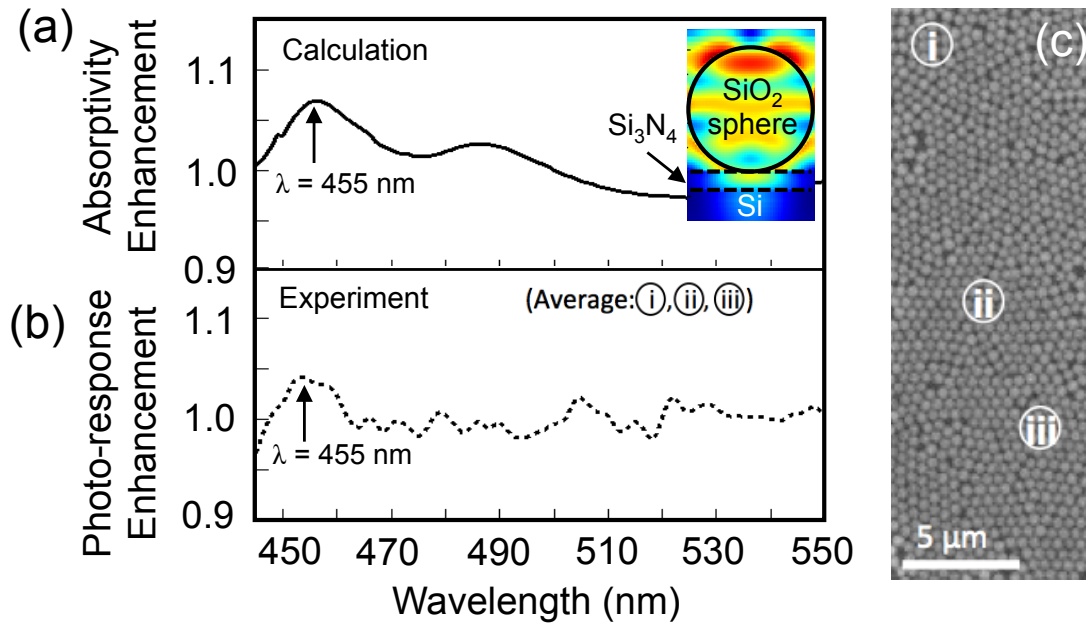


Figure 4.16: (a) Calculated absorptivity and (b) measured photo-response enhancement resulting from the addition of a close-packed SiO<sub>2</sub> nanosphere coating to a Si solar cell that already contains a Si<sub>3</sub>N<sub>4</sub> ARC. Inset shows the calculated electric field profile at  $\lambda = 455$  nm, which is similar to resonance 1 in Fig. 4.4. A photocurrent enhancement of  $\sim 5\%$  is measured. (c) SEM image showing three representative, close-packed regions where the measurements shown in (b) were performed.

## 4.8 Conclusions

In conclusion, we have developed SiO<sub>2</sub> dielectric nanosphere ARCs that improve the light absorptivity within a semiconducting slab and ultimately increase the power conversion efficiency of solar cells by exploiting various optical resonances. A combination of optical simulations and experimental measurements were performed and compared, which enable insights into the excited modes. Photo-response measurements for a Si solar cell were also presented, and the results illustrate how the excitation of individual modes can improve the optoelectronic properties of solar cells. Because SiO<sub>2</sub> nanospheres can be made with an easy, inexpensive and scalable process, this type of ARC is an excellent new candidate for replacing conventional ARC technologies that are unsuitable for certain photovoltaic technologies.

## Chapter 5: Conclusions and future outlook

In this thesis, I have described novel anti-reflection techniques based on two architectures: (i) a transparent cellulous-fiber coating and (ii) an array of coupled micro-resonators. Both techniques enable a significant reduction in the reflectivity of a device and are amiable to large-scale production. These techniques were experimentally applied to a variety of common solar cell materials (*e.g.*, GaAs and Si). The addition of a transparent paper coating to an uncoated GaAs solar cell lead to a 23.9% improvement in the power conversion efficiency. Similar enhancements can be obtained for flat Si solar cells; however, textured devices are hindered by small amounts of absorption that occur within the transparent paper. Coupled micro-resonators created by SiO<sub>2</sub> spheres are also shown to reduce reflective and have both broadband and narrowband resonances that can be tuned by modification of either the pitch or diameter of the spheres. Trade-offs exist between larger narrowband enhancements and smaller broadband enhancements.

## 5.1 Improving transparent paper coatings

The addition of a transparent cellulose-fiber coating to a typical solar cell made of GaAs or Si, reduces reflection from 35-40% to 15-20% over the entire spectral range. While this reduction in reflection leads to a significant power conversion efficiency enhancement, its performance does not surpass that of traditional thin-film anti-reflection coatings despite its advantages in terms of fabrication costs, flexibility, and environmental sustainability. However, given these advantages, we consider future opportunities to improve these paper coatings.

In order to reduce reflection further, one could use multiple papers to create a graded index coating. The index of refraction of the paper is based on the cellulose pulp material, density, and binder material. By changing these parameters, the index of refraction can be modified. An ideal broadband anti-reflection coating would consist of a material whose index of refraction is equal to that of air at the top (where the light enters the whole structure), is equal to that of the substrate on the bottom (where light enters the semiconductor), and is gradually varied from one side to the other. In principle, this behavior could be achieved by stacking multiple layers of papers with different refractive indices.

To improve paper coatings on textured surfaces, one needs to reduce absorption within the paper layer. We showed that the absorption within the paper layer is very small (Fig. 2.2); however, even spurious absorption of a few percent can be important for very high quality solar cells. To reduce absorption further, it would be useful to explore papers made from different plant pulps.

In addition to improved optical performance, future transparent paper coatings will need to be robust enough to be deployed for long periods of times (*e.g.*, decades). While our initial stability tests show that these coatings can withstand significant exposure to solar illumination, further in-depth studies are needed. Most solar panels are rated for 20-30 years of operation (however, many last much longer), and the paper should be made to withstand similar timeframes.

## 5.2 Improving dielectric micro-resonator coatings

To improve micro-resonator coatings, a balance is needed between weak broadband absorption enhancements and strong narrowband enhancements. One way to increase the number of resonances is by using multiple spheres with either different diameters or that are made of different materials (with different refractive indices). Our preliminary studies suggest that the introduction of different materials into the periodic array (*e.g.*,  $\text{Si}_3\text{N}_4$ ,  $\text{TiO}_2$ , etc.) can yield additional resonances and improved reflection suppression.

## Appendix A: **Additional information on experiments and calculations**

### A.1 Polarization of optical setup

While ideally the light entering the integrating sphere from the monochromator is unpolarized, we determined that there was a slight wavelength-dependent polarization due to the optics of our setup. The polarization of the light incident on the integrating sphere was measured (Fig. 2.8) and used to correct our simulation data, which is calculated separately for each polarization. The relationship between incident and reflected light at the sample for each polarization is

$$I_{r,S} = I_{i,S} \cdot R_S \tag{A.1}$$

and

$$I_{r,P} = I_{i,P} \cdot R_P \tag{A.2}$$

where  $R_S$  is the reflectivity, and  $I_{r,S}$  and  $I_{i,S}$  are the intensity of reflected and incident light, respectively, for the incident  $S$ -polarized light. Similarly,  $I_{r,P}$ ,  $I_{i,P}$ , and  $R_P$  correspond to the values for the incident  $P$ -polarized light.

The ratio of the light intensities from the two different polarizations is:

$$\gamma = \frac{I_{i,P}}{I_{i,S}}. \quad (\text{A.3})$$

The average reflectivity incorporating both polarizations is

$$R = \frac{I_{r,S} + I_{r,P}}{I_{i,S} + I_{i,P}} = \frac{I_{i,S} \cdot R_S + I_{i,P} \cdot R_P}{I_{i,S} + I_{i,P}} = \frac{I_{i,S} \cdot R_S + \gamma \cdot I_{i,S} \cdot R_P}{I_{i,S} + \gamma \cdot I_{i,S}} = \frac{R_S + \gamma \cdot R_P}{1 + \gamma}. \quad (\text{A.4})$$

If we have same fraction of each polarization ( $\gamma = 1$ ), the reflectivity is

$$R = \frac{R_S + R_P}{2}. \quad (\text{A.5})$$

A schematic illustration and a photograph (LPNIRE100-B, Thorlabs) showing polarizers we have used to determine system polarization are in Fig. A.1. For shorter wavelengths, we use a polarizer that has an operational range of 400-700 nm (LPVISE100-A, Thorlabs). The dot denotes the direction of the E-field polarization (see Fig A.1). For longer wavelengths, we use a polarizer having an operational range of 600-1100 nm (LPNIRE100-B, Thorlabs). Note: for this polarizer, the dot denotes the direction where the electric field is filtered out, resulting in a polarization of the E-field that is 90 degrees with respect to the dot (see Fig A.1). Both polarizers are 1 in in diameter and have a thickness of 3.5 mm.

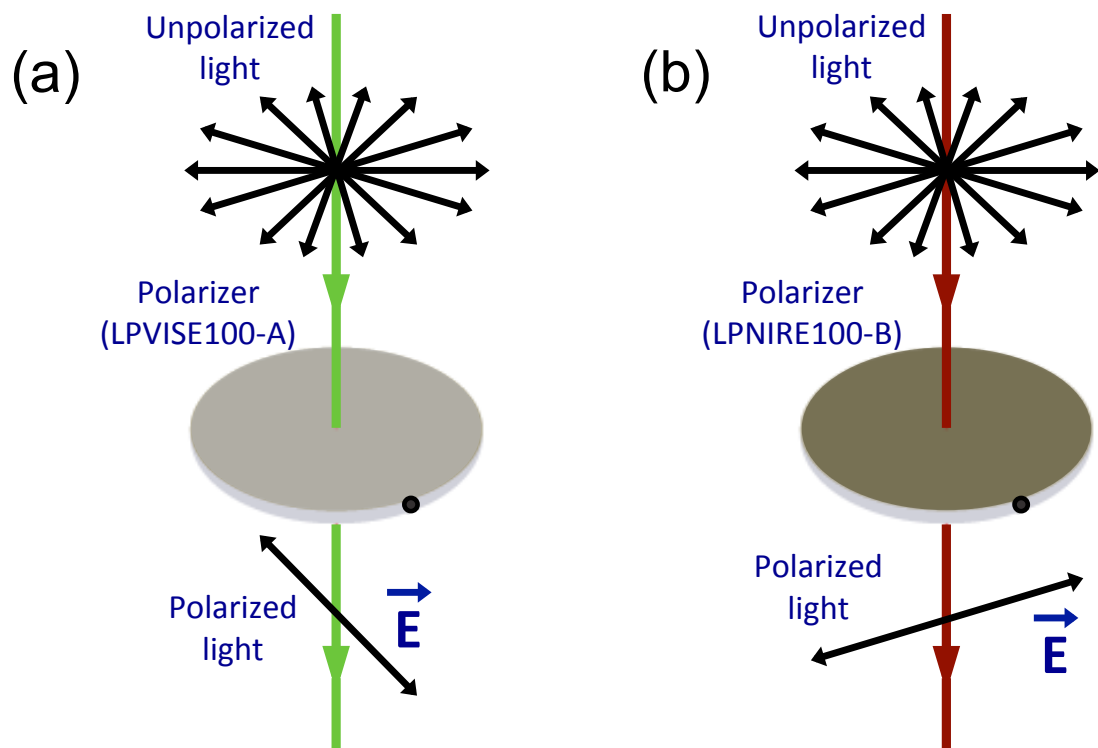


Figure A.1: Schematic of the polarizers used in the optical setup. (a) Model LPVISE100-A polarizes the light along the direction of the black dot for short wavelengths (400-700 nm). (b) Model LPNIRE100-B polarizes the light perpendicular to the direction of the black dot, which is used for longer wavelength measurements (600-1100 nm). Note: we found that the black dot denoting polarization direction can vary from product to product from the manufacture, so it is best to measure the polarization direction independently.

## A.2 Incoherent reflection model

An incoherent optical model is used to determine the total reflection from the paper ARC.

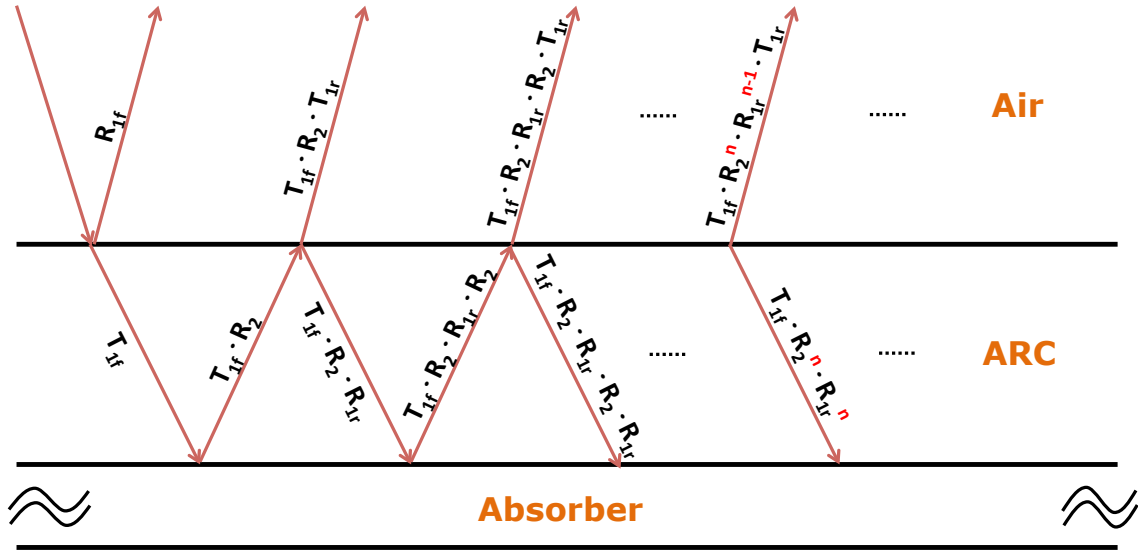


Figure A.2: Schematic depicting multiple reflections resulting in a geometric series.

At each interface, the reflectivity is calculated as

$$R_{total} = \frac{R_S + R_P}{2} \quad (\text{A.6})$$

where

$$R_S = \left| \frac{n_1 \cos \theta_i - n_2 \cos \theta_t}{n_1 \cos \theta_i + n_2 \cos \theta_t} \right|^2 \quad (\text{A.7})$$

and

$$R_P = \left| \frac{n_1 \cos \theta_t - n_2 \cos \theta_i}{n_1 \cos \theta_t + n_2 \cos \theta_i} \right|^2 \quad (\text{A.8})$$

and  $n_1$  and  $n_2$  are the refractive indices of the two media at the interface and  $\theta_i$  and  $\theta_t$  are the incident and transmitted angles from the surface normal. Because we are dealing with a film, some of the transmitted light will be reflected once it hits the next interface. This light will make its way back to the surface and a fraction of that light will exit the structure, hence adding to the original reflection signal. This process is shown in Fig. A.2.

The total reflectivity is then:

$$\begin{aligned} R &= R_{1f} + T_{1f} \cdot R_2 \cdot T_{1r} + T_{1f} \cdot R_2 \cdot R_{1r} \cdot R_2 \cdot T_{1r} + \dots + T_{1f} \cdot R_2^n \cdot R_{1r}^{n-1} \cdot T_{1r} + \dots \\ &= R_{1f} + \frac{T_{1f} \cdot R_2 \cdot T_{1r}}{1 - R_2 \cdot R_{1r}} \end{aligned} \quad (\text{A.9})$$

based upon the transmission,  $T$ , and reflection,  $R$ , shown in Fig. A.2.

## Appendix B: **Fabrication details**

### B.1 Deposition of SiO<sub>2</sub> nanospheres using a Meyer rod

A monolayer of SiO<sub>2</sub> nanospheres was deposited on Si by using the Meyer rod rolling technique, with a 0.46 mm (0.018 in) wire wound rod (No. 18 wire wound rod, RD specialties, Inc.). A surfactant (Zonyl) was added to the SiO<sub>2</sub> nanospheres suspension to prevent sphere agglomeration, resulting in a suspension with sphere concentration of  $\sim 0.1\%$ . The coated sample was subjected to a mild annealing treatment, at 50 °C for 1 min, on a hotplate to evaporate the water.

## B.2 A Si photodetector

A simple Si photodetector is fabricated and used to determine the effect of a nanosphere array on an optoelectronic device. The device has two metal contacts having different work functions deposited on a Si wafer. As a result of the differing work functions, the band structure is asymmetric from one contact to the other. With this type of structure, we can collect photo-generated carriers under light illumination without any external bias. Because it is not a  $p$ - $n$  junction-based device, the efficiency is not high but can be used as a proof-of-concept. Thus, we use this device to test the characteristics of our new anti-reflection coatings before applying it to solar cells.

The mask (Fig. B.1 and B.2) is designed with a CAD software (AutoCad) and the photomask (CAD/Art Services, Inc., [www.outpucity.com](http://www.outpucity.com)) is made based on the drawing. Figure B.3. to Figure B.7 show the fabrication procedures.

Photoresist (PR) is covered with a spin coater at 3000 rpm for 1 min. The mask is aligned using a mask aligner and UV exposed for 7 s (see Fig. B.3). Exposed PR is then removed with developer for 45 s. Metal 1 (Ag) is deposited using a thermal evaporator and is in direct contact with the Si where the PR was removed. The target thickness is 270 nm. Figure B.4. shows metal 1 deposited on the Si wafer. The sample is immersed in PR remover for 40 min, and only the metal in contact with Si remains. Any additional residue is then removed with acetone (see Fig. B.5).

The electron beam evaporator (Denton) is used for metal 2 deposition (Pt).

The target thickness is 20 nm. Figure B.6. shows the deposition of metal 2 on a Si wafer. Afterwards, the thin layer of Pt is covered with an additional metal layer having a thickness of 100 nm (Cr or Ag) to guarantee small contact resistance and robust operation. Figure B.7. shows a schematic of device structure including additionally deposited metal layers on metal 2 (Pt). Figure A.8 shows the fabricated device (and holder) used for photo-current measurement with and without SiO<sub>2</sub> nanospheres on surface. Table B.1 summarizes the fabrication steps.

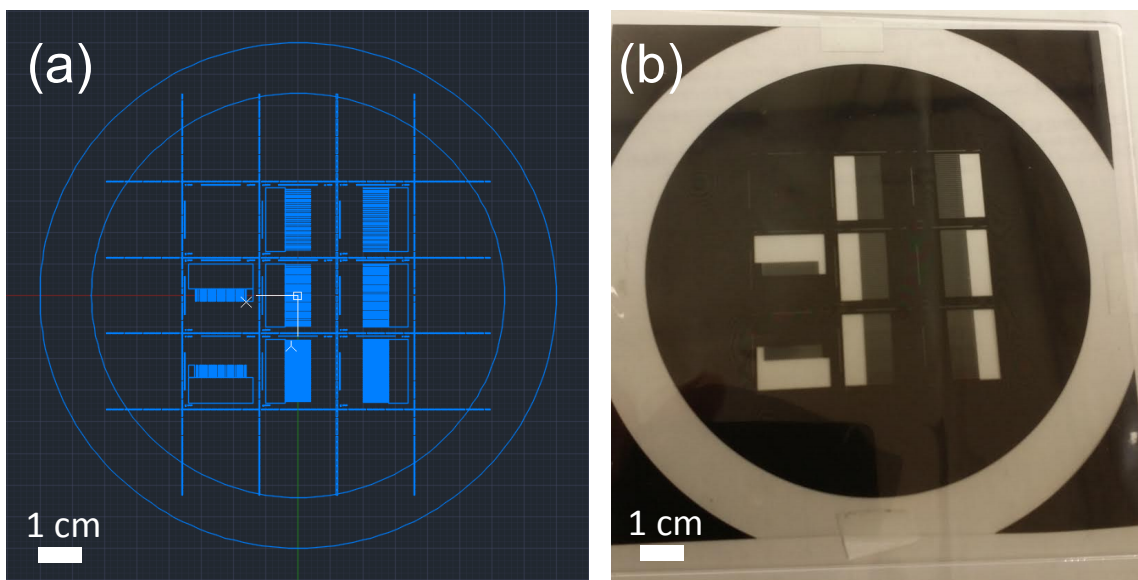


Figure B.1: (a) Designed layout of the photomask (AutoCad). (b) Fabricated mask attached to quartz.

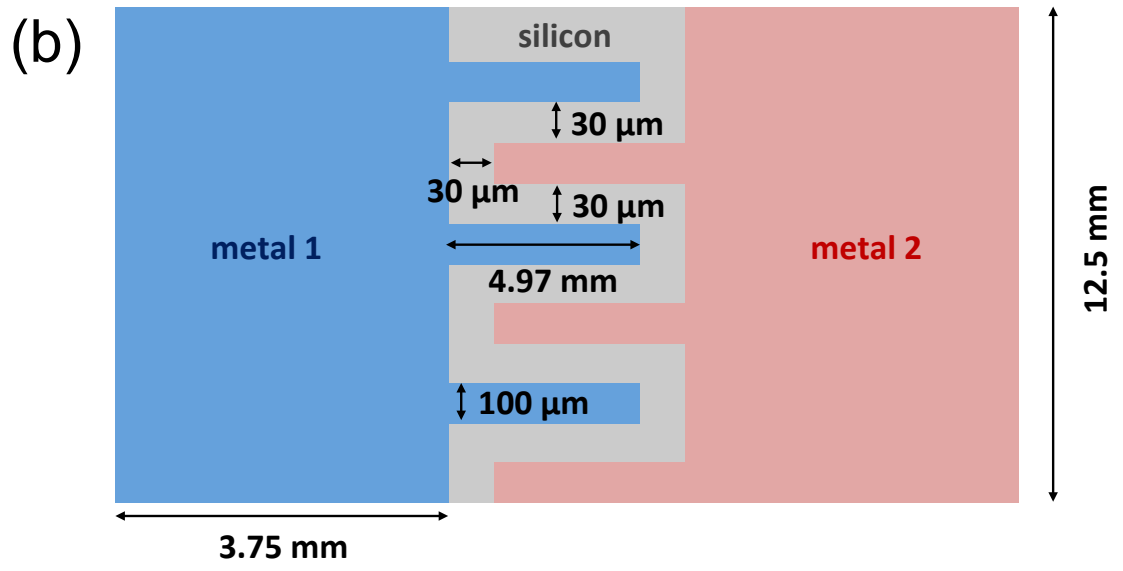
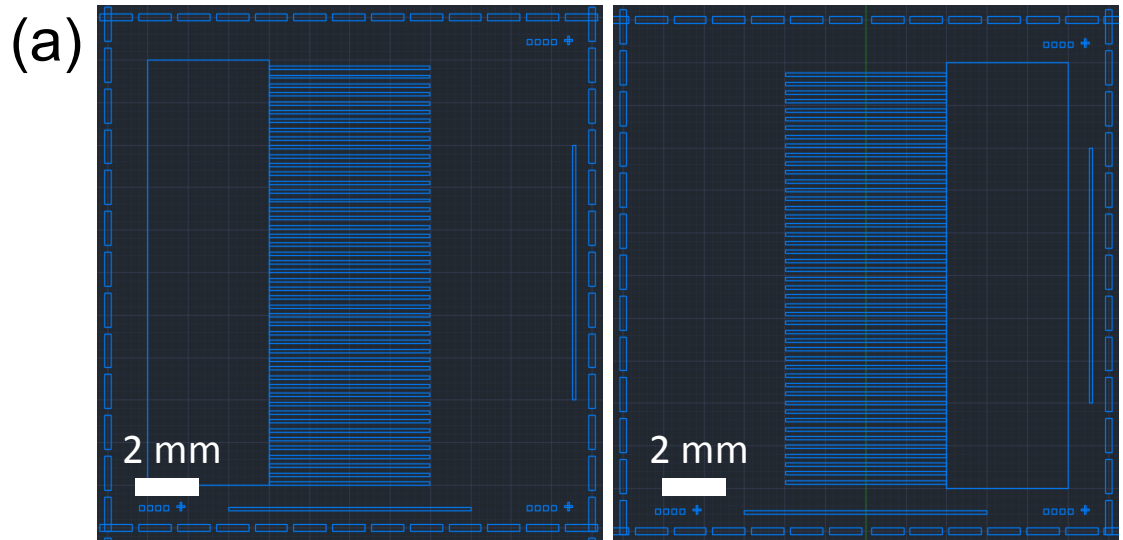


Figure B.2: (a) Designed mask layout showing metal regions to be defined. (b) Schematic of a typical device having a distance of  $30\ \mu\text{m}$  separating the two metals. Other devices having a separations of  $50\ \mu\text{m}$  and  $100\ \mu\text{m}$  are also made to determine the effect of carrier diffusion length on device performance.

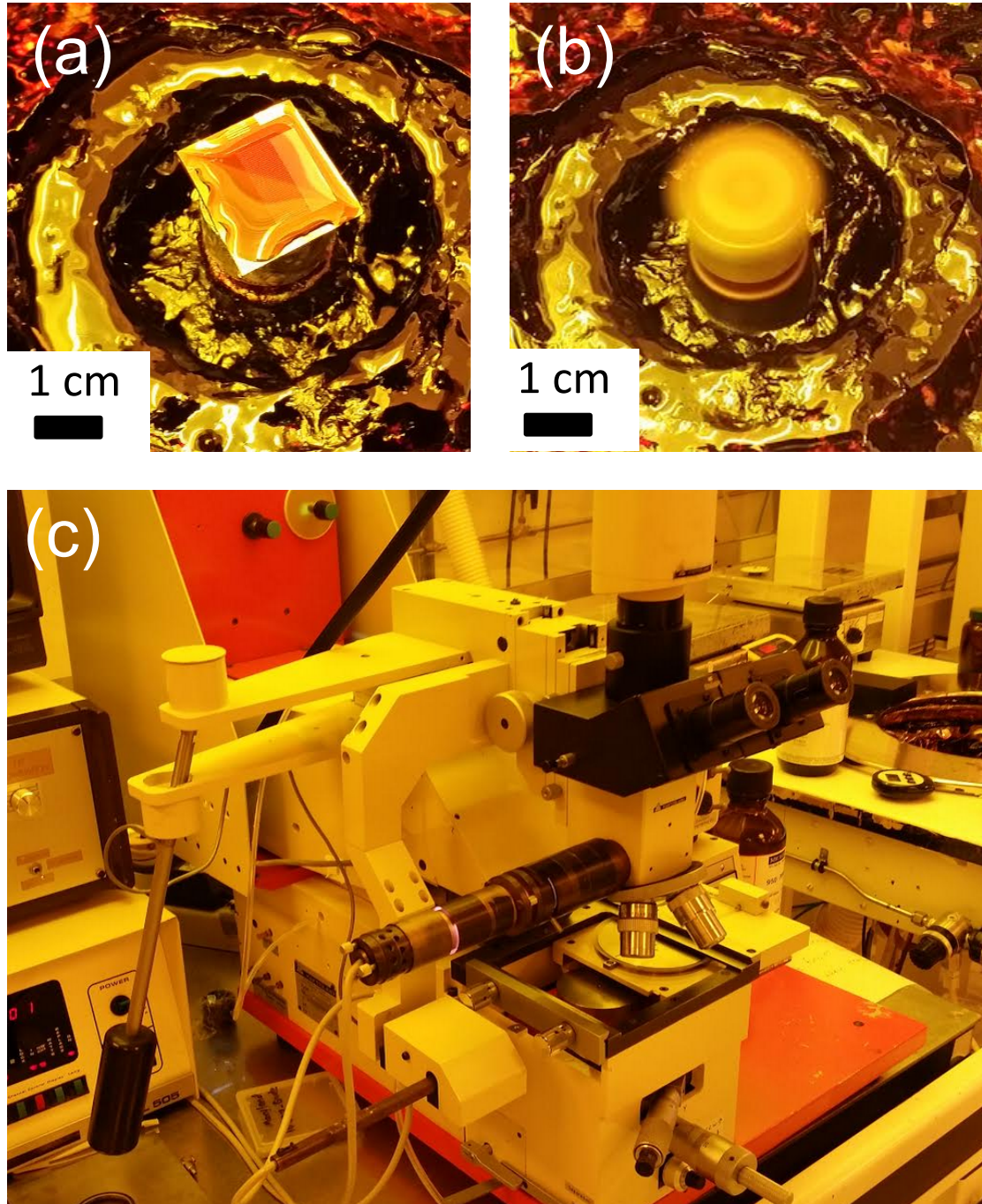


Figure B.3: Photolithograph. (a) A sample coated with photoresist (PR) prior to spin coating. (b) Spin coating of PR at 3000 rpm for 1 min. (c) A photograph of the mask aligner used for this work. The sample is exposed under UV illumination for 7 s and PR is removed by immersing in developer (Micro Dev 1:1) for 45 s.

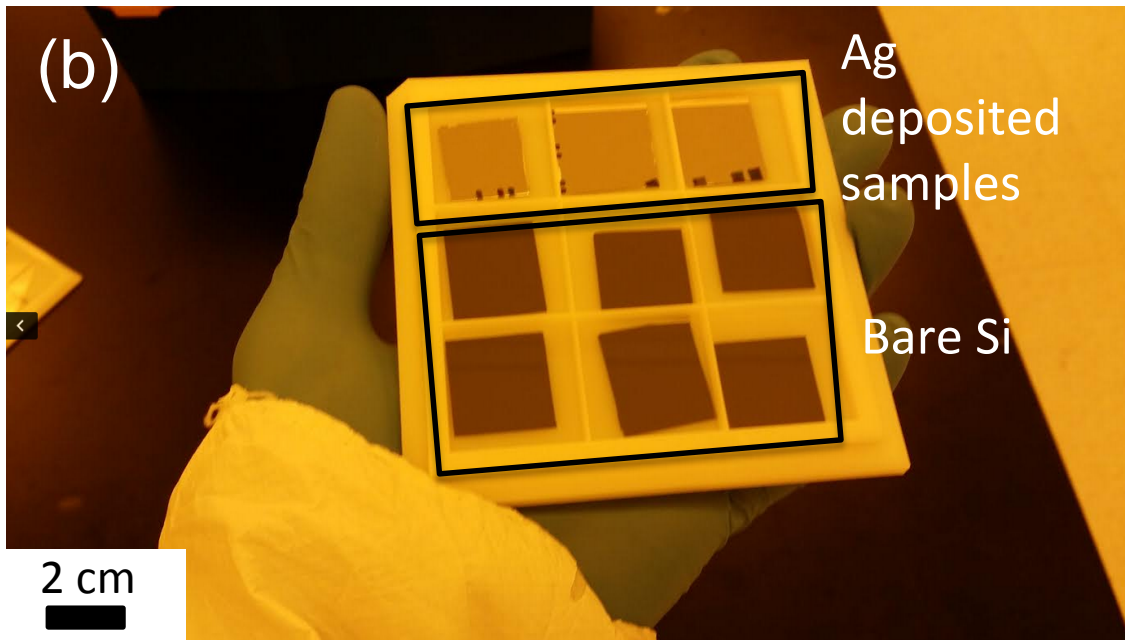
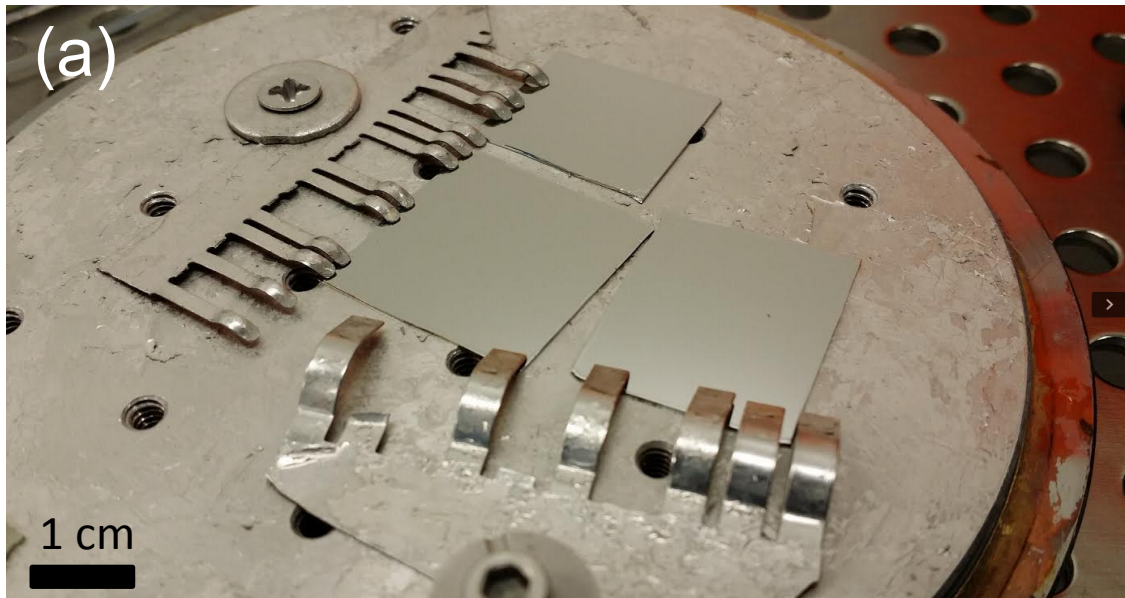


Figure B.4: Metal deposition. (a) Metal 1 (Ag) is deposited with a thermal evaporator. (b) Photograph showing Ag deposited samples and bare Si. There is a clear color contrast due to the deposited Ag having a thickness of 270 nm.

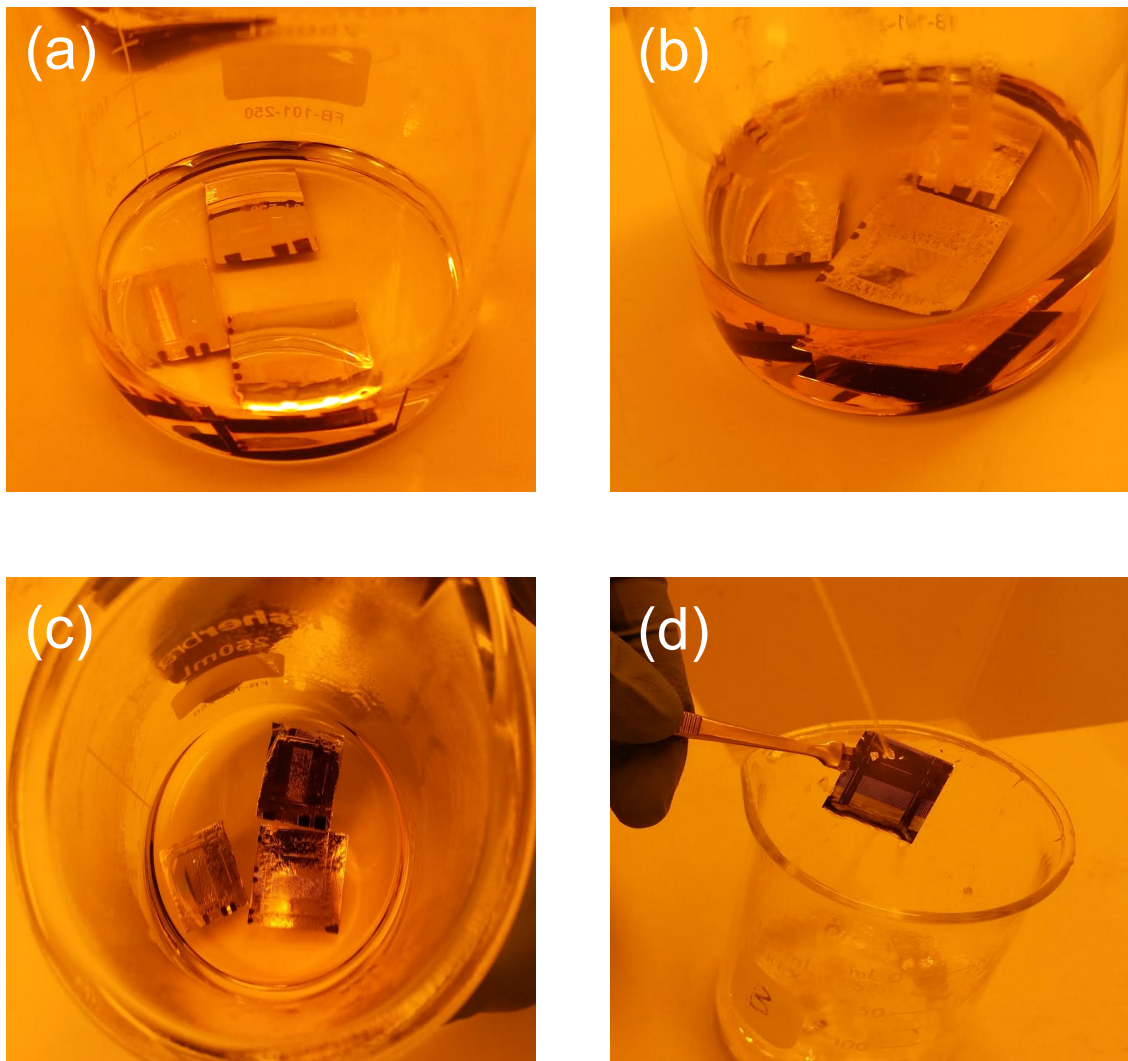


Figure B.5: Ag removal. (a)-(c) Pictures showing the procedure of PR removal after Ag deposition. The sample is immersed in PR remover (Remover PG) for 40 min. (d) Further residue can be removed with Acetone cleaning.

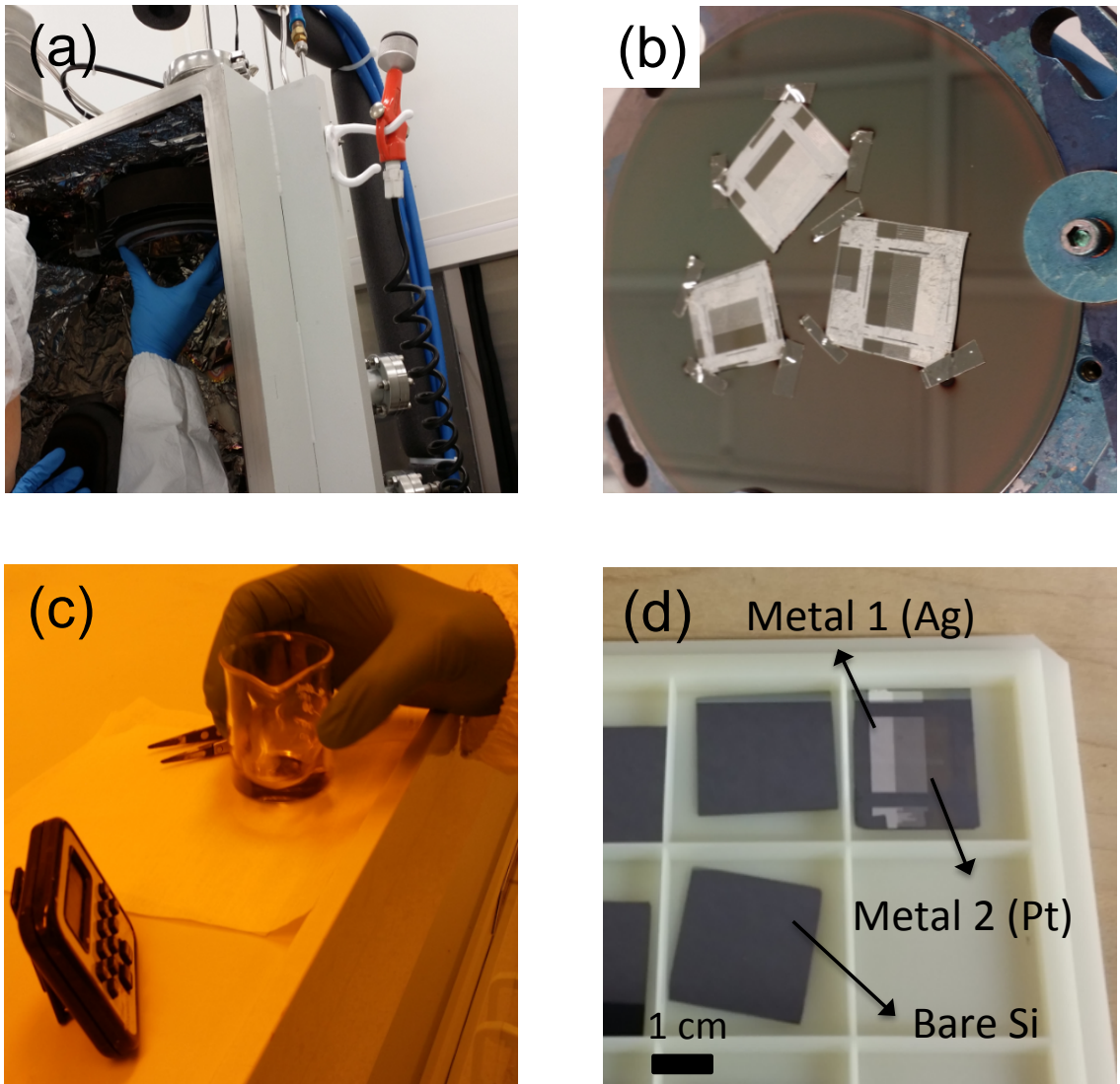


Figure B.6: Final metallization. (a) Samples are loaded into the electron beam evaporator (Denton) for metal 2 (Pt) deposition. (b) Picture showing Pt deposited onto the samples. The thickness is 20 nm. The deposited Pt is covered with other metals (Ag, Cr) having a thickness of 100 nm afterwards to guarantee small contact resistance. (c) Photoresist is removed after Pt deposition. (d) Picture showing the sample having two deposited metals on the Si substrate.

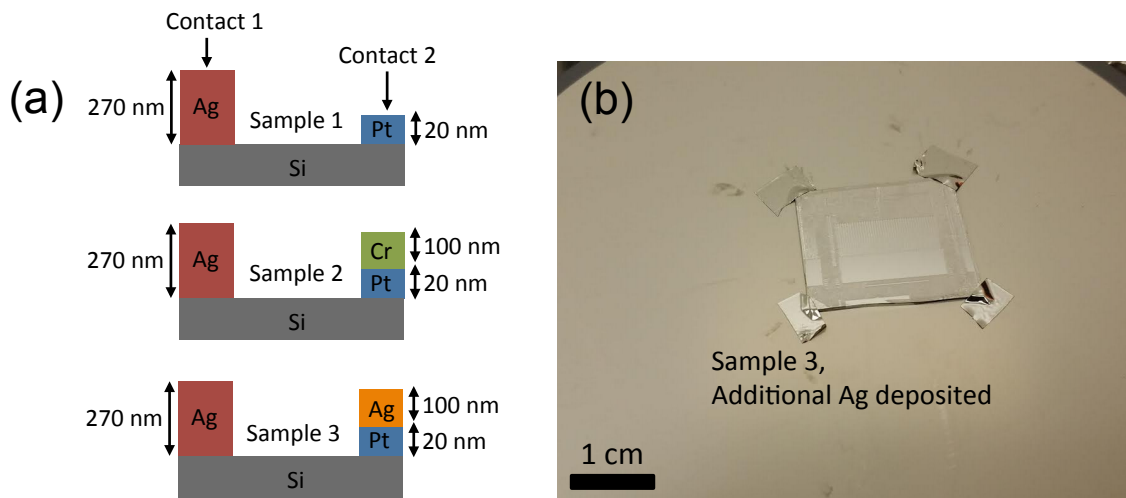
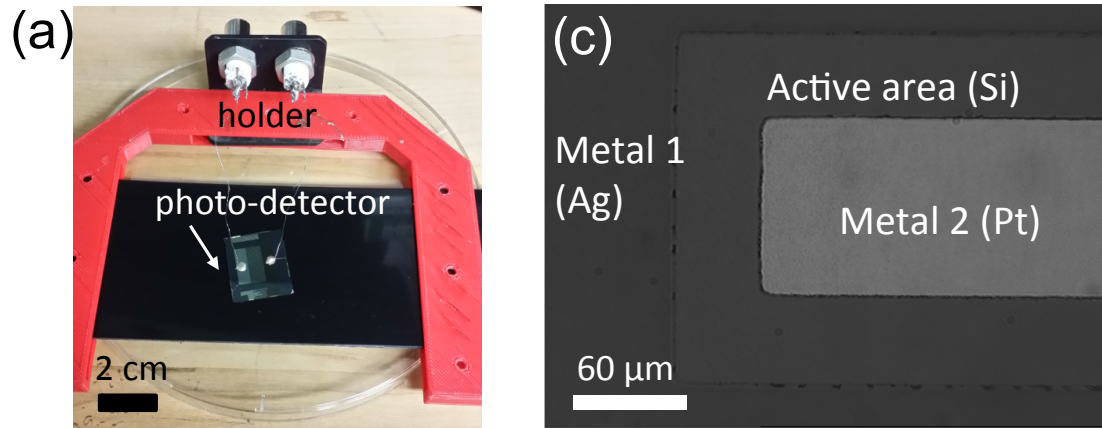


Figure B.7: To guarantee small contact resistance on contact 2, additional metal layers (Cr, Ag) are deposited on top of Pt. (a) Schematics showing three different types of samples for contact 2; Pt only (Sample 1), Pt with additional Cr on top (Sample 2), and Pt with additional Ag on top (Sample 3). Regardless of the existence of additional metal layers, the band structure of three samples are similar. (b) A picture showing additionally deposited Ag on Pt. The thickness is targeted to 100 nm.

### Si photodetector w/o spheres



### Si photodetector w/ spheres

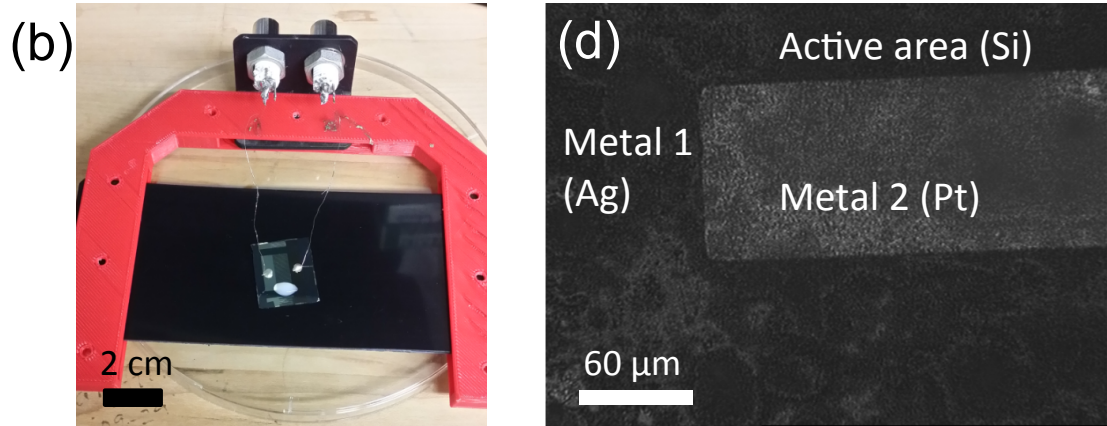


Figure B.8: (a),(b) Optical and (c),(d) SEM images showing Si photodetector used for photocurrent measurement (a),(c) without SiO<sub>2</sub> nanospheres (b),(d) with SiO<sub>2</sub> nanospheres.

Table B.1: Si photodetector fabrication steps.

Step	Description	Equipment	Conditions	Remarks
1	Cleaning	Hood		
2	Ozone cleaning	UV Ozone cleaner	~ 1 hour	Surface up
3	PR coating	Spinner	3000 rpm for 1 min	Use positive PR (1813)
4	Soft bake	Hot plate	100°C for 1 min	Left oven (UMD FabLab)
5	Align mask	MJB-3 Mask aligner	UV exposure for 7 sec	Glass printed down
6	Develop	Hood	Developing for 45 sec	Micro DEV 1:1, in developer there should be no H <sub>2</sub> O
7	Pattern checking	Optical microscope		
8	Metal 1 deposition	Thermal / E-beam evaporator	Depends on situation,	
9	PR removing	Hood and hot plate	~ 1 hour to day, using hot plate	Remover PG
10	Repeat from step 3 for the 2 <sup>nd</sup> round			

## Bibliography

- [1] D. Ha, Z. Fang, L. Hu, and J. N. Munday, "Paper-based anti-reflection coatings for photovoltaics," *Advanced Energy Materials*, **4**, 1301804 (2014).
- [2] D. Ha, J. Murray, Z. Fang, L. Hu, and J. N. Munday, "Advanced broadband antireflection coatings based on cellulose microfiber paper," *IEEE Journal of Photovoltaics*, **5**, 577-583 (2015).
- [3] D. Ha, C. Gong, M. S. Leite, and J. N. Munday, "Demonstration of resonance coupling in scalable dielectric micro-resonator coatings for photovoltaics," (*submitted and under review*).
- [4] R. Gelman, *Renewable Energy Data Book*, (edited by M. Kubik, produced by the U.S. Department of Energy, 2009).
- [5] M. M. Hand, S. Baldwin, E. DeMeo, J. M. Reilly, T. Mai, D. Arent, G. Porro, M. Meshek, and D. Sandor, *Renewable Electricity Futures Study (Entire Report)*, (National Renewable Energy Laboratory, 2012).
- [6] V. E. Ferry, J. N. Munday, and H. A. Atwater, "Design considerations for plasmonic photovoltaics," *Advanced Materials*, **22**, 4794-4808 (2010).
- [7] H. R. Stuart and D. G. Hall, "Island size effects in nanoparticle-enhanced photodetectors," *Applied Physics Letters*, **73**, 3815-3817 (1998).
- [8] J. N. Munday and H. A. Atwater, "Large integrated absorption enhancement in plasmonic solar cells by combining metallic gratings and antireflection coatings," *Nano Letters*, **11**, 2195-2201 (2010).
- [9] H. A. Atwater and A. Polman, "Plasmonics for improved photovoltaic devices," *Nature Materials*, **9**, 205-213 (2010).

- [10] K. R. Catchpole and A. Polman, “Design principles for particle plasmon enhanced solar cells,” *Applied Physics Letters*, **93**, 19113 (2008).
- [11] K. R. Catchpole and A. Polman, “Plasmonic solar cells,” *Optics Express*, **16**, 21793-21800, (2008).
- [12] Q. Gan, F. J. Bartoli, and Z. H. Kafafi, “Plasmonic-enhanced organic photovoltaics: Breaking the 10% efficiency barrier,” *Advanced Materials*, **25**, 2385-2396 (2013).
- [13] I. -K. Ding, J. Zhu, W. Cai, S. -J. Moon, N. Cai, P. Wang, S. M. Zakeeruddin, M. Grätzel, M. L. Brongersma, Y. Cui, and M. D. McGehee, “Plasmonic dye-sensitized solar cells,” *Advanced Energy Materials*, **1**, 52-57 (2011).
- [14] J. Bhattacharya, N. Chakravarty, S. Pattnaik, W. Dennis Slafer, R. Biswas, and V. L. Dalal, “A photonic-plasmonic structure for enhancing light absorption in thin film solar cells,” *Applied Physics Letters*, **99**, 13114 (2011).
- [15] R. A. Pala, J. White, E. Barnard, J. Liu, and M. L. Brongersma, “Design of plasmonic thin-film solar cells with broadband absorption enhancements,” *Advanced Materials*, **21**, 3504-3509 (2009).
- [16] C. Hägglund, M. Zäch, G. Petersson, and B. Kasemo, “Electromagnetic coupling of light into a silicon solar cell by nanodisk plasmons,” *Applied Physics Letters*, **92**, 053110 (2008).
- [17] J. Grandidier, D. M. Callahan, J. N. Munday, and H. A. Atwater, “Thin-film solar cells: Light absorption enhancement in thin-film solar cells using whispering gallery modes in dielectric nanospheres,” *Advanced Materials*, **23**, 1272-1276 (2011).
- [18] J. Grandidier, D. M. Callahan, J. N. Munday, and H. A. Atwater, “Gallium arsenide solar cell absorption enhancement using whispering gallery modes of dielectric nanospheres,” *IEEE Journal of Photovoltaics*, **2**, 123-128 (2012).
- [19] J. Grandidier, R. A. Weitekamp, M. G. Deceglie, D. M. Callahan, C. Battaglia, C. R. Bukowsky, C. Ballif, R. H. Grubbs, and H. A. Atwater, “Solar cell efficiency enhancement via light trapping in printable resonant dielectric nanosphere arrays,” *Physica Status Solidi (a)*, **210**, 255-260 (2013).
- [20] D. Derkacs, W. V. Chen, P. M. Matheu, S. H. Lim, P. K. L. Yu, and E. T. Yu, “Nanoparticle-induced light scattering for improved performance of quantum-well solar cells,” *Applied Physics Letters*, **93**, 091107 (2008).

- [21] J. Zhu, C. -M. Hsu, Z. Yu, S. Fan, and Y. Cui, “Nanodome solar cells with efficient light management and self-cleaning,” *Nano Letters*, **10**, 1979-1984 (2010).
- [22] M. Kroll, S. Fahr, C. Helgert, C. Rockstuhl, F. Lederer, and T. Pertsch, “Employing dielectric diffractive structures in solar cells - A numerical study,” *Physica Status Solidi (a)*, **205**, 2777-2795 (2008).
- [23] P. Spinelli, M. A. Verschuuren, and A. Polman, “Broadband omnidirectional antireflection coating based on subwavelength surface Mie resonators,” *Nature Communications*, **3**, 692 (2012).
- [24] M. L. Brongersma, Y. Cui, and S. Fan, “Light management for photovoltaics using high-index nanostructures,” *Nature Materials*, **13**, 451-560 (2014).
- [25] J. Yin, Y. Zang, C. Yue, X. He, Jing Li, Z. Wu, and Y. Fang, “Self- assembled hollow nanosphere arrays used as low Q whispering gallery mode resonators on thin film solar cells for light trapping,” *Physical Chemistry Chemical Physics*, **15**, 16874-16882 (2013).
- [26] M. Mariano, F. J. Rodríguez, P. Romero-Gomez, G. Kozyreff, and J. Martorell, “Light coupling into the whispering gallery modes of a fiber array thin film solar cell for fixed partial Sun tracking,” *Scientific Reports*, **4**, 4959 (2014).
- [27] Y. Yao, J. Yao, V. K. Narasimhan, Z. Ruan, C. Xie, S. Fan, and Y. Cui, “Broadband light management using low-Q whispering gallery modes in spherical nanoshells,” *Nature Communications*, **3**, 664 (2012).
- [28] P. Bermel, C. Luo, L. Zeng, L. C. Kimerling, J. D. Joannopoulos, “Improving thin-film crystalline silicon solar cell efficiencies with photonic crystals,” *Optics Express*, **15**, 16986 (2007).
- [29] A. Luque and S. Hegedus, *Handbook of Photovoltaic Science and Engineering*, (John Wiley and Sons, United Kingdom, 2011).
- [30] H. Park, D. Shin, G. Kang, S. Baek, K. Kim, and W. J. Padilla, “Broadband optical antireflection enhancement by integrating antireflective nanoislands with silicon nanoconical-frustum arrays,” *Advanced Materials*, **23**, 5796-5800 (2011).
- [31] Z. Tang, A. Elfving, J. Bergqvist, W. Tress, and O. Inganäs, “Light trapping with dielectric scatterers in single- and tandem-junction organic solar cells,” *Advanced Energy Materials*, **3**, 1606-1613 (2013).
- [32] B. Niesen, B. P. Rand, P. V. Dorpe, D. Cheyns, L. Tong, A. Dmitriev, and P. Heremans, “Plasmonic efficiency enhancement of high performance organic

- solar cells with a nanostructured rear electrode,” *Advanced Energy Materials*, **3**, 145-150 (2013).
- [33] J. You, X. Li, F.-x. Xie, W. E. I. Sha, J. H. W. Kwong, G. Li, W. C. H. Choy, and Y. Yang, “Surface plasmon and scattering-enhanced low-bandgap polymer solar cell by a metal grating back electrode,” *Advanced Energy Materials* **2**, 1203-1207 (2012).
- [34] X. Li, W. C. H. Choy, L. Huo, F. Xie, W. E. I. Sha, B. Ding, X. Guo, Y. Li, J. Hou, J. You, and Y. Yang, “Dual plasmonic nanostructures for high performance inverted organic solar cells,” *Advanced Materials*, **24**, 3046-3052 (2012).
- [35] J. Weickert, R. B. Dunbar, H. C. Hesse, W. Wiedemann, and L. Schmidt-Mende, “Nanostructured organic and hybrid solar cells,” *Advanced Materials*, **23**, 1810 (2011).
- [36] K. J. Yu, L. Gao, J. S. Park, Y. R. Lee, C. J. Corcoran, R. G. Nuzzo, D. Chanda, and J. A. Rogers, “Light trapping in ultrathin monocrystalline silicon solar cells,” *Advanced Energy Materials*, **3**, 1401-1406 (2013).
- [37] D. M. O’Carroll, C. E. Hofmann, H. A. Atwater, “Conjugated polymer/metal nanowire heterostructure plasmonic antennas,” *Advanced Materials*, **22**, 1223-1227 (2010).
- [38] C. F. Bohren, D. R. Huffman, *Absorption and Scattering of Light by Small Particles*, (John Wiley Sons, New York, 1983).
- [39] L. Cao, P. Fan, A. P. Vasudev, J. S. White, Z. Yu, W. Cai, J. A. Schuller, S. Fan, and M. L. Brongersma, *Nano Letters*, **10**, 439-445 (2010).
- [40] Y. Zhou, C. Fuentes-Hernandez, T. M. Khan, J. -C. Liu, J. Hsu, J. W. Shim, A. Dindar, J. P. Youngblood, R. J. Moon, and B. Kippelen, “Recyclable organic solar cells on cellulose nanocrystal substrates,” *Scientific Reports*, **3**, 1536 (2013).
- [41] F. Wang, Z. Chen, L. Xiao, B. Qu, and Q. Gong, “Papery solar cells based on dielectric/metal hybrid transparent cathode,” *Solar Energy Materials and Solar Cells*, **94**, 1270-1274 (2010).
- [42] T. -S. Kim, S. -I. Na, S. -S. Kim, B. -K. Yu, J. -S. Yeo, and D. -Y. Kim, “Solution-processible polymer solar cells fabricated on a papery substrate,” *Physica Status Solidi (RRL)*, **6**, 13-15 (2012).

- [43] A. Hübler, B. Trnovec, T. Zillger, M. Ali, N. Wetzold, M. Mingeback, A. Wagenpfahl, C. Deibel, V. Dyakonov, "Printed Paper Photovoltaic Cells," *Advanced Energy Materials*, **1**, 1018-1022 (2011).
- [44] H. Zhu, Z. Xiao, D. Liu, Y. Li, N. J. Weadock, Z. Fang, J. Huang, and L. Hu, "Biodegradable transparent substrates for flexible organic-light-emitting diodes," *Energy and Environmental Science* **6**, 2105-2111 (2013).
- [45] H. Zhu, Z. Fang, C. Preston, Y. Li, and L. Hu, "Transparent paper: fabrications, properties, and device applications," *Energy and Environmental Science*, **7**, 269-287 (2013).
- [46] J. Vartiainen, T. Pöhler, K. Sirol, L. Pylkkänen, H. Alenius, J. Hokkinen, U. Tapper, P. Lahtinen, A. Kapanen, K. Putkisto, P. Hiekkataipale, P. Eronen, J. Ruokolainen, and A. Laukkanen, "Health and environmental safety aspects of friction grinding and spray drying of microfibrillated cellulose," *Cellulose*, **18**, 775-786 (2011).
- [47] N. Lin, J. Huang, and A. Dufresne, "Preparation, properties and applications of polysaccharide nanocrystals in advanced functional nanomaterials: a review," *Nanoscale* **4**, 3274-3294 (2012).
- [48] N. Lavoine, I. Desloges, A. Dufresne, and J. Bras, "Microfibrillated cellulose - Its barrier properties and applications in cellulosic materials A review," *Carbohydrate Polymers* **90**, 735-764 (2012).
- [49] Y. Habibi, L. A. Lucia, and O. J. Rojas, "Cellulose nanocrystals: chemistry, self-assembly, and applications," *Chemical Reviews*, **110**, 3479-3500 (2010).
- [50] R. J. Moon, A. Martini, J. Nairn, J. Simonsen, and J. Youngblood, "Cellulose nanomaterials review: structure, properties and nanocomposites," *Chemical Society Reviews*, **40**, 3941-3994 (2011).
- [51] D. Klemm, F. Kramer, S. Moritz, T. Lindström, M. Ankerfors, D. Gray, and A. Dorris, "Nanocelluloses: a new family of nature-based materials," *Angewandte Chemie International Edition*, **50**, 5438-5466 (2011).
- [52] L. Hu, G. Zheng, J. Yao, N. Liu, B. Weil, M. Eskilsson, E. Karabulut, Z. Ruan, S. Fan, J. T. Bloking, M. D. McGehee, L. Wgberg, Y. Cui, "Transparent and conductive paper from nanocellulose fibers," *Energy and Environmental Science*, **6**, 513-518 (2013).
- [53] I. Siró, D. Plackett, "Microfibrillated cellulose and new nanocomposite materials: a review," *Cellulose*, **17**, 459-494 (2010).

- [54] H. Zhu, S. Parvinian, C. Preston, O. Vaaland, Z. Ruan, and L. Hu, "Transparent nanopaper with tailored optical properties," *Nanoscale*, **5**, 3787-3792 (2013).
- [55] C. -M. Hsu, S. T. Connor, M. X. Tang, and Y. Cui, "Wafer-scale silicon nanopillars and nanocones by Langmuir-Blodgett assembly and etching," *Applied Physics Letter*, **93**, 133109 (2008).
- [56] P. Jiang, J. F. Bertone, K. S. Hwang, and V. L. Colvin. "Single-crystal colloidal multilayers of controlled thickness," *Chemistry of Materials*, **11**, 2132-2140 (1999).
- [57] A. Mihi, C. Zhang, and P. V. Braun, "Transfer of preformed three-dimensional photonic crystals onto dye-sensitized solar cells," *Angewandte Chemie International Edition*, **50**, 5712-5715 (2011).
- [58] J. Wang, M. Liang, Y. Fang, T. Qiu, J. Zhang, and L. Zhi, "Rod-coating: Towards large-area fabrication of uniform reduced graphene oxide films for flexible touch screens," *Advanced Materials*, **24**, 2874-2878 (2012).
- [59] L. Hu, H. S. Kim, J. -Y. Lee, P. Peumans, and Y. Cui, "Scalable coating and properties of transparent, flexible, silver nanowire electrodes," *ACS Nano*, **4**, 2955-2963 (2010).
- [60] B. Dan, G. C. Irvin, and M. Pasquali, "Continuous and scalable fabrication of transparent conducting carbon nanotube films," *ACS Nano*, **3**, 835-843 (2009).
- [61] Z. Fang, H. Zhu, Y. Yuan, D. Ha, S. Zhu, C. Preston, Q. Chen, Y. Li, X. Han, S. Lee, G. Chen, T. Li, J. Munday, J. Huang, and L. Hu, "Novel nanostructured paper with ultrahigh transparency and ultrahigh haze for solar cells," *Nano Letters*, **14**, 765-773 (2014).
- [62] S. N. Kasarova, N. G. Sultanova, C. D. Ivanov, and I. D. Nikolov, "Analysis of the dispersion of optical plastic materials," *Optical Materials*, **29**, 1481-1490 (2007).
- [63] S. Hayashi, K. Asada, S. Horiike, H. Furuhashi, and T. Hirai, "Piezochromism of porous Poly(vinyl alcohol)-Poly(vinyl acetate) composite film in organic solvents," *Journal of Colloid and Interface Science*, **176**, 370-377 (1995).
- [64] E. D. Palik, *Handbook of optical constants of solids*, (Academic Press, New York, 1998).

- [65] C. C. Katsidis and D. I. Siapkas, “General transfer-matrix method for optical multilayer systems with coherent, partially coherent, and incoherent interference,” *Applied Optics*, **41**, 3978-3987 (2002).
- [66] *CompleteEASE, Ver. 4.72 (Computer Program)*, (J.A.Woollam Co. Inc., Lincoln, NE, USA, 2012).
- [67] R. M. Cole, Y. Sugawara, J. J. Baumberg, S. Mahajan, M. Abdelsalam, and P. N. Bartlett, “Easily coupled whispering gallery plasmons in dielectric nanospheres embedded in gold films,” *Physical Review Letters*, **97**, 137401 (2006).
- [68] K. Hayata, H. Yénaka, and M. Koshiha, “Theory of coherent optical coupling between dielectric microspheres,” *Optics Letters*, **18**, 1385-1387 (1993).
- [69] X. Yu, L. Shi, D. Han, J. Zi, and P. V. Braun, “High quality factor metallo-dielectric hybrid plasmonic-photonic crystals,” *Advanced Functional Materials*, **20**, 1910-1916 (2010).
- [70] A. Yariv, Y. Xu, R. K. Lee, and A. Scherer, “Coupled-resonator optical waveguide: a proposal and analysis,” *Optics Letters* **24**, 711-713 (1999).